C4R

Capacity for Rail

Towards an affordable, resilient, innovative and high-capacity European Railway System for 2030/2050

Innovative concepts and designs for resilient S&Cs (intermediate)

Submission date: 22/06/2016

Deliverable 13.2

This project has received funding from the European Union's Seventh Framework Programme for research, technological development and demonstration under grant agreement n° 605650








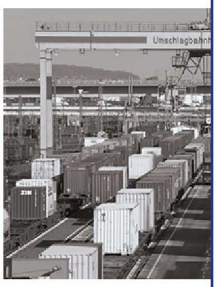

Collaborative project SCP3-GA-2013-60560
Increased Capacity 4 Rail networks through enhanced infrastructure and optimised operations
FP7-SST-2013-RTD-1

Lead contractor for this deliverable:

- CHALMERS

Contributors:

- University of Huddersfield
- VAE
- VCSA
- INECO
- TCDD
- Trafikverket

Project coordinator

- International Union of Railways, UIC

Executive Summary

The turnout (Switch & Crossing, S&C) is a vital component in railway networks as it provides flexibility to traffic operation by allowing trains to switch between tracks. However, the flexibility comes at a cost as the variation and discontinuities in rail profiles in the switch and crossing panels result in increased dynamic loading during wheel passage and thus increased degradation of track (and vehicle) components compared to plain line track. Common damage mechanisms on rails are wear, plastic deformation and rolling contact fatigue (RCF), while components suffer from fatigue (cracked casting) and support degrades (uneven ballast settlement and voids). The present deliverable is an intermediate report describing the work carried out in Capacity4Rail WP1.3, tasks 2, 3 and 4.

The main focus of the report is to investigate and propose innovative designs aiming towards improved S&Cs that reduces material deterioration and failures (task 1.3.2). Based on numerical simulations with validated models and software, the approach is focused on improved understanding of dynamic wheel-rail interaction in S&C and on how the rail degradation can be reduced by optimisation of geometrical and stiffness properties of the turnout. Examples of design variables are rail profiles and the selection of dynamic stiffness for the resilient elements, such as rail pads, base plate pads and under sleeper pads. The influence of rail grade selection and the introduction of friction management in the wheel-rail interface is also covered. The objective is to reduce rail degradation by improved wheel-rail contact conditions leading to a reduction of wheel-rail contact forces (stresses) and creepages. Reduced rail degradation rates will reduce the Life Cycle Cost (LCC) for turnouts. One particular challenge in the optimisation of S&C is to reach a design that is robust in terms of allowing for large variations in traffic conditions due to different vehicle types and worn wheel profiles.

The adopted approach incorporates studies of *short-term design measures* for improving current S&Cs, a *medium-term strategy* where improved solutions are incorporated in an existing railway system and a *long-term vision* where radically new solutions can be introduced without a need for compromising with existing structures. The WP focuses on medium/long distance mixed traffic. However, the design framework developed in the task can be applied to other operational scenarios, e.g. very high speed.

The investigated *short-term solutions* for minimising loads and rail profile degradation in the switch panel include selection of (1) rail profile and rail inclination, (2) rail grade, and (3) friction management. The calculations show that a design with inclined rails (1:30) is superior to the case with vertical rails. The selection of rail grade R350HT instead of R260 leads to a confirmed large reduction in wear. However, the predicted influences of rail grade and friction management on RCF are uncertain due to the wide range of factors influencing RCF initiation, such as the important interaction between crack growth and wear. Thus, the applied RCF damage model needs to be validated by future field observations and measurements. It is shown that both wear and RCF are reduced significantly by maintaining a low friction coefficient in the wheel-rail contact. In particular,

situations with dry wheel-rail contact (high friction) should be avoided as these lead to very high RCF damage impact.

The investigated *medium-term solutions* focus on improving the performance of the crossing panel. These solutions include (1) geometry optimisation of the crossing to minimise impact loads and reduce the steering force damage in the contact areas, (2) dynamic load mitigation (ballast protection) through rail pad stiffness optimisation and the use of under sleeper pads (USP) or connecting elements between sleepers, and (3) novel materials in crossing nose and wing rails to resist fatigue, wear and plastic deformation. The investigation in crossing geometry has highlighted key differences in current design practice and machining tools used for half and full cant (UK terminology, where half cant produces a canted wing rail over half its width, while full cant produces a canted wing over its entire width, see Section 3.2.4.2 for more details) geometries, leading to quantifiably different damage behaviour. Damage has also been predicted on the opposite rail due to imposed creep steering forces in the crossing panel. On that basis, a methodology has been proposed to enable fast and effective optimisation of the crossing wing rail geometry to minimise vertical impact loads, wear and RCF on wing rail and crossing vee. Here also the requirement for additional material behaviour observations (field measurements and lab tests) are highlighted, especially the need to address the specific case of cast manganese steels with different hardening laws and processes than rails in plain line track. A methodology has also been proposed for the optimisation of rail pad stiffness in crossing panel, showing that low stiffness rail pads (ca 80 kN/mm) provide a suitable mitigation for ballast pressure, sleeper acceleration and minimising contact forces, while maintaining acceptable bending stresses of rail components.

The overall design of the S&C has been fundamentally unchanged over at least the last 30 years. To tackle the significant increases in line speed, axle load and volume of traffic the S&C system has been incrementally developed, but from a sub-system or component level. The ambition of the S&C next generation (*long-term solution*) is to consider a whole-system approach by enhanced design, materials and components and to incorporate modern mechatronics for improved system kinematics and control. One example of a long-term solution that is discussed in the report is the Modular Continuous Support (MCS) track, which is a ballast-less track design offering an efficient lower cost rail technology based on pre-fabricated modules and continuously supported rails.

Operation of S&Cs in extreme weather conditions is a challenge to railway administrations (task 1.3.3). Examples of common problems are the difficulty to move the switch rails in situations with a combination of strong winds and heavy snow fall, track instability due to buckling at high temperatures, and deterioration of track support conditions due to heavy rain fall and flooding. These issues are discussed in the report, and innovative designs and operational practices to ensure resilience to extreme weather conditions are suggested.

The last section of the report includes a brief survey of optimised maintenance and sensor strategies (task 1.3.4).

The present work and the writing of this deliverable were performed by Chalmers (lead contractor), University of Huddersfield, VAE, VCSA, INECO, TCDD and Trafikverket.

Table of contents

Abbreviations and acronyms

Abbreviation / Acronym	Description
RCF	Rolling contact fatigue
S&C	Switch and crossing

1. Background

The turnout (Switch & Crossing, S&C) is a vital component in railway networks as it provides flexibility to traffic operation by allowing trains to switch between tracks. However, the flexibility comes at a cost as the variation and discontinuities in rail profiles in the switch and crossing panels result in higher rail (and wheel) degradation rates than in plain line track. Turnouts are often built without transition curves, causing high vehicle jerk (time derivative of lateral vehicle acceleration) at entry and exit of the diverging route. Further, space constraints often prevent the provision of adequate length of support transitions on either side of the S&C unit. Due to the planar nature of a turnout, track inclination (cant) to compensate for the lateral acceleration is not possible.

There are many different railway turnout configurations to fulfil the needs of varying traffic demands. Figure 1.1 illustrates a common layout featuring a straight section called the through route and a curved deviating part called the diverging route. The 'front of the turnout' is defined as the start of the deviating curve in the switch panel. The switching function is realised by switching machines or actuators that position the switch rails according to the desired traffic route. The closure panel connects the switch and crossing panels, whereas the crossing panel allows for wheels to travel along both intersecting paths. Opposite to the crossing, and next to the adjacent through (stock) rails, are the check rails that enforce a constraint on the lateral position of passing wheelsets. This is to avoid interference contact between wheel and crossing nose.

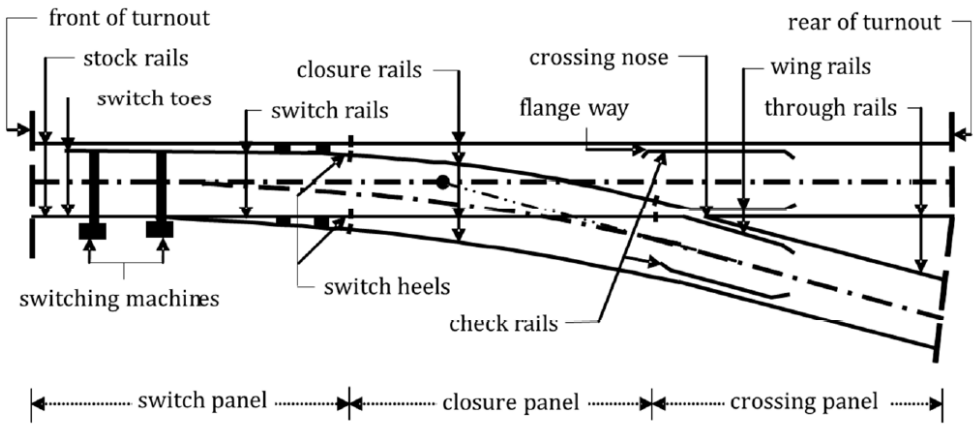

Figure 1.1. Schematic illustration of a turnout (S&C) and its components

The costs for S&C are high as they constitute a key component in railway systems all over the world and consume large capital resources for their construction and maintenance. Turnouts stand for a considerable contribution to reported track faults. In Sweden there are over 12 000 turnouts in some 17 000 km of track [1.1], and the cost for turnout operation and maintenance was 250 – 300 MSEK per year in 2001 to 2004 [1.2]. In the EC FP6 sponsored European project INNOTRACK [1.3], LCC models were used to find cost drivers for S&C and to study the cost benefits of innovative solutions. Within INNOTRACK, Deutsche Bahn (DB) analysed a set of 458 turnouts on a high-speed line with a mixed traffic volume of about 17.5 mega gross tonnes (MGT) per year [1.4]. It was concluded that 50% of the overall costs were for inspection, service and test measures. Out of the remaining costs it was found that renewal of switch rails, crossings and large elements such as check rails stood for 65% of the costs while other maintenance activities such as welding and tamping constituted the remainder of the costs. With such a large contribution to the overall costs, it was quite naturally found that optimized components such as switch rails and crossings with a longer service life can help to reduce the life cycle costs for turnouts [1.3].

1.1 REFERENCES

[1.1] A. Nissen, *Development of life cycle cost model and analyses for railway switches and crossings*, PhD Thesis, Division of Operation and Maintenance Engineering, Luleå University of Technology, Luleå, 2009

[1.2] A. Nissen, *Analys av statistik om spårväxlars underhållsbehov (analysis of statistics of maintenance requirements for railway turnouts, in Swedish)*, Licentiate Thesis, Division of Operation and Maintenance Engineering, Luleå University of Technology Luleå, 2005

[1.3] A. Ekberg, and B. Paulsson (eds.), *INNOTRACK: Concluding technical report*, International Union of Railways (UIC), Paris, 2010, 288 pp

[1.4] W. Grönlund, and G. Baumann (eds.), *INNOTRACK: D3.1.1/D3.1.2 Definition of key parameters and Report on cost-drivers for goal-directed innovation*, www.innotrack.net, 2008, 37 pp

2. Objectives

The objectives of WP1.3 in Capacity4Rail are to:

- Identify current and future operational failure modes of S&Cs and related root causes (task 1.3.1). This was reported in deliverable D1.3.1.
- Propose innovative designs to minimize material deterioration and failures (task 1.3.2)
- Suggest innovative designs and operational practices to ensure resilience to extreme weather conditions and improved maintainability (task 1.3.3)
- Survey optimized maintenance and sensor strategies (task 1.3.4)
- Perform in-field demonstration of key concepts (task 1.3.5). This work is not covered in the present report.

Part of this intermediate report (deliverable D13.2) is presenting the work performed in task 1.3.2 aiming towards an optimisation of the design of S&C. It is focused on the understanding of dynamic wheel-rail interaction in S&C and on how the rail degradation can be reduced by optimisation of geometrical and stiffness properties of the track superstructure, such as the design of rail profiles and the selection of stiffness of resilient elements (rail pads, base plate pads, under sleeper pads). The influence of rail grade selection and the introduction of friction management in the wheel-rail interface is also covered. The objective is to reduce rail degradation by improved wheel-rail contact conditions leading to a reduction of wheel-rail contact forces (stresses) and creepages. Reduced rail degradation rates will reduce the Life Cycle Cost (LCC) for turnouts.

Further, this report surveys problems occurring with S&C in extreme weather conditions (warm and cold climate, flooding) and suggests remedial actions.

3. Innovative designs minimizing S&C loads and material deterioration (C4R task 1.3.2)

Capacity4Rail WP1.3 aims to provide for a drastic improvement in S&C design and operations. To a successful end, the strategy outlined incorporates short-term objectives in improving current S&Cs, a medium term strategy where improved solutions are incorporated in an existing railway system and a long-term vision where radically new solutions can be introduced without a need for compromising with existing structures. The WP focuses on medium/long distance mixed traffic. However, the design framework developed in the task can be applied to other operational scenarios, e.g. very high speed and in spin-off projects.

This chapter covers work performed in Capacity4Rail task 1.3.2. Short-term design solutions, with particular focus on the switch panel, have been studied by Chalmers and are presented in Section 3.1. Medium-term design solutions, with focus on the crossing panel, have been the focus of the work by University of Huddersfield, see Section 3.2. Long-term design solutions are briefly described by VAE and VCSA, see Section 3.3.

References to Section 3.1 are listed in Section 3.1.8, while references to Section 3.2 are listed in Section 3.2.8.

3.1 SHORT-TERM DESIGN SOLUTIONS

In this section, focus is on short-term design solutions for mitigation of accumulated damage in the switch panel. In this part of the turnout, the combined profile of the stock and switch rail assembly results in non-smooth rolling radius difference characteristics due to contact between wheel flange and switch rail. As the rolling radius difference that can be generated is reduced (compared to for a standard rail profile), this contact condition reduces the steering capability of the wheelset leading to a magnification of the lateral wheel–rail contact force [3.1.1]. Further, the two-point contact situation with one contact point on the switch rail and one on the stock rail induces relative motion and slip between wheel and rail leading to high energy dissipation, in this section referred to as $T\gamma$ (creep force multiplied with creepage).

Examples of wear and RCF damage in the switch panel are shown in Figure 3.1.1, where severe wear is observed on the switch rail, while RCF has been generated on the crown of the stock rail. This particular RCF defect mainly occurs in the wheel transfer area from stock rail to switch rail, caused by high tangential contact stresses leading to near surface crack initiation. However, RCF damage does also occur on the switch rail. Subsequent merger of cracks leads to detachment of material (spalling). Corrective measures include grinding or replacement of the switch and stock rail assembly.

Means to mitigate the insufficient rolling radius difference and improve the contact conditions include prescribed track gauge widening and optimisation of switch rail profiles [3.1.3, 3.1.4]. For example, it has been shown that a variation of prescribed track gauge widening along the switch panel is efficient in the through route and improves the situation in the diverging route. Optimisation of switch rail profile to allow for an earlier full transition from stock rail to switch rail (facing move) is particularly efficient in the diverging route. However, limits on switch rail loading need to be established to determine the feasible design space. Combining the two measures can be an effective solution for reduced damage because the track gauge widening makes it possible to increase the thickness and strength of the front section of the switch rail.

Thus, short-term design solutions for minimising loads and rail profile degradation in the switch panel include (1) prescribed track gauge widening and (2) rail profile optimisation (also considering rail inclination). Other short-term solutions include (3) different rail grades and (4) friction management. Based on numerical simulations, solutions (2), (3) and (4) will be studied in this section.

Section 3.1 has been written by Chalmers, except Section 3.1.1 which has been written by INECO.

Figure 3.1.1. Wear on the switch rail and RCF on the stock rail caused by high tangential contact stresses. From [3.1.2]

3.1.1 IN SITU MEASUREMENT OF PROFILE DAMAGE OF THE SWITCH RAILS

3.1.1.1 Background

The acquisition of real data from railway lines in service is a valuable work that helps to understand the wearing processes of the components in a turnout. The periodical inspections of the track superstructure, i.e. rail condition, track geometry, S&C performance, etc. are complemented with rolling stock inspections and the conditions of traffic operation. Correct management of all this information leads to a better understanding of the ageing and degradation processes of turnout components.

In some situations, it may be very interesting to select an S&C in the network where particular defects are recurrent or are showing at an early stage. More intense inspections can be done to monitor the evolution of these defects, and the data can be combined with the information from the rolling stock side (wheel profile condition, number of MGT, intensity of traffic, etc.). The implementation of all sources of information gives clues of the causes of a particular defect, e.g. the excessive damage of a stock rail after a relatively short time in track.

However, taking this information to the research projects related with the study of damage in particular parts of S&Cs is also very important. It definitely helps to fit the results of the laboratory models to the real conditions of a turnout in operation. Reciprocally, railway maintenance staff can be advised on the future condition of track elements and plan actions to prevent some defects reaching a critical level.

3.1.1.2 Procedure for measurements in an S&C

In order to apply the methodology explained in the background, an S&C has been selected out of all turnouts of a particular metropolitan network. Measuring on this type of railway systems has some advantages:

- Traffic parameters are known and constant (mass, frequency, axles, …)
- Rolling stock is almost mono-type
- Wheel profiles are homogeneous and easy to measure
- Turnouts are operated in the same position and direction at most of cases (except in manoeuvring, redirecting to depots, etc.)
- Maintenance protocols and actions are mostly periodical and well reported

A full inspection of the turnout components has been performed, which includes the following aspects:

- Geometry (track gauge, inclination, alignment, safety parameters, …)
- Coupling of the switch rail
- Sitting of the switch rail on the slide baseplates
- Curving of the switch rail in the diverging route
- Proper work of the locking system
- Condition of the crossing
- Presence of damage (wear or any other rail defect)
- Measurement of the rail profile at several locations

Figure 3.1.2 shows a general view of the selected S&C. The turnout characteristics are diverging curvature 154 metres and tangent 1:8.5. Manufactured in rail 54E1 with an inclination 1:20 on straight route and vertical on the switch part.

Figure 3.1.2. Photo of selected S&C

3.1.1.3 Study of defects

In this study, the aim is to detect the causes for excessive damage on the left-side switch rail and stock rail when both rails are coupled in diverging track, see Figure 3.1.3. Besides, on the right-side stock rail there is a noticeable vertical wear, see Figure 3.1.4. On this stock rail, there is also a plastic deformation on the gauge corner at the field side, see Figure 3.1.5. This premature damage has been noticed in several S&C that are installed in the same line, so it is important to detect the causes and set actions to prevent the defect to damage a large number of turnouts. There is an irregular running surface along the switch rails and a notable wearing from the corner gauge to the top of the coupled stock rail. Thus, the profile of both rails has been carefully measured during the inspection. Further photos from the selected S&C are shown in Figures 3.1.3-3.1.5.

Figure 3.1.3. View of coupled switch rail and stock rail (allowing for diverging track)

Figure 3.1.4. Stock rail on the right side. When uncoupled, it allows for traffic to diverging track

Figure 3.1.5. Stock rail on the right side. View of the field side seen from the switch toe

3.1.1.4 Rail profile measurement

The transverse profiles of the switch rail and stock rails have been measured by using the Miniprof tool. Specific measurements have been performed on each set of switch rail and stock rail at 200 mm and at 1000 mm from the toe of the swith rail. The results are reported in the following template, see Figure 3.1.6.

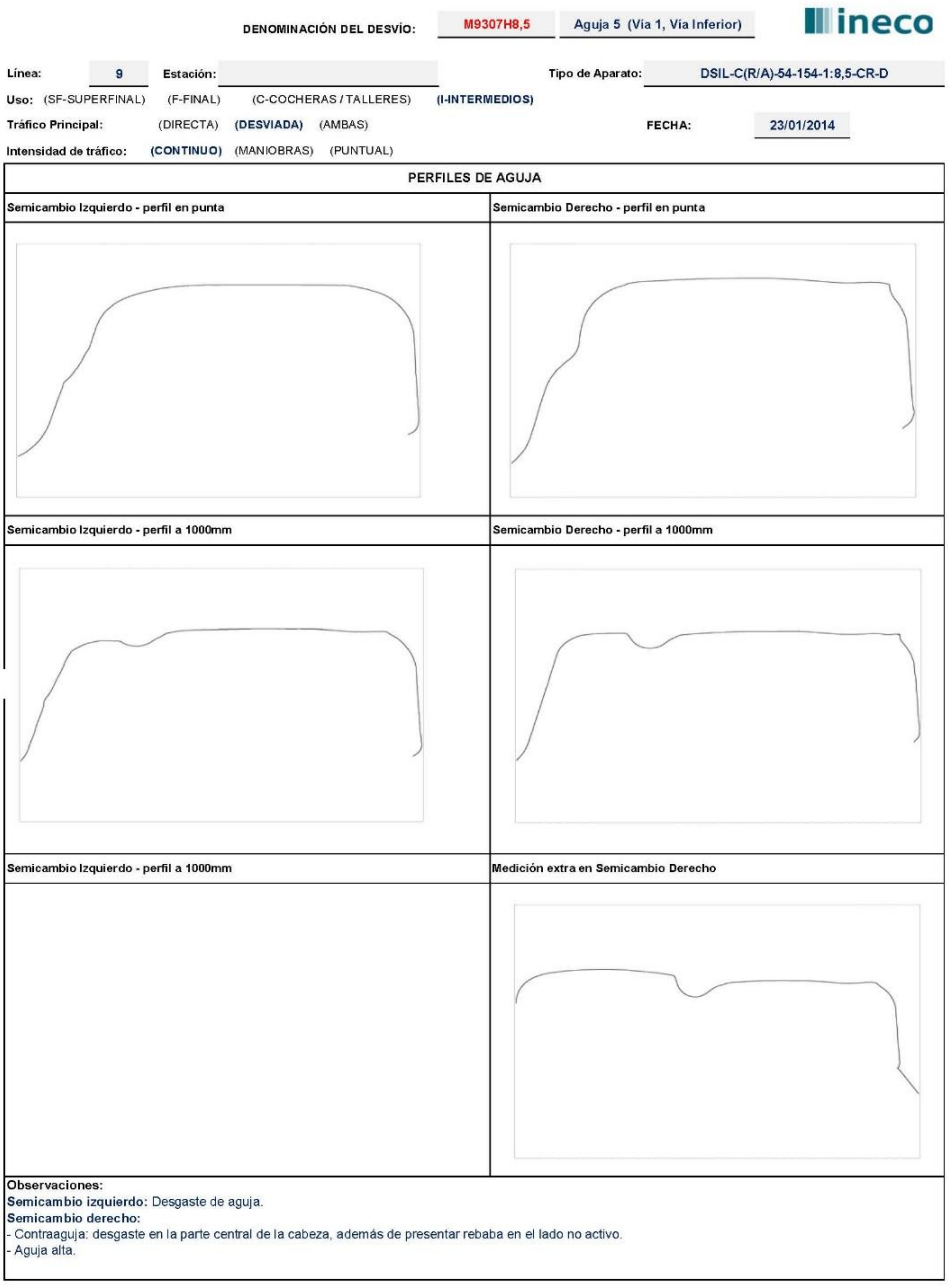
DENOMINACIÓN DEL DESVÍO: M9307H8,5 Aguja 5 (Vía 1, Vía Inferior)

Línea: 9 Estación: Tipo de Aparato: DSIL-C(R/A)-54-154-1:8,5-CR-D

Uso: (SF-SUPERFINAL) (F-FINAL) (C-COCHERAS / TALLERES) (I-INTERMEDIOS)

Tráfico Principal: (DIRECTA) (DESVIADA) (AMBAS) FECHA: 23/01/2014

Intensidad de tráfico: (CONTINUO) (MANIOBRAS) (PUNTUAL)

PERFILES DE AGUJA

Semicambio Izquierdo - perfil en punta | Semicambio Derecho - perfil en punta

Semicambio Izquierdo - perfil a 1000mm | Semicambio Derecho - perfil a 1000mm

Semicambio Izquierdo - perfil a 1000mm | Medición extra en Semicambio Derecho

Observaciones:
Semicambio izquierdo: Desgaste de aguja.
Semicambio derecho:
- Contraaguja: desgaste en la parte central de la cabeza, además de presentar rebaba en el lado no activo.
- Aguja alta.

Figure 3.1.6. Graphic reporting. Left column shows profiles of the left hand side rails at (from top down) 200 mm and 1000 mm. Right column shows profiles of the right hand side rails at (from top down) 200 mm, 1000 mm and 1600 mm

3.1.1.5 Wheel profile measurement

In order to have good information about the interaction between the switch rails and the wheels of the rolling stock, several measurements of wheel profile for the trainsets in operation have been performed, see Figure 3.1.7. As the types of trains are similar and all of them work in the same conditions, this information helps greatly in the understanding of the damages observed.

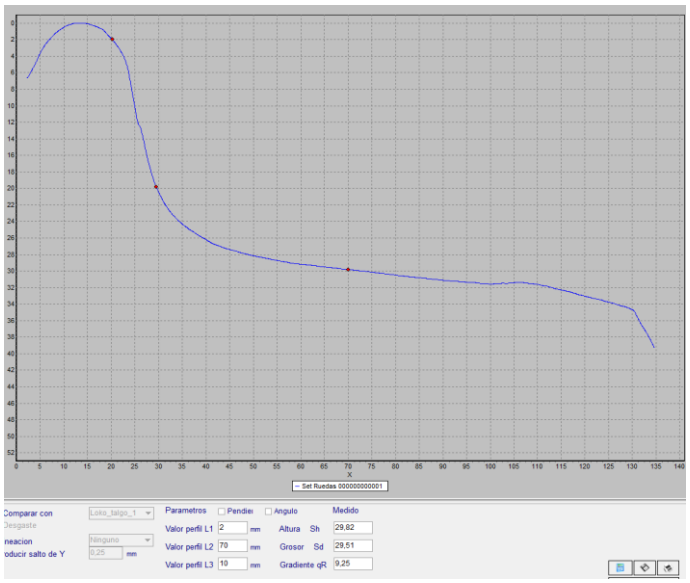

Figure 3.1.7. Measurement of wheel profile

3.1.1.6 Traffic conditions

- Type of traffic: there is an intense traffic, one trainset every 4 min. Most trains run in the diverging route.
- Type of trains: Trainset series 9000, 5 coaches, 20 axles, axle payload: 10 t.
- Annual tonnage (estimated) = 12.4 MGT per year.

3.1.1.7 Postprocessing of the profile measurements

The combination of the real profile and the original one (as designed) is done in order to detect any distortion of shape, excessive wearing, etc. In this case, the damage observed is caused by an irregular wheel/rail interaction, which causes diverse defects.

The thickness of material removed from the running surface of the switch rails is calculated from the graphic results, see examples in Figures 3.1.8 – 3.1.10.

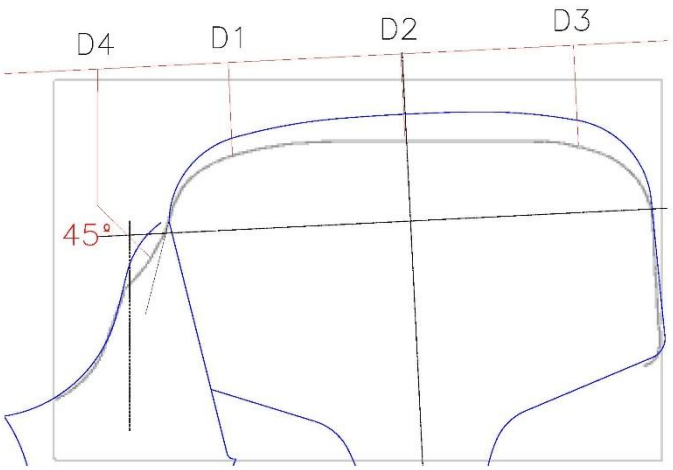

Switch rail	Stock rail		
D4 [mm]	D1 [mm]	D2 [mm]	D3 [mm]
3.265	3.13	4.7	4.53

Figure 3.1.8. Combination of profiles at 200 mm from the beginning of the switch rail (switch rail and stock rail coupled). Blue is new rail and grey is measured rail. ***The matching point is the down gauge corner of the field side, then the worn profile is adapted to the nominal inclination.*** *Results of thickness of material removed*

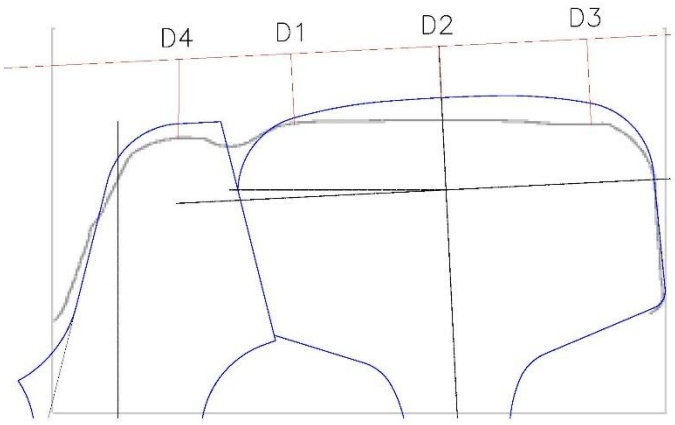

Switch rail	Stock rail		
D4 [mm]	D1 [mm]	D2 [mm]	D3 [mm]
3.33	1.575	4.795	4.585

Figure 3.1.9. Combination of profiles at the 1000 mm from the beginning of the switch rail (switch rail and stock rail coupled). Results of thickness of material removed. See also caption to Figure 3.1.8

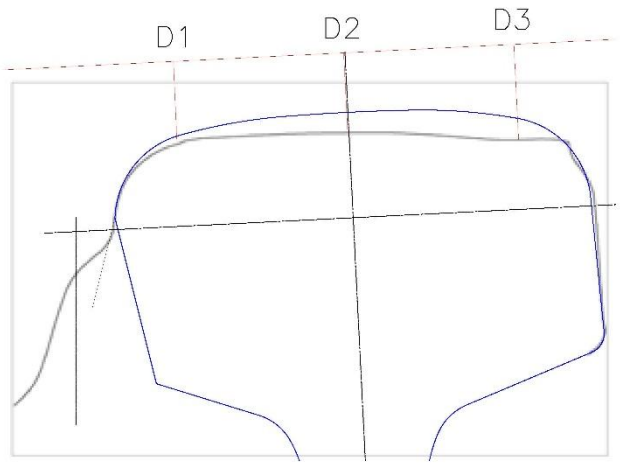

Switch rail	Stock rail		
D4 [mm]	D1 [mm]	D2 [mm]	D3 [mm]
-	1.095	3.48	3.875

Figure 3.1.10. Combination of profiles at the beginning of the right stock rail 200 mm from the switch rail toe (as reference). Results of thickness of material removed. See also caption to Figure 3.1.8

3.1.1.8 Comments to the measurement procedure

The methodology for the acquisition of data from S&C in operation and the processing of this information to analyse the damage due to wheel/rail interaction is useful from the point of view of the treatment of particular defects on the rails in an S&C. In a further study, it may be useful to study the influence of tonnage and type of traffic on accumulated wear. Eventually the results can be applied to validate the developed models to simulate damage and improve designs.

It is observed that the combination of the theoretical switch profile and the measured profile is sometimes difficult due to shape of the running surface after some time in operation. There are some defects, i.e. plastic deformations or abnormal wear, which makes an accurate matching difficult. Therefore, an accurate procedure for matching both images is necessary and even more so when there is a need to measure thin layers of removed material.

It is also observed that a poor condition of the wheel profile – on an average basis – is detrimental as it creates damage in areas where the wheel/rail contact is not expected. Nonetheless, the geometry of the S&C and the proper coupling of the switch rail and sitting to the slide base plates is determinant for the occurrence of premature damages.

3.1.2 METHODOLOGY FOR NUMERICAL PREDICTION OF ACCUMULATED RAIL DAMAGE

A brief overview and description of the methodology applied by Chalmers in numerical prediction of accumulated rail damage (wear and RCF) is given below. Further details can be found in [3.1.5].

Two different wear regimes, mild and severe wear, in terms of wear rate and characteristics of wear debris were identified in [3.1.6]. Different parts of the rail profile may be subjected to different wear regimes, the wear rate at the gauge corner being up to ten times higher than on the rail crown [3.1.7]. This can be accounted for in a prediction model by implementing a wear map where the wear coefficient in the wear model is dependent on normal contact pressure p_z and sliding velocity **s** [3.1.8], see also Section 3.1.4.

Two models for evaluation of rail wear have been applied in this study. Model A (often referred to as the *Tγ* method) is based on the calculated energy dissipation given by the summed products of force and corresponding creepage in each wheel–rail contact. For each wheel *i* passing through the switch panel on the side where the wheel transfers from stock rail to switch rail (the damage on the opposite rail is not considered here as it is significantly lower) and each evaluated instant in time, the energy dissipation W_i is calculated by summing the work in up to two considered contact points/patches (j=1, 2) as

$$W_i = \sum_{j=1}^{2} T_{x,j}\gamma_{x,j} + T_{y,j}\gamma_{y,j} \tag{1}$$

where T_x and T_y are the tangential contact forces in the contact plane, and γ_x and γ_y are the associated creepages (note that the contribution due to spin has been dropped here). From the output of each simulation of dynamic vehicle-track interaction, the energy dissipation at N_i discrete time steps is assembled in the vector $\mathbf{W}_i$ ($N_i \times 1$), collecting data for the most loaded front section of the switch and stock rail assembly, see [3.1.3]. For each wheel passage, a scalar damage value D_i^{w} ('w' for wear) is then evaluated as

$$D_i^{\mathrm{w}} = \frac{\sqrt{\mathbf{W}_i^{\mathrm{T}}\mathbf{W}_i}}{N_i} \tag{2}$$

The vector norm of the damage value is used to obtain a weighted average of the total friction work, thus indicating the total material removal, while providing a penalty to high local values. Model A allows for a fast assessment of the influence of switch panel geometry on damage over the switch panel as it requires no further post-processing of the output from GENSYS.

Model B applies the Archard model of sliding wear. The distributions of contact stress and sliding distance are determined from a FASTSIM discretisation of the contact area. According to the Archard wear model, the volume V_{wear} of worn material is calculated as

$$V_{\text{wear}} = k_{\text{w}}(p_z, s) \cdot \frac{Nd}{H} \tag{3}$$

where k_{w} is the non-dimensional wear coefficient given by a wear map, N is the normal contact force, d is the sliding distance and H is the hardness of the softer material. For further details about wear model B, see [3.1.5].

The development of surface initiated RCF cracks is due to accumulated plastic deformation (ratchetting) of the surface material caused by cyclic loading leading to compressive and shear stresses acting at the wheel-rail contact surface [3.1.9, 3.1.10]. Cracks are formed if the plastic deformation exceeds the fracture strain of the material. Crack growth is promoted not only due to subsequent rolling contact loading, but also due to hydro-pressurisation caused by fluid trapped in the crack.

Based on shakedown theory (assuming full slip and Hertzian wheel–rail contact conditions), an index for time-efficient prediction of rolling contact load levels resulting in ratchetting was introduced in [3.1.9] as

$$FI_{\text{surf}} = f - \frac{2\pi abk}{3N} \tag{4}$$

where f is the traction coefficient given by the ratio of resultant tangential contact force and normal contact force, while a and b are the semi-axes of the Hertzian contact patch. For rail grade R260, the yield stress in shear for the work-hardened material is taken as k = 300 MPa. Surface initiated RCF is predicted to occur if

$$FI_{\text{surf}} > 0 \tag{5}$$

Using this model, the risk for surface initiated RCF can be predicted by straight-forward assessment of output from a simulation of vehicle-track interaction. However, in an assessment of different RCF prediction models [3.1.11], it was pointed out that disadvantages of the FI_{surf} model are the assumption of full slip and that it does not consider that wear is generally the dominating type of damage at high levels of slip. High levels of wear will wear away cracks and lead to an increase of fatigue life. Wear (and plastic deformation) will also alter the contact geometry that may lead to an increase or decrease in contact stresses. More general slip conditions (partial slip) will be accounted for in this study by relating the RCF damage to the local shear stress [3.1.12].

An alternative approach to predict RCF on rails is to relate a fatigue damage index to the energy dissipation $T\gamma$ in the wheel–rail contact [3.1.13, 3.1.14]. At high levels of energy dissipation, the wear rate is higher than the crack growth resulting in no RCF damage. This is reflected in the model by a

multi-linear relationship between damage index and $T\gamma$. A disadvantage of this model is that it is empirical and needs to be calibrated for different applications of rail grades and traffic conditions. Based on validation of the model versus field observations of surface initiated RCF on various curves with rail grade R260 or R350HT, it was concluded that no RCF damage occurs for $T\gamma > 175$ J/m and $T\gamma > 400$ J/m, respectively, see [3.1.14]. For wheel–rail contact occurring between wheel flange and gauge side of the switch rail, it can be concluded that evaluated $T\gamma$-values generally exceed the limit values indicating that wear is the dominating damage mechanism. As this is in agreement with field observations, it is proposed here to apply the model based on shakedown theory (see Equation (4)) but to multiply the predicted damage with a penalty function $f_p(T\gamma)$ that is reflecting the damage index in [3.1.13, 3.1.14]. Thus, for all grid elements of a given contact patch, this means that there is no RCF damage if $T\gamma$ evaluated for the complete contact patch exceeds the threshold value (175 J/m for R260 and 400 J/m for R350HT). If $T\gamma$ evaluated for the complete contact patch is in the range between the maximum in the damage index function and the threshold value, the RCF damage will be scaled down by the suggested penalty function.

The model used here for prediction of accumulated damage (wear and RCF) in the switch panel is described in further detail in [3.1.5]. The model is inspired by the approach presented by Dirks et al [3.1.11, 3.1.15], where Archard's model is applied for the calculation of wear, while the shakedown approach and the empirical damage index model are compared for the calculation of RCF. It was shown that fatigue life prediction based on the two RCF models can differ, in particular in situations with severe wear such as in small radius curves. However, if wear is considered in the shakedown approach model (as is already the case in the damage index model), it was shown that the two models give comparable results. It was also concluded that the two RCF models lead to different results in cases with poor adhesion conditions (high slip) since the influence of creepage is only explicitly implemented in the damage index model. In [3.1.15], the two RCF models were extended with a computationally efficient model for propagation of short cracks. The extension leads to that two material parameters need to be determined by calibration with field measurements.

3.1.3 INFLUENCE OF RAIL GRADE ON WEAR AND HEAD CHECK GROWTH – REVIEW OF LABORATORY TESTS AND FIELD OBSERVATIONS

The measured influence of rail grade on wear rate and head check initiation and growth on standard (curved) track has been investigated in several references. In this section, a summary of important results and conclusions from laboratory tests (twin disk tests and wheel/rail roller rig tests) and field observations is given with particular focus on the compared performance of R260 and R350HT. The section ends with a recommendation on rail grade selection from the INNOTRACK project [3.1.16], see also [3.1.17].

Results from twin disk tests (performed by Corus) with various pearlitic rail steels are reported in [3.1.16] and are copied in Figures 3.1.11 and 3.1.12. The tests show an increasing resistance to wear and RCF initiation with increasing hardness of the rail.

Twin disk tests performed at DB with different combinations of wheel and rail materials are reported in [3.1.18]. The prescribed normal contact pressure in the tests was 1250 MPa and the slip was 3%. A drop of water was applied to the contact at 20 s intervals (wet conditions). The results are shown in Figure 3.1.13. For pairing with wheel material R7, it is observed that rail wear was increased by a factor of about 1.2 if R260 was used for the rail instead of R350HT.

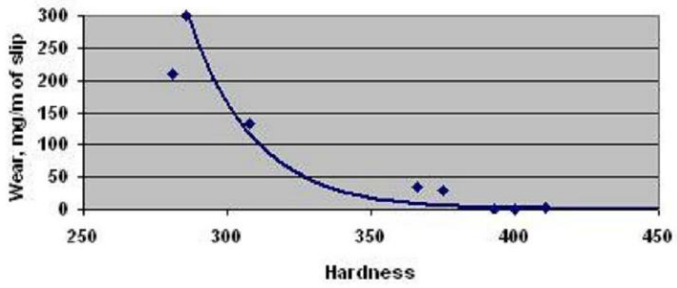

Figure 3.1.11. Influence of hardness on wear rate. Twin disk test. From [3.1.16]

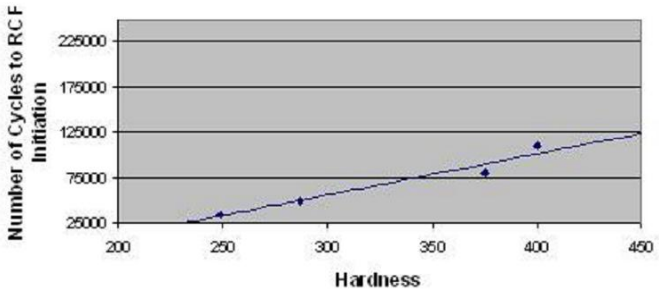

Figure 3.1.12. Influence of hardness on number of cycles to RCF initiation. Twin disk test. From [3.1.16]

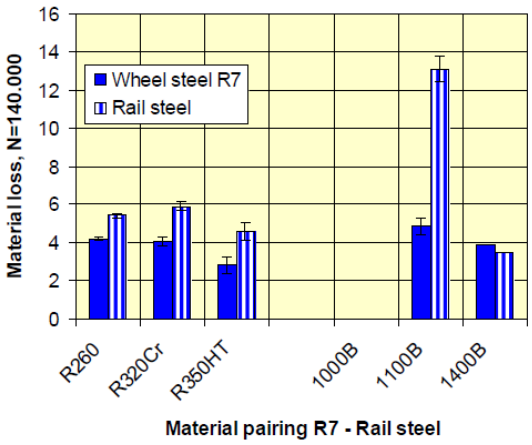

Figure 3.1.13. Influence of wheel and rail material on wear. Twin disk test (wet conditions). From [3.1.18]

Extensive laboratory tests have been performed in a full-scale wheel/rail test rig at DB Kirchmöser [3.1.19]. In this case, the applied contact forces are similar to the contact forces in a real application in the field and realistic vehicle speeds can be simulated. This means there is no need to use a scaling of contact forces and slip, which may lead to uncertain results in a twin disk test. However, note that the laboratory tests are conducted with the same wheel profile whereas the rail in track sees a wide variety of wheel profiles and vehicles. Although the laboratory tests were successful in initiating RCF, the nature and magnitudes of the crack were different to those seen in samples taken out of track. Corus (Tata) also examined samples from the full-scale rig and the results were reported in INNOTRACK. Different combinations of rail and wheel materials were tested in dry conditions, see Figure 3.1.14. For pairing with wheel steel ER7, it is observed that rail wear was reduced by a factor of about 6 if R350HT was used instead of R260. Further, it was concluded that neither more wear nor more RCF damage was detected on either wheel or rail when using a harder contact partner.

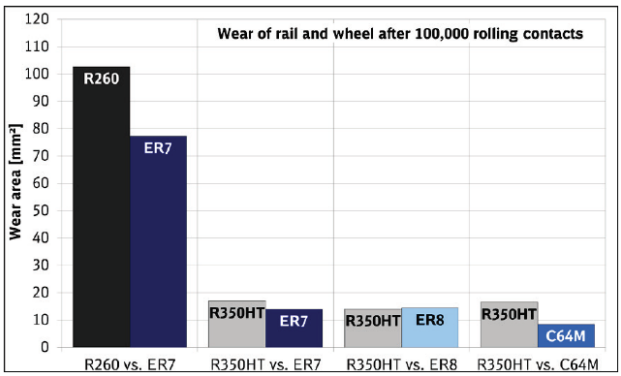

Figure 3.1.14. Wear of wheel and rail for different combinations of material (rail wear in the left columns). Full-scale wheel/rail test rig (dry conditions). From [3.1.19]

A comprehensive database containing field measurements from the years 1998-2012 has been compiled by DB [3.1.20, 3.1.21]. The database has been used to determine rates of head check growth and wear in R260 and R350HT grade rail steels, see Figures 3.1.15 and 3.1.16. For R260, it was concluded that the depth of head check cracks grows at a rate of 0.8-2.8 mm/ 100 MGT, while for R350HT the growth rate is 0.1-1.2 mm/100 MGT. The database indicates no influence of curve radius on head check growth for radii in the interval 300-6000 m and no influence of cant, cant deficiency or permissible speed. Further, it was observed that head checks were avoided by using a bainitic steel. However, it should also be pointed out that three different grades of bainitic steels are available to the railways: a low carbon carbide free bainitic steel from Tata that has shown very high resistance to RCF, a high carbon heat treated bainitic steel from voestalpine whose performance has been found to be not as good as R400HT, and the final bainitic steel with a chemistry developed by DB whose performance is also believed to be good.

In curves with radius greater than 1000 m, wear rates for R260 were between 0.5 and 1.0 mm/100 MGT and between 0.2 and 0.4 mm/100 MGT for R350HT [3.1.20]. In small radius curves, wear rates increase exponentially with decreasing curve radius reaching values of several millimetres per 100 MGT of traffic. For a given curve with two different rail grades, it was found that wear rates for R260 were 1.5 – 3 times greater than for R350HT [3.1.20].

Note that it is important to differentiate between vertical wear and side wear as the mechanisms causing these two types of wear are different. Large radii curves do not suffer from side wear, whereas in tight curve radii the rail is subjected to both vertical and side wear. In tight radii curves, it is largely the magnitude of side wear that determines rail life.

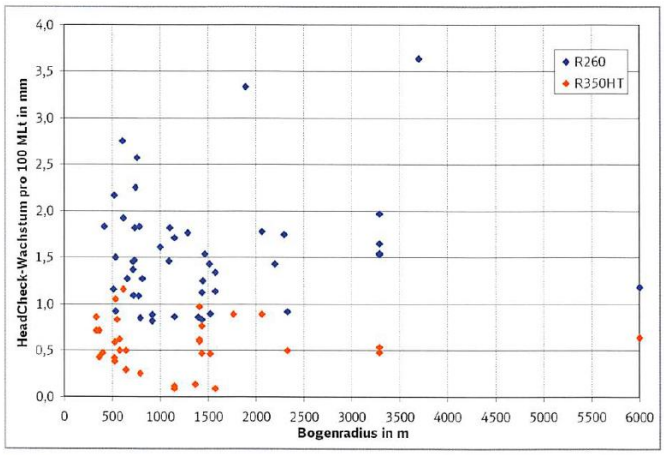

Figure 3.1.15. Influence of curve radius and rail grade on head check growth per 100 MGT. From [3.1.21]

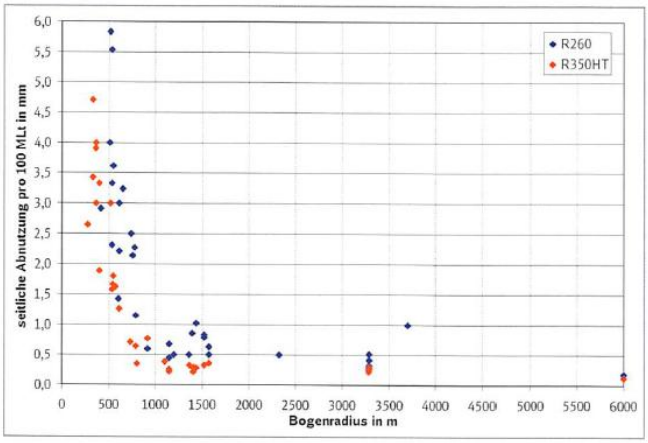

Figure 3.1.16. Influence of curve radius and rail grade on gauge corner rail wear per 100 MGT. From [3.1.21]

The database [3.1.20] also shows that modern traction units with electric power transmission and automatic traction control facilitate the formation of head checks. Homogeneous vehicle fleets tend to produce a narrow band for the wheel-rail contacts. This could be the reason for early onset of RCF observed in suburban rapid transit systems and on homogeneous high-speed lines. The combination of wheel and rail profiles has a major effect on the stresses in the wheel-rail contact patch, and the contact patch becomes smaller the closer the contact point is to the gauge corner and the smaller the gauge corner radius. In Germany since 2010, an anti-head-check (AHC) profile is used on all outer rails in curves with radius up to 3000 m. The AHC profile corresponds to the 60E2 profile with a rail inclination 1:40 and with a radial deviation (material removal) at the gauge corner of at most -0.6 mm. It was also concluded that the stability of the wheel/rail profiles is larger when using higher-strength steels.

In a long-term field test (part of the Optikon project), DB placed eight different steel grades in a 791 m curve near Vilshofen [3.1.22]. The test curve with curve radius 791 m, 60E1 rail profile and mixed traffic conditions (maximum speed 130 km/h) was prepared by welding 15 m sections of different rail grades. Gauge corner wear and RCF were monitored during 10 years corresponding to an accumulated traffic load of 170 MGT, see Figure 3.1.17. It was concluded that the higher strength pearlitic steels resulted in less wear than R260, the factor between R260 and R350HT being about 1.8. The heat-treated pearlitic grades revealed head checks but not as deep as for R260. The three hard pearlitic R320Cr grades showed low levels of wear but head checks were not completely eliminated. The bainitic rail steels showed differences in performance. The high manganese and low carbon (1100Mn) bainitic steel showed no head checks but a high level of wear. Finally it was pointed out that the 1400Cr bainitic grade had low wear and no head checks but requires more demanding welding techniques.

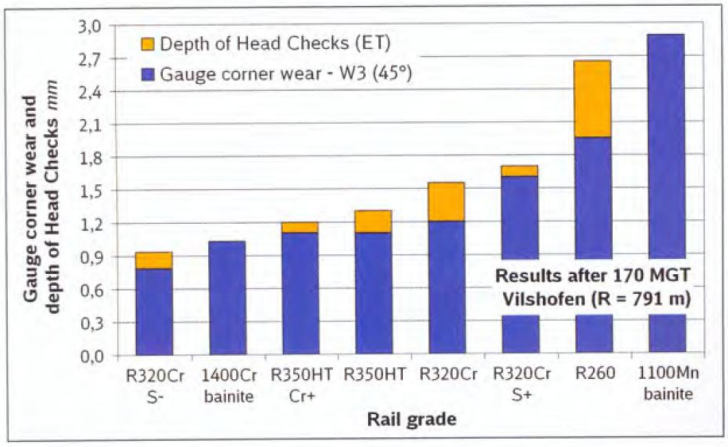

Figure 3.1.17. Influence of rail grade on gauge corner wear and depth of head checks (field conditions). From [3.1.22]

Field tests to compare the performance of R260 and R350HT have also been reported in [3.1.23]. It was concluded that for a medium-speed track with curve radius 3300 m, the wear of the R260 rail was about 1.6 times higher than for R350HT. For a high-speed tangent track and curve with radius 6000 m, the corresponding factors were about 1.6 and 1.4, respectively.

Based on track data collected by Corus and voestalpine in the INNOTRACK project, it was found that gauge corner (45°) wear is significantly dependent on curve radius with higher wear occurring on tighter radius curves [3.1.24]. It was concluded that the influence of rail grade is reduced wear in inverse proportion to the increasing hardness, with a pronounced influence for the smaller radius curves, see Figure 3.1.18. Empirical formulae for mean wear rate for three rail grades are given in Figure 3.1.18. No formula could be determined for R350HT due to a limited number of test sites with this rail grade. It should also be noted that there is a significant scatter in the data and that there are many unknown/uncontrolled variables that could have affected the measured wear rates resulting in the observed scatter of results.

A guideline for selection of rail grade for standard track leading to improved durability and reduced need for maintenance was one of the key results of the INNOTRACK project [3.1.16]. The guideline is based on various laboratory and field (track) tests, many of them being referred to above. For given applications, recommendations of different rail grades are provided, either in terms of curve radius and tonnage or based on accepted track degradation (wear rate and head check crack depth rate). The recommended use of a range of rail steel grades for different applications (curve radius and tonnage) is shown in Figure 3.1.19. In INNOTRACK, it was concluded that the use of heat treated rail grades, such as R350HT, to reduce both wear and RCF is beneficial for curves with radius up to 3000 m.

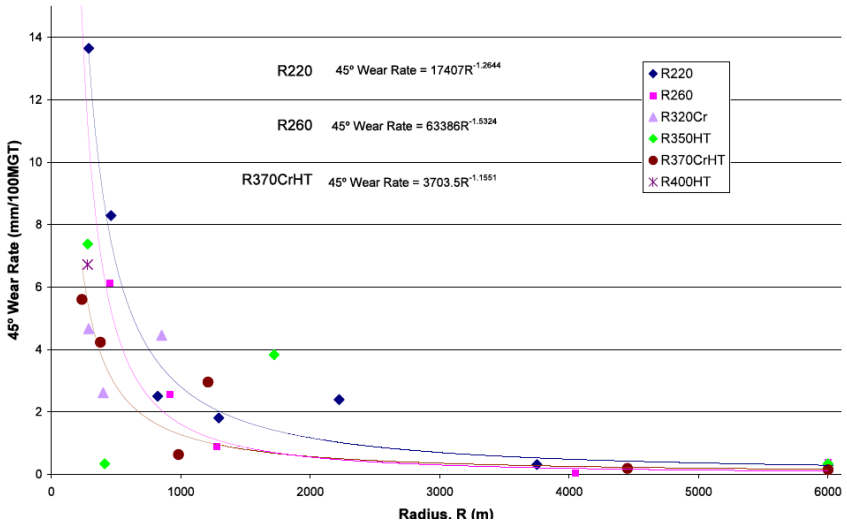

Figure 3.1.18. Influence of curve radius and rail grade on gauge corner (45°) wear rate. From [3.1.16]

According to [3.1.16], wear is dominant in curves with radius less than 1000 m, while RCF occurs for radii in the range 500 to 5000 m. Increasing hardness of pearlitic rail steels leads to higher resistance to both wear and RCF, where the improvement in terms of wear for R350HT relative to R260 is in the order of a factor 3 (and higher for small radius curves), and at least a factor 2 for RCF.

Wear and RCF initiation are influenced by the conditions (contact stresses) in the wheel-rail contacts. The contact stresses are determined by the normal and tangential contact forces, the combination of wheel/rail profiles and the size of the contact patch. This means that conditions in a curve of a standard track and subsequent rail damage cannot be directly translated to the conditions in a switch panel.

Unfortunately, official documents reporting results from field studies of influence of material in a switch panel have not been found. However, for a given S&C geometry and tonnage, the expected improvement in terms of wear has been stated to be in the order of a factor 2 when using switch rails manufactured with rail grade R350HT instead of R260 [3.1.25]. For a switch panel with curve radius smaller than 300 m, the expected improvement is higher than a factor 2. However, it should also be emphasised that the harshness of contact conditions can vary very considerably from one S&C unit to another and hence comparative evaluation of different rail grades becomes more challenging.

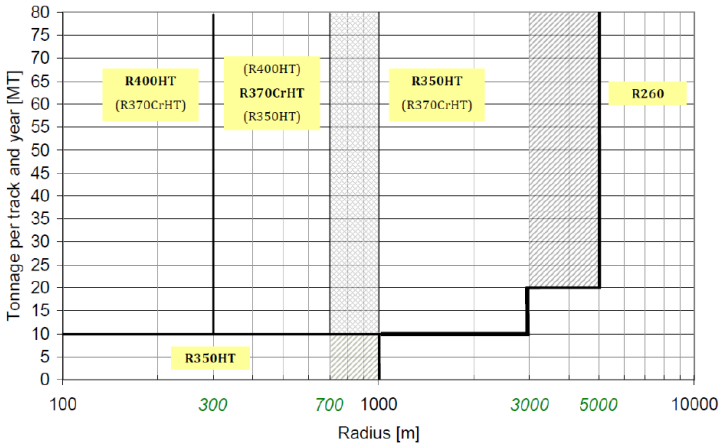

Figure 3.1.19. INNOTRACK recommendation on rail grade selection. From [3.1.16]

3.1.4 INPUT DATA TO DAMAGE MODELS – FOCUS ON R260 AND R350HT

The concept of wear maps was introduced by Lim and Ashby [3.1.26] to classify the influence of different dry wear mechanisms (delamination, mild and severe oxidation, melting, seizure, etc.) on wear data. Based on pin-on-disk and twin disc tests (dry conditions), wear coefficient maps for different wheel/rail material combinations were derived in [3.1.27]. The results showed that wear coefficient is dependent on sliding velocity and contact pressure. This agrees with observations from a curve at Älvsjö in Sweden, where wear measured at the rail gauge (high sliding velocity) was six times higher than on the rail head (low sliding velocity). In a pin-on-disc test, the wear rate in the so-called catastrophic wear regime was four times higher than in the mild regime. The wear rates measured in the field test were lower than in the laboratory due to differences in environmental control between the two tests (humidity, presence of biological material). Further, it was concluded that wear rates for R8T and R260 are similar to those for R7 and R260.

Thus, wear maps allow for the contributions of sliding velocity and contact pressure to the wear rate to be isolated and give an understanding of where transitions occur between acceptable and more severe wear conditions [3.1.27]. Wear maps for different wheel/rail material combinations have shown that there is a clear difference in wear rates in the severe wear regime. For example, comparing standard carbon rail material with R260, rail wear rates were reduced by an order of magnitude by using the latter material. In the mild wear regime, however, it was hard to distinguish any difference in wear rate between different material combinations. Note that, at present, available data required to set up detailed wear maps is very limited (in particular for combinations of high contact pressure and high sliding velocity and for materials other than R260). This calls for further measurements to increase understanding of the influence of material on wear coefficient and to extend the usefulness of wear maps and wear models.

A wear map for R260 is shown in Figure 3.1.20 [3.1.28]. Based on these measurements, a wear map was set up by Jendel [3.1.29], see Figure 3.1.21. The horizontal line is indicating the so-called seizure limit according to the original wear map suggested by Lim and Ashby [3.1.26]. This limit can be estimated by Tabor's equation [3.1.26] and is dependent on hardness and friction coefficient. The wear map in Figure 3.1.21 has been used as input in this study for predicting wear in switch panels with R260 rail grade. To account for the influence of field conditions (weather, contamination, lubrication, etc), all wear coefficients have been scaled down by a factor 5.5, see [3.1.29].

Unfortunately, data for R350HT are very scarce. However, according to [3.1.30] and based on two twin disc tests with one combination of contact pressure (1500 MPa) and sliding velocity (0.01 m/s, slip 1%), the Archard wear coefficient for R8T/R260 is about 8 times higher than for R8T/R350HT. The wear map in Figure 3.1.21 has been used also for predicting wear in switch panels with R350HT rail grade but wear coefficients have been divided by a factor 3 (a more conservative value compared to the single test referred to above) and the seizure limit has been raised due to the higher hardness. Note that these assumptions need to be verified by future measurements.

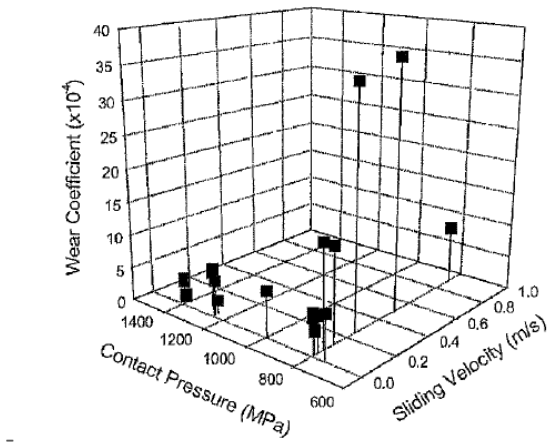

Figure 3.1.20. Wear coefficient map for wheel/rail combination R7 and R260 (dry conditions). From [3.1.28]

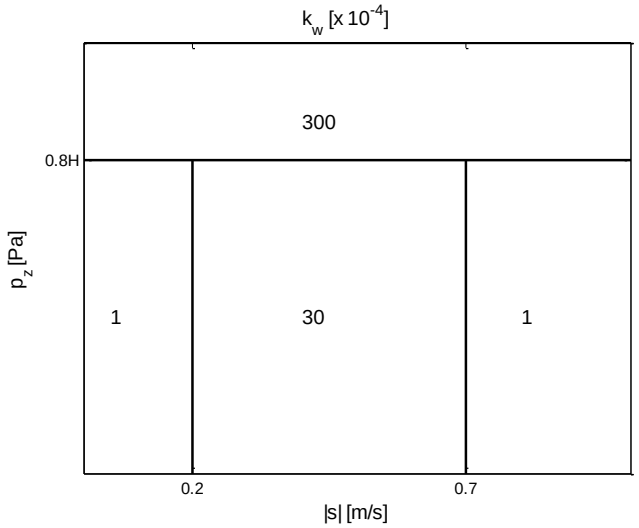

Figure 3.1.21. Map for coefficient k_w [×10^{-4}] in Archard's wear model. Based on laboratory measurements with wheel (R7) and rail (R260) steels, dry conditions, H = 3.4 GPa for run-in R260 rails (virgin material H = 2.7 GPa). For R350HT (run-in rails), it is assumed that all wear coefficients are reduced by a factor 3 and H = (350/260)*3.4 = 4.6 GPa

To predict RCF damage by the shakedown approach, the cyclic yield stress in shear *k* is required, see Equation (4). For rail grade R260, the yield stress in shear for work-hardened material is taken as *k* = 300 MPa [3.1.9].

Based on a database including laboratory measurements on 150 different non-austenitic steels, there is a linear correlation between the static yield strength in pure tension and Vickers hardness H_v, see Figure 3.1.22 [3.1.31]. This observation was used to derive a linear regression equation for the static yield strength in pure tension of non-martensitic steels.

$$\sigma_{\mathrm{Y}} = -84.8 + 2.646 H_{\mathrm{V}} \tag{6}$$

According to von Mises, the corresponding static yield strength in pure shear is obtained as

$$k_{\mathrm{stat}} = \sigma_{\mathrm{Y}} / \sqrt{3} \tag{7}$$

This results in k_{stat} = 370 MPa for R260 (H_{V}=274 GPa) and k_{stat} = 516 MPa for R350HT (H_{V}=370 GPa), corresponding to a ratio 1.4. Note that the static yield strength is normally higher than the cyclic yield strength.

For three levels of total strain amplitude (0.4, 0.6 and 1.0%), uniaxial, strain-controlled fatigue tests on R260 and R350HT specimens were performed in the INNOTRACK project [3.1.32, 3.1.33]. During the tests the maximum and minimum stress values were logged for each load cycle, see Figures 3.1.23 and 3.1.24. For R260, stable stresses were measured at *N*/2 as 465, 530 and 640 MPa, respectively. For R350HT, the corresponding stresses were 650, 750 and 885 MPa. This corresponds to a consistent ratio of about 1.4, which is in agreement with the ratio from the monotonic tests. In

the present study, for R350HT the cyclic yield stress in shear is taken as k = 1.4·300 = 420 MPa. Further, (based on the data for R260 and R350HT) it is here assumed that the cyclic yield stress for other rail grades can be obtained by linear inter/extrapolation depending on the Brinell hardness. Thus,

$$k = \frac{4}{3} H_B - 47 \quad \text{[MPa]} \tag{8}$$

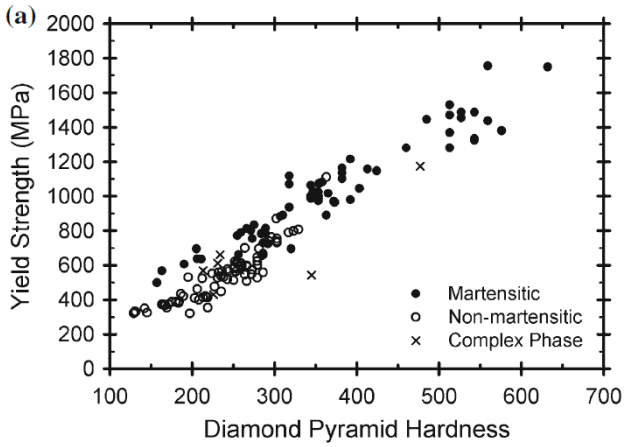

Figure 3.1.22. Influence of Vickers hardness on static yield strength in pure tension. From [3.1.31]

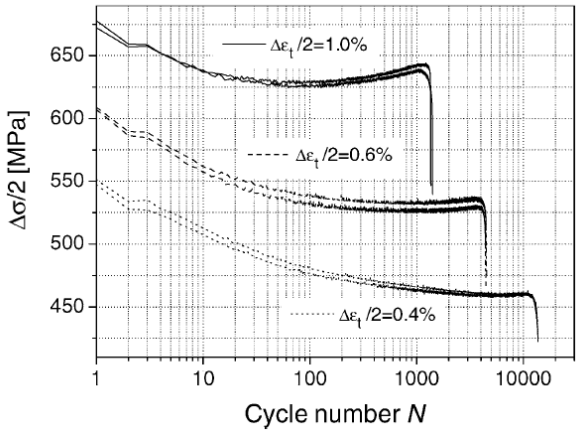

Figure 3.1.23. Stress amplitude versus cycle number in a uniaxial, strain-controlled fatigue test on rail grade R260. From [3.1.32]

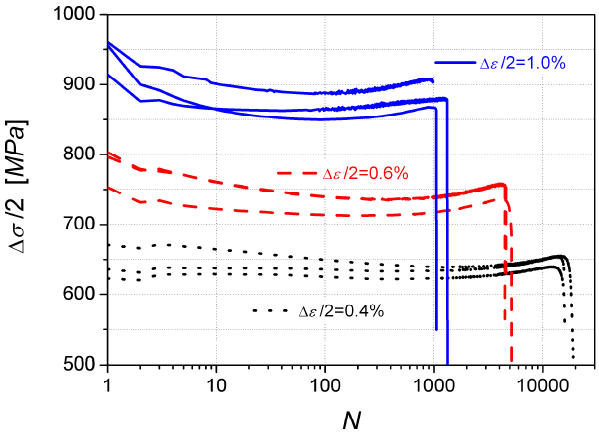

Figure 3.1.24. Stress amplitude versus cycle number in a uniaxial, strain-controlled fatigue test on rail grade R350HT. From [3.1.33]

As described in Section 3.1.2, an alternative approach to predict RCF on rails is to relate a RCF damage index to the energy dissipation $T\gamma$ in the wheel-rail contact (neglected influence of spin) [3.1.13]. Based on validation of this model versus field observations of surface initiated RCF on various curves with rail grade R260 or R350HT, the multi-linear damage functions in Figure 3.1.25 were derived [3.1.14]. In this study, the model based on shakedown theory is used but the predicted damage is multiplied with a penalty function $f_p(T\gamma)$ that is reflecting the damage index in Figure 3.1.25. Thus, for all grid elements of a given contact patch, it is assumed that there is no RCF damage if $T\gamma$ evaluated for the complete contact patch exceeds the threshold value (175 J/m for R260 and 400 J/m for R350HT), see Figure 3.1.26. Note that the empirical functions in Figures 3.1.25 and 3.1.26 were derived for wheel-rail contact conditions in curves and may not be representative for the wheel-rail contact conditions in a switch panel. Note that these assumptions need to be verified by future measurements.

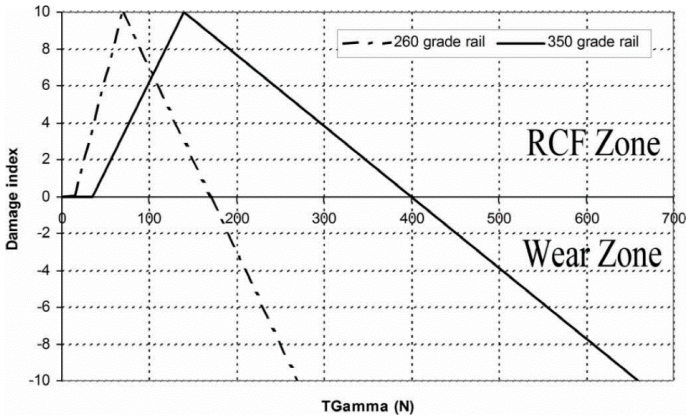

Figure 3.1.25. Empirical assessment of RCF damage index based on energy dissipation in the wheel–rail contact. From [3.1.14]

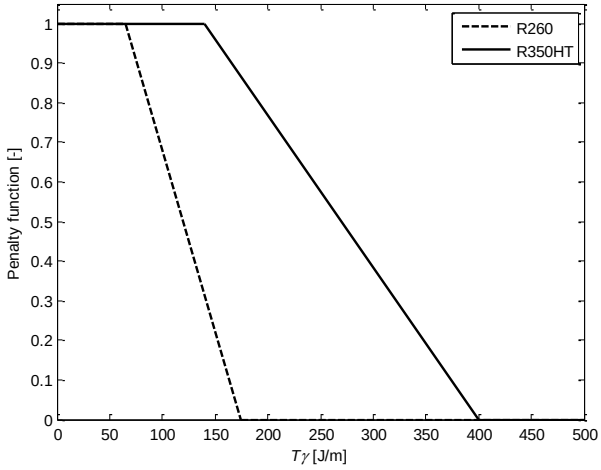

Figure 3.1.26. Penalty function applied in evaluation of surface-initiated RCF damage for rail grades R260 and R350HT

3.1.5 VEHICLE-TRACK INTERACTION MODEL

Dynamic interaction between vehicle and the switch panel of a railway turnout is studied in the time domain using the commercial software GENSYS [3.1.34]]. The vehicle model represents a freight vehicle (one car) with Y25 bogies and axle load 25 tonnes. For a detailed description of this vehicle and the simulation set-up, see [3.1.35, 3.1.36]. For traffic in the through route, the nominal vehicle speed is 100 km/h, whereas for traffic in the diverging route the speed is 70 km/h. The geometry of the nominal (reference) turnout is the standard design 60E1-760-1:15 with rail profile 60E1 (rail inclination 1:30 and a 60° chamfer milled on the front section of the switch rail), curve radius 760 m and turnout angle 1:15. In nominal configuration, the switch rails begin at 805 mm from the start of the turnout.

The track flexibility is modelled by systems of springs and dampers, with one such moving system following each wheelset. Each track model consists of two rails with neglected inertia that are attached to rigid ground by linear spring-damper elements in the lateral and vertical directions to account for the stiffness of the track. The vertical track properties used here are taken from track model TM1 in [3.1.37] with input data based on the measured track stiffness in a turnout using the rolling stiffness measurement vehicle developed by the Swedish Transport Administration (Trafikverket) [3.1.38]. The vertical track stiffness between rail and ground is 60 kN/mm and the viscous damping coefficient is 535 kNs/m. The corresponding stiffness and damping in the lateral direction were not available from these measurements but are set to 30 kN/mm and 270 kNs/m, see the discussion in [3.1.3]. The properties of the moving track models are taken as independent of the position along the switch panel. Note that this simple track representation, with neglected track inertia, should be sufficiently accurate as vehicle dynamics in the switch panel is dominated by low frequencies (< 20 Hz) [3.1.37].

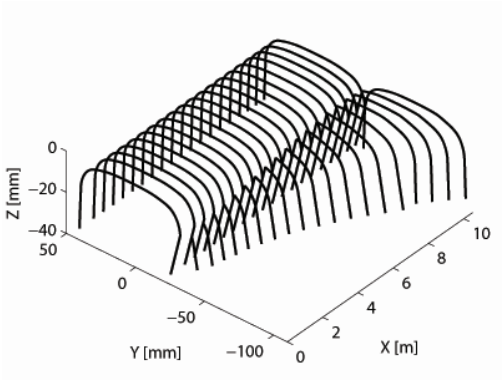

Figure 3.1.27. Switch rail assembly based on 60E1 rail profile, no rail inclination and nominal milling tool path

The manufacturing process of a switch rail is briefly described in [3.1.4]. For a given tool profile, the complete switch rail is milled from a nominal stock rail profile as determined by the prescribed vertical and lateral motion of the tool along the longitudinal milling tool path. In addition, the front part of the switch rail is milled to generate a 60° chamfer to avoid contact with the wheel flange where the switch rail is thin.

Using an in-house computer program inspired by this manufacturing process, the switch rail profile geometry is parameterised in two levels, see [3.1.4]. The milling tool profile is parameterised using a B-spline, and the vertical milling tool path for the profiling tool is parameterised by adding a deviation from the nominal profiling path. The implemented nominal design is based on drawing 9-511401 (Trafikverket), which describes a turnout with 60E1 rails with no rail inclination. However, alternative switch rail designs can also be generated by setting different parameters for the tool profile and the tool path. Based on this procedure, and for any given combination of rail profile, rail inclination and selected vertical milling tool path, the variation in rail profile in the switch panel is here represented by 68 pairs of rail cross-sections (one set of rail cross-sections per rail side). The stock rail and switch rail assembly is considered as rigid. Note that the switch rail is manufactured from a rail with the same inclination as the stock rail but the tool profile is not rotated.

One example of a generated nominal rail assembly is illustrated in Figure 3.1.27. Samples of rail profiles created by the in-house program are compared with the corresponding rail sections supplied by Vossloh Cogifer (representing the INNOTRACK turnout at Eslöv in Sweden with rail inclination 1:30) in Figure 3.1.28. Good agreement between the generated sections and the true profiles is observed (the small deviations are mainly explained by small differences in longitudinal coordinates for the Vossloh and generated profiles). This serves as a validation of the in-house program, which will be used to generate also other switch panel designs with different combinations of stock rail profile and rail inclination.

For each combination of wheel profile and rail cross-section, the wheel-rail contact geometry problem is solved in advance using the GENSYS module KPF. Based on a linear interpolation procedure between rail sections, tabulated contact geometry functions are used in the subsequent

time integration analysis. Further, each wheel-rail contact is modelled by a Hertzian spring with linearised stiffness 1500 kN/mm in the normal direction and an implementation of Kalker's simplified theory FASTSIM [3.1.39] in the tangential direction. The software accounts for the two-point contact situations occurring on the stock and switch rail assembly.

Time histories of normal and tangential forces, creepages and positions for each wheel–rail contact are calculated with a sampling frequency of 1 kHz. All results are then filtered with a low-pass (fourth-order Butterworth) filter with cut-off frequency 20 Hz before calculating the damage (wear and RCF).

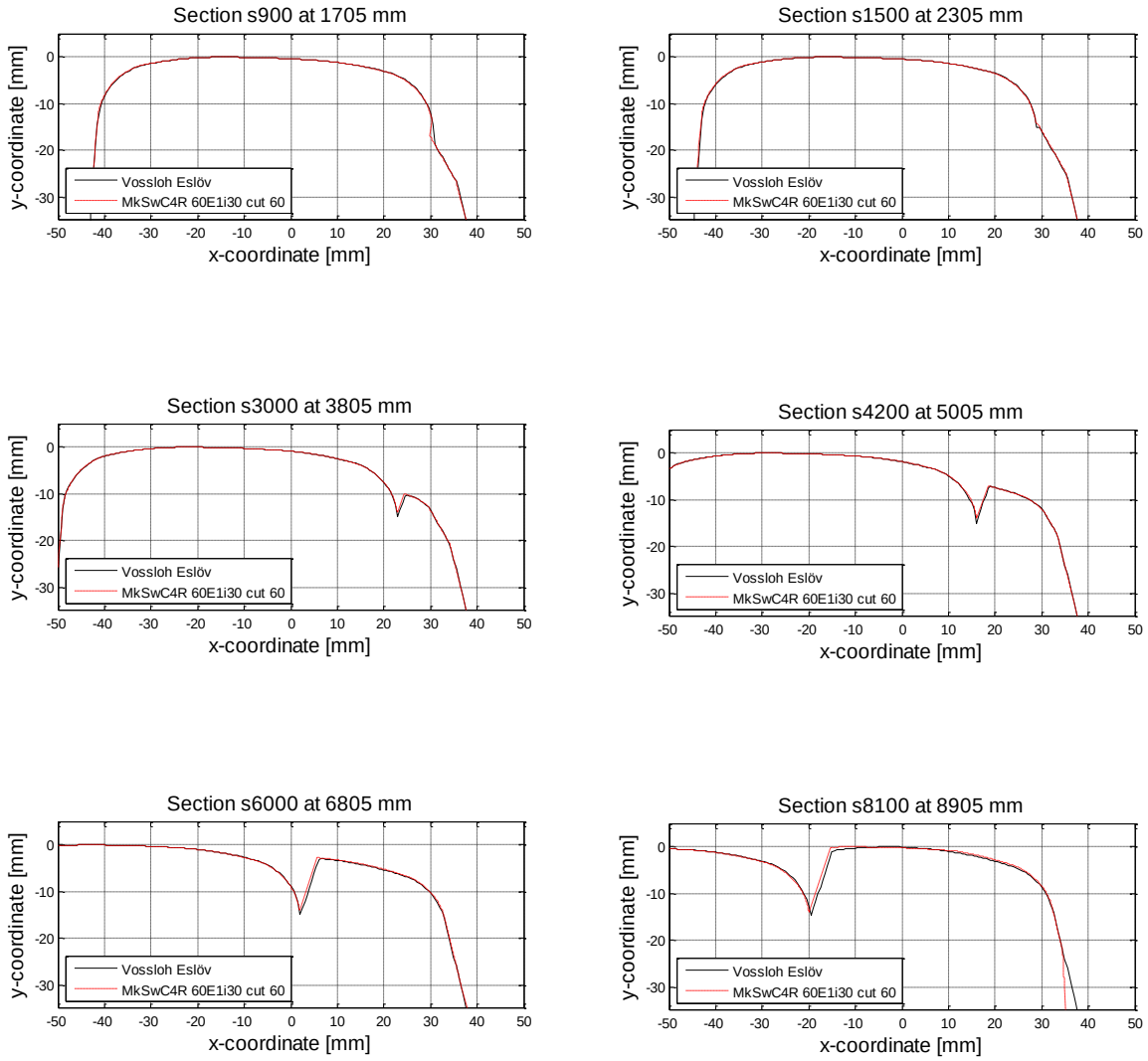

Figure 3.1.28. Samples of rail profile in the switch panel. Comparison of rail profiles generated by parameterised in-house program and rail profiles supplied by Vossloh Cogifer representing the INNOTRACK turnout at Eslöv in Sweden with 60E1 stock rail profile and rail inclination 1:30

3.1.6 SWITCH RAIL PROFILE, RAIL INCLINATION AND RAIL GRADE

The influence of switch rail profile and rail inclination on damage in the switch panel has been investigated using the model described in the previous sections. Two rail inclinations (vertical rails and 1:30) and the influence of a 60° chamfer along the front section (up to 4.98 m from the switch rail tip) of the switch rail have been studied. Examples of rail cross-sections from the three different designs used as input are compared in Figure 3.1.29.

For freight traffic in facing move of the diverging route at speed 70 km/h, and with nominal (non-worn) S1002 wheel profiles, time histories of $T\gamma$ and contact positions on the rails are illustrated in Figure 3.1.30 (leading wheel in leading bogie) and Figure 3.1.31 (trailing wheel in leading bogie). The shaded area indicates the range of $T\gamma$-values that according to Figure 3.1.25 corresponds to the RCF zone for rail grade R260. In particular, the horizontal dashed line within the shaded area indicates the $T\gamma$-value where there is a maximum in RCF damage. Rail inclination has a significant influence on contact position on the stock rail, see Figures 26(a) and 27(a), but not for the contact position on the switch rail since the switch rail profile is the same independent of rail inclination, see Figures 26(b) and 27(b). Further, it is observed in Figure 3.1.30(b) and Figure 3.1.31(b) that there is two-point wheel-rail contact for both leading and trailing wheels from about 4 m to 9 m from the front of the turnout. Thus, the full transition to the switch rail occurs at about 9 m from the front of the turnout for all the studied switch panel designs. Two-point contact occurs slightly earlier for the inclined rail (60E1i30) and in particular if there is no 60° chamfer. Very high values of $T\gamma$ (and normal contact pressure, not shown here) are generated in the contact between wheel flange and switch rail indicating that the dominating damage mechanism is wear (wear zone in Figure 3.1.25). For the contact between wheel tread and stock rail (during the situation with two-point contact), the leading wheel generates $T\gamma$-values in the upper end of the RCF zone (see Figure 3.1.30(a)), whereas the trailing wheel generates $T\gamma$-values closer to the maximum in the RCF damage function (see Figure 3.1.31(a)). Thus, for this load case, it is concluded that the maximum wear damage is generated on the switch rail due to contact with the wheel flange of both leading and trailing wheels. Further, RCF damage on the stock rail before the full transition to the switch rail is mainly generated by the trailing wheel (see Figure 3.1.31(a)), whereas the RCF damage on the switch rail after the full transition to the switch rail is generated by the leading wheel (see Figure 3.1.30(a)).

The corresponding plots for freight traffic in trailing move of the diverging route are shown in Figure 3.1.32 (leading wheel in leading bogie) and Figure 3.1.35 (trailing wheel in leading bogie). It is observed that the leading wheel is in two-point contact from about 9 m to 2 m from the front of the turnout, whereas the trailing wheel is generally only making one-point contact. The model indicates there is intermittent (irregular) contact between wheel flange and switch rail when there is a 60° chamfer, and that severe wear damage is generated (high $T\gamma$-values, see Figure 3.1.32(b)). The leading wheel generates severe RCF damage on the stock rail while there is two-point contact ($T\gamma$-values close to the maximum in the RCF damage function), see Figure 3.1.32(a). The trailing wheel generates low damage (both wear and RCF), see Figure 3.1.33.

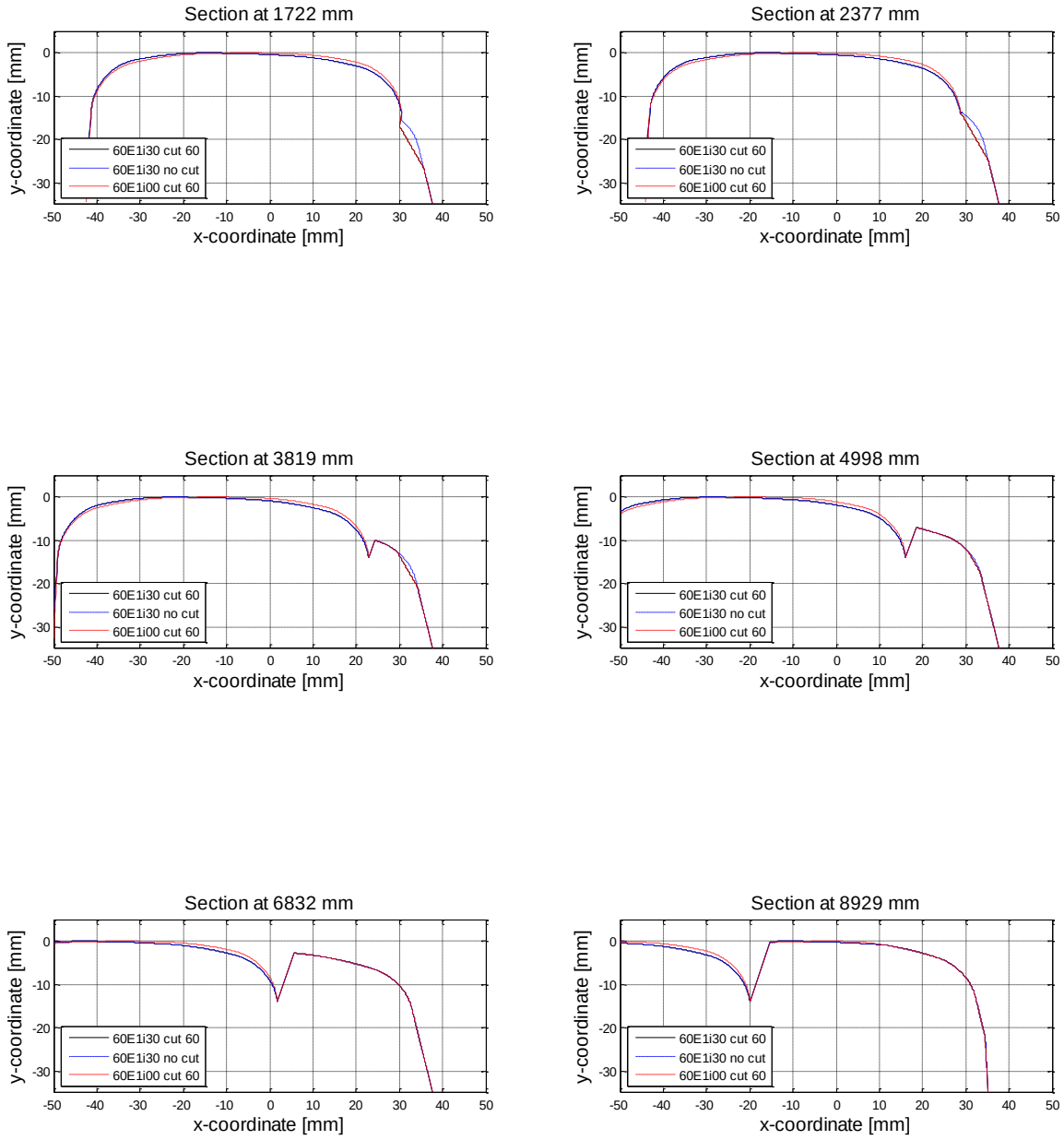

Figure 3.1.29. Samples of rail profile in the switch panel. Comparison of rail profiles generated by in-house computer program: two different rail inclinations and with or without 60° chamfer

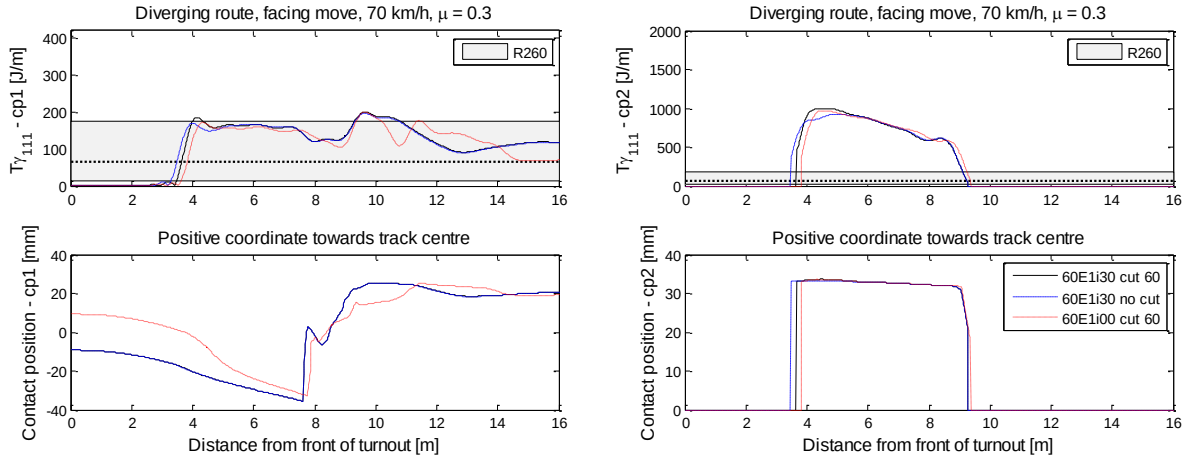

(a) (b)

Figure 3.1.30. Influence of rail inclination and 60° chamfer on damage function Tγ and contact position (two contact points) in diverging route. S1002 wheel profile, vehicle speed 70 km/h, friction coefficient 0.3. Leading wheel in leading bogie, facing move

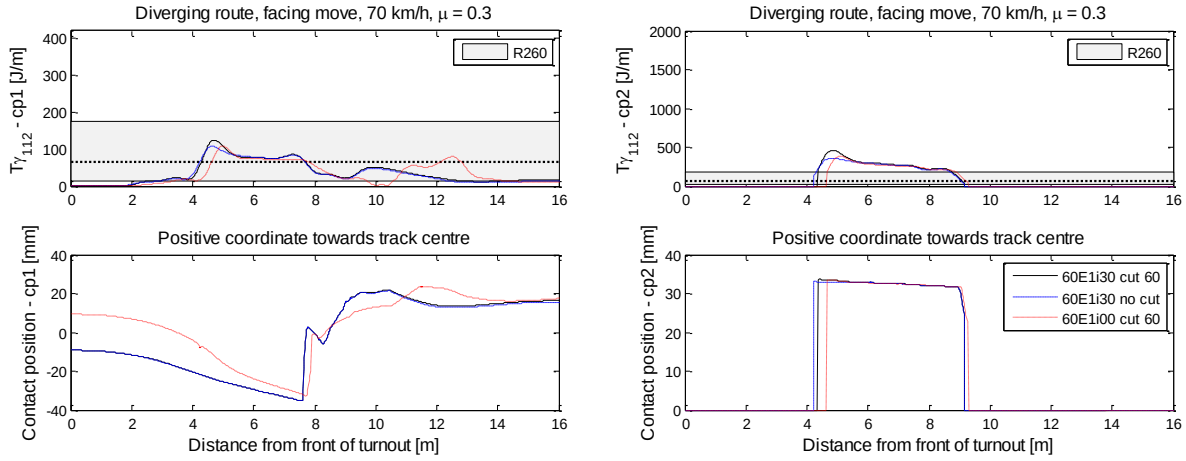

(a) (b)

Figure 3.1.31. Influence of rail profile and rail inclination on damage function Tγ and contact position (two contact points) in diverging route. S1002 wheel profile, vehicle speed 70 km/h, friction coefficient 0.3. Trailing wheel in leading bogie, facing move

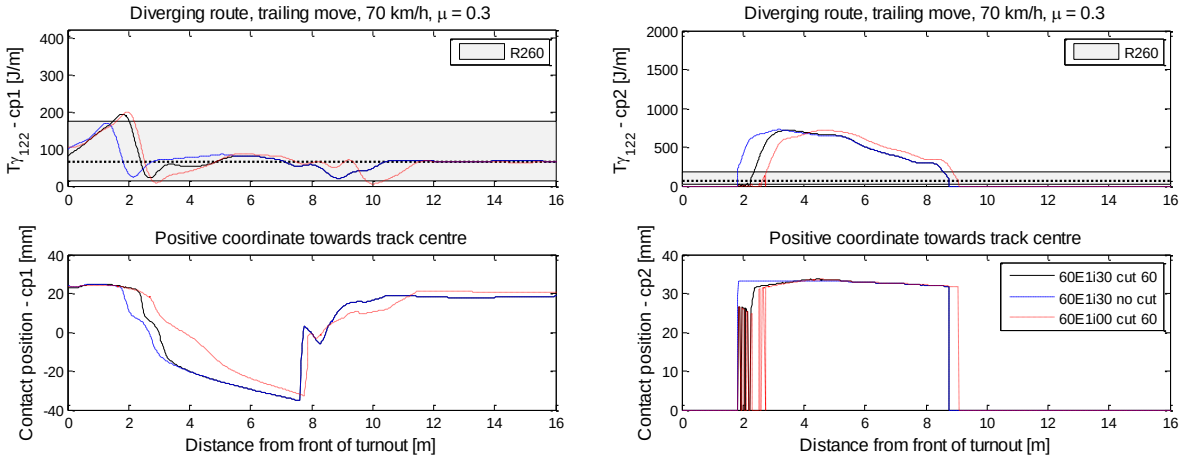

(a) (b)

Figure 3.1.32. Influence of rail profile and rail inclination on damage function Tγ and contact position (two contact points) in diverging route. S1002 wheel profile, vehicle speed 70 km/h, friction coefficient 0.3. Leading wheel in leading bogie, trailing move

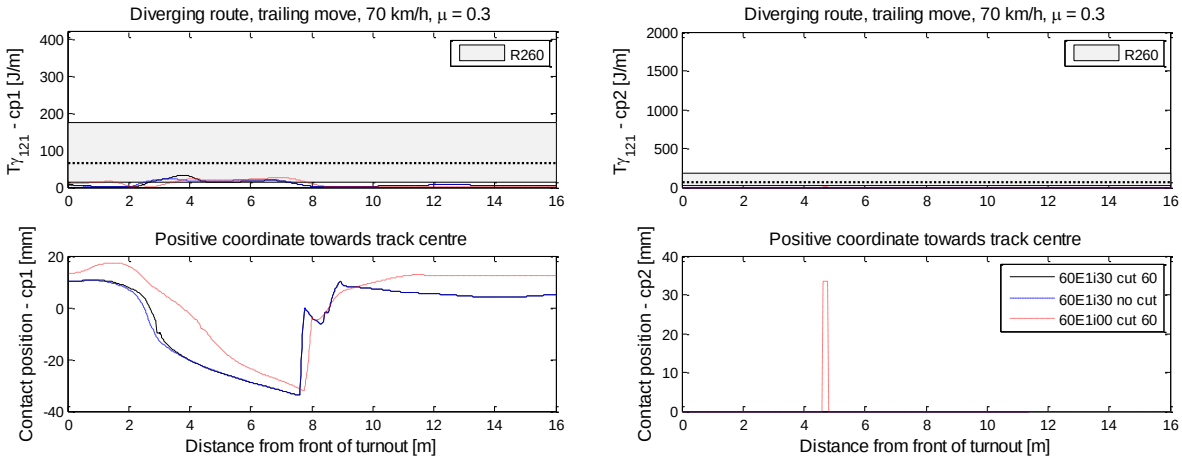

(a) (b)

Figure 3.1.33. Influence of rail profile and rail inclination on damage function Tγ and contact position (two contact points) in diverging route. S1002 wheel profile, vehicle speed 70 km/h, friction coefficient 0.3. Trailing wheel in leading bogie, trailing move

Table 3.1.1. Influence of rail profile and rail inclination on maximum accumulated wear and RCF damage for one Y25 vehicle (four wheelsets) in diverging route. S1002 wheel profile, vehicle speed 70 km/h, friction coefficient 0.3. Damage is normalised with respect to damage calculated for the case marked with grey colour

Rail profile	Move	Max wear [μm]	Position [m]	Max RCF damage [10^{-6}]	Position [m]	Max wear [μm]	Position [m]	Max RCF damage [10^{-6}]	Position [m]
		R260				R350HT			
60E1i30 cut 60	Facing	1	x=5.12 m y=3.33 cm	1	x=5.64 m y=3.27 cm	0.15	x=4.45 m y=3.37 cm	2.68	x=4.35 m y=3.37 cm
60E1i30 no cut	Facing	0.90	x=5.06 m y=3.31 cm	1.51	x=4.24 m y=3.31 cm	0.08	x=3.66 m y=3.33 cm	2.48	x=4.24 m y=3.31 cm
60E1i00 cut 60	Facing	1.38	x=4.73 m y=3.35 cm	3.92	x=9.60 m y=1.17 cm	0.18	x=4.67 m y=3.35 cm	3.08	x=10.96 m y=1.85 cm
60E1i30 cut 60	Trailing	1.10	x=4.06 m y=3.35 cm	1.34	x=8.66 m y=3.17 cm	0.16	x=4.06 m y=3.35 cm	1.31	x=1.01 m y=2.47 cm
60E1i30 no cut	Trailing	1.50	x=2.35 m y=3.33 cm	3.08	x=2.60 m y=3.31 cm	0.24	x=2.55 m y=3.33 cm	3.64	x=1.84 m y=2.93 cm
60E1i00 cut 60	Trailing	1.13	x=4.67 m y=3.35 cm	2.80	x=2.55 m y=1.95 cm	0.15	x=4.19 m y=3.35 cm	2.80	x=2.37 m y=2.11 cm

The calculated accumulated damage (wear and RCF) due to the passage of one vehicle (four wheelsets with nominal S1002 wheel profiles) in either facing or trailing move is summarised in Table 3.1.1. The calculated damage has been normalised with respect to the corresponding damage calculated for the inclined rail with 60° chamfer (60E1i30 cut 60) and rail grade R260 in facing move traffic (shaded area). For comparison, damage has also been calculated assuming rail grade R350HT. The positions (longitudinal coordinate measured from the front of the turnout and lateral coordinate on the rail, see Figure 3.1.29 for reference) of calculated damage maxima are also presented in the table. Based on the calculated results, the following conclusions can be made:

- Wear is significantly reduced by selecting R350HT instead of R260. This is as expected as it has been assumed that R350HT corresponds to a factor 3 lower wear coefficients and the higher hardness of R350HT raises the seizure limit in the wear map, see Figure 3.1.21.
- The maximum wear damage is generated on the side of the switch rail, typically at 4.5 – 5 m from the front of the turnout). However, for the design without the 60° chamfer the position of maximum wear in trailing move is shifted closer to the switch rail tip where the switch rail is thinner.
- The 60° chamfer leads to increased wear in the facing move.

- There seems to be no clear correlation between initiation of RCF damage and rail grade selection. Depending on rail profile design and move, RCF damage may increase or decrease when selecting R350HT instead of R260. This can be explained by the assumed penalty function, see Figure 3.1.26, which depending on rail grade scales the evaluated RCF damage. For the higher rail grade, the evaluated $T\gamma$ may be closer to the maximum in the RCF damage function.
- The inclined rail profile leads to reduced damage (both wear and RCF) compared to the vertical profile for all cases except one (wear in trailing move, R350HT).
- The 60° chamfer reduces wear and RCF damage in the trailing move.
- The rail inclination has a significant influence on the position of maximum RCF damage.

The influence of switch rail profile and rail inclination on damage in the switch panel has also been investigated for a traffic situation with a more representative selection of measured (worn) wheel profiles. Ten wheel profiles were sampled (Latin hypercube sampling) from a pool of 120 profiles measured on 120 unique and randomly selected Y25 wheelsets. To obtain the representative selection, before sampling the wheel profiles were sorted with respect to equivalent conicity $\lambda_{\mathrm{eq,3mm}}$ as this has been shown to be the wheel profile parameter correlating best to damage in S&C [3.1.40].

The scalar damage value D_i^{w} (i = 1, 2, 3 and 4), see Equation (2), was evaluated for each wheel passage i and each contact point to determine which wheel profile is the most detrimental to the switch panel. Note that the damage value is a weighted average of $T\gamma$ evaluated along the switch panel (1 – 11 m from the front of the turnout). Thus, while providing a penalty to high local values, it does not necessarily indicate which wheel profile generates the maximum local damage. For traffic in facing move and for each combination of wheel profile, switch rail profile and rail inclination, the maximum value D^{w} evaluated for all four wheels in the vehicle model is shown in Figure 3.1.34. It was observed (not shown here) that the maximum value was always generated by the leading wheel in the leading bogie. Further, it is noted in Figure 3.1.34 that all wheels generate maximum D^{w}-values in the same order of magnitude although wheel profile 4 is slightly worse than the other profiles. It is observed that the influence of switch rail profile and rail inclination on D^{w} is moderate. The corresponding plot for traffic in trailing move is presented in Figure 3.1.35. In this case, it was observed (not shown here) that the maximum value was always generated by the leading wheel in the trailing bogie.

Calculated accumulated damage (wear and RCF) due to the passage of 10 vehicles (total of 40 wheelsets and each vehicle with a different worn wheel profile) in either facing or trailing move is summarised in Table 3.1.2. Again, the calculated damage has been normalised with respect to the corresponding damage calculated for the inclined rail with 60° chamfer (60E1i30 cut 60) and rail grade R260 in facing move traffic (shaded areas). The variation in wheel profile leads to a more realistic distribution of wheel-rail contact positions (a wider running band). In comparison with the nominal S1002 profile, the worn wheel profiles can make contact with the switch rail closer to the front of the turnout. The damage has also been calculated assuming rail grade R350HT. The following conclusions can be made:

- Wear is reduced significantly by selecting R350HT instead of R260 (same conclusion as for the case with S1002 profiles).
- The maximum wear damage is generated on the switch rail (same conclusion as for the case with S1002 profiles). For the switch rails with the 60° chamfer, the use of worn wheel profiles leads to a shift of the position of maximum wear closer to the switch rail tip, compare Tables 1 and 2.
- Wear and RCF damage are higher in the trailing move.
- The 60° chamfer leads to increased wear in both moves.
- RCF damage increases with the selection of R350HT. As discussed above, this is a consequence of the assumed penalty function. To confirm that this is a correct result, the penalty function (RCF damage function) needs to be calibrated for switch panels in the field.
- The inclined rail profile leads to significantly reduced RCF damage compared to the vertical profile for both moves and both rail grades. However, the wear on the switch rail is in most cases slightly increased by the inclined stock rail.
- The maximum RCF damage in facing move is on the switch rail in the area where the full wheel transition to the switch rail has just occurred, while the maximum RCF damage in trailing move is on the stock rail in the area where the full wheel transition to the stock rail has just occurred.

To summarise, the calculations show that the design with inclined rails (1:30) is superior to the case with vertical rails. However, it seems that the 60° chamfer of the switch rail does not have a positive effect. It is possible that this chamfer design would be improved by adding also a so-called secondary cut where the vertical milling tool path is changed to reduce the height of the front sections of the switch rail. The use of R350HT instead of R260 leads to a significant reduction in wear although the results obtained here indicate are more dramatic reduction than has been observed in the field. This is probably explained by the lack of input data in the wear maps for both rail grades, in particular for R350HT and for combinations with high contact pressure and high sliding velocity. The predicted positions of maximum RCF damage and the influence of rail grade on RCF damage (R350HT leads to increased RCF damage compared to R260) need to be confirmed by field observations.

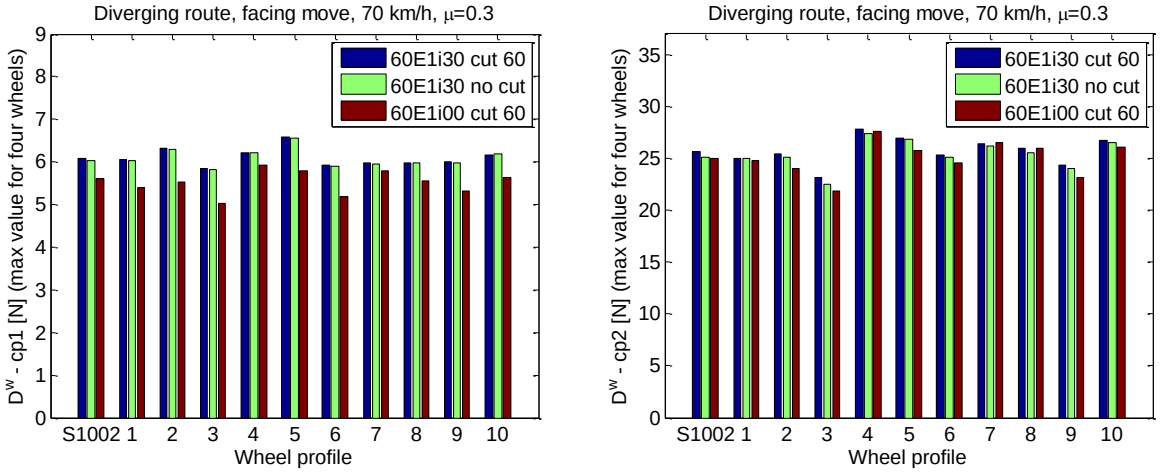

(a) (b)

Figure 3.1.34. Influence of wheel profile, switch rail profile and rail inclination on damage value D – maximum value evaluated for all four wheels in vehicle model (two contact points). Diverging route, facing move, vehicle speed 70 km/h, friction coefficient 0.3

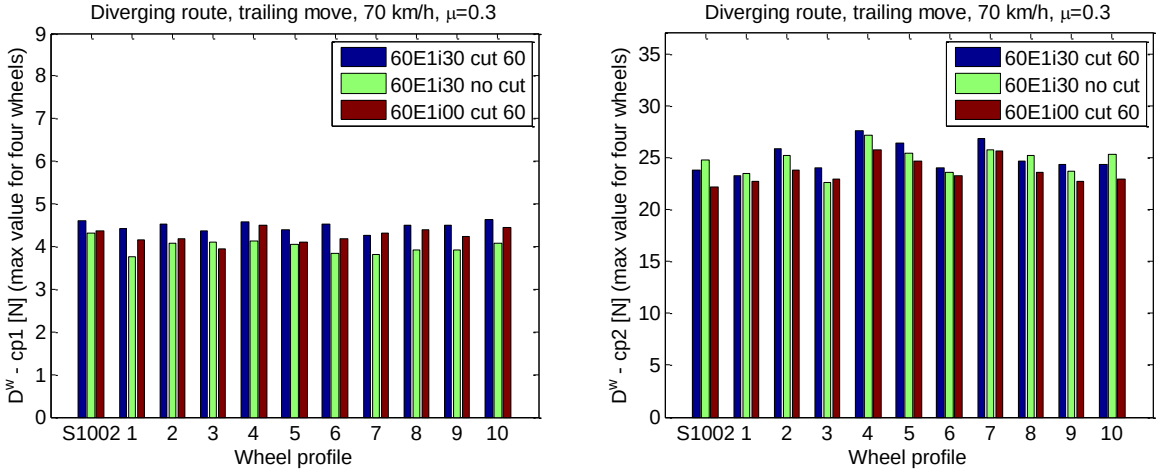

(a) (b)

Figure 3.1.35. Influence of wheel profile, switch rail profile and rail inclination on damage value D – maximum value evaluated for all four wheels in vehicle model (two contact points). Diverging route, trailing move, vehicle speed 70 km/h, friction coefficient 0.3

Table 3.1.2. Influence of rail profile and rail inclination on maximum accumulated wear and RCF damage for 10 Y25 vehicles (40 wheelsets) in diverging route. 10 combinations of worn wheel profile and vehicle speed 70 km/h. Friction coefficient 0.3. Damage is normalised with respect to damage calculated for the case marked with grey colour

Rail profile	Move	Max wear [μm]	Position [m]	Max RCF damage [10^{-6}]	Position [m]	Max wear [μm]	Position [m]	Max RCF damage [10^{-6}]	Position [m]
		R260				R350HT			
60E1i30 cut 60	Facing	1	x=4.14 m y=3.39 cm	1	x=9.23 m y=2.15 cm	0.08	x=3.97 m y=3.41 cm	2.88	x=10.47 m y=2.43 cm
60E1i30 no cut	Facing	0.26	x=3.91 m y=3.35 cm	1.06	x=9.18 m y=2.19 cm	0.04	x=5.86 m y=3.31 cm	3.23	x=10.82 m y=2.41 cm
60E1i00 cut 60	Facing	1.09	x=4.69 m y=3.37 cm	2.18	x=10.88 m y=1.79 cm	0.07	x=4.07 m y=3.39 cm	4.72	x=10.98 m y=1.87 cm
60E1i30 cut 60	Trailing	2.70	x=3.93 m y=3.41 cm	2.97	x=2.33 m y=1.99 cm	0.19	x=3.36 m y=3.43 cm	4.06	x=2.00 m y=2.21 cm
60E1i30 no cut	Trailing	1.26	x=3.01 m y=3.37 cm	2.15	x=1.77 m y=2.21 cm	0.07	x=2.06 m y=3.35 cm	5.02	x=1.44 m y=2.33 cm
60E1i00 cut 60	Trailing	2.33	x=3.98 m y=3.41 cm	6.66	x=2.44 m y=1.95 cm	0.17	x=3.51 m y=3.43 cm	6.81	x=2.24 m y=2.07 cm

3.1.7 FRICTION MANAGEMENT

The influence of friction coefficient in the wheel-rail interface on damage in the switch panel has been investigated using the model described in the previous sections. The studied switch panel design is the reference design in Section 3.1.6 with the 1:30 inclined rails and the 60° chamfer of the front section of the switch rail. The background for this investigation is the possibility to use friction management in the switch panel with a friction coefficient designed to be on a moderate level (in the order of 0.3) independent of weather conditions.

For freight traffic in facing move of the diverging route at speed 70 km/h, and with nominal (non-worn) S1002 wheel profiles, time histories of $T\gamma$ and contact positions on the rails are illustrated in Figure 3.1.36 (leading wheel in leading bogie). The shaded area indicates the range of $T\gamma$-values that according to Figure 3.1.25 corresponds to the RCF zone for rail grade R260. In particular, the horizontal dashed line within the shaded area indicates the $T\gamma$-value where there is a maximum in RCF damage. Very high values of $T\gamma$ are observed on the switch rail during two-point contact and $T\gamma$ is increasing with increasing wheel-rail friction, see Figure 3.1.36(b). Contact positions on the rails are

only influenced by friction coefficient after the full transition to the switch rail. Based on the damage function for R260 in Figure 3.1.25, there is no RCF damage on the switch rail during two-point contact for any studied value of friction coefficient. RCF damage may occur on the stock rail during two-point contact and on the switch rail after the transition to one-point contact, and in particular for the low friction coefficient as the *Tγ*-values are close to the maximum in the RCF damage function. However, the high *Tγ*-values indicate that RCF is to some degree suppressed by wear.

The tangential forces in the wheel-rail contact (in longitudinal and lateral directions) are presented in Figure 3.1.37. During two-point contact (from about 3.5 m to 9 m from the front of the turnout), the longitudinal wheel-rail contact force on the stock rail is acting in positive X-direction (same as facing move) and in the negative X-direction on the switch rail, see Figure 3.1.37(a). The lateral (in the contact plane) wheel-rail contact forces on stock rail and switch rail are acting towards the inside of the curve, see Figure 3.1.37(b). The magnitudes of the tangential contact forces are increasing with increasing friction. Calculated levels of FI_{surf} indicates RCF damage impact on both rails during two-point contact and on the switch rail after the transition to one-point contact, see Figure 3.1.38. The damage index FI_{surf} is increasing significantly with increasing wheel-rail friction. However, as stated above, note that FI_{surf} does not account for the influence of wear on crack growth.

Figures 3.1.39 – 3.1.41 illustrate the corresponding results for the trailing wheel in the leading bogie, while Figures 3.1.42 – 3.1.47 present the corresponding results for the leading and trailing wheels in the leading bogie in trailing move. It is concluded that friction management to maintain a controlled friction level and avoid situations with dry wheel-rail contact conditions with high friction coefficients has a significant potential to reduce energy dissipation, tangential contact forces and damage (wear and RCF) in the wheel-rail contacts.

The calculated accumulated damage (wear and RCF) due to the passage of one vehicle (four wheelsets with nominal S1002 wheel profiles) in either facing or trailing move is summarised in Table 3.1.3. As in Table 3.1.1, the calculated damage has been normalised with respect to the corresponding damage calculated for the reference switch panel design (60E1i30 cut 60) with rail grade R260 and friction coefficient 0.3 in facing move traffic (shaded areas). For comparison, damage has also been calculated assuming rail grade R350HT. The positions (longitudinal coordinate measured from the front of the turnout and lateral coordinate on the rail, see Figure 3.1.29 for reference) of calculated damage maxima are presented in the table. The following conclusions can be made:

- Wear is reduced significantly by selecting rail grade R350HT instead of R260.
- Wear is reduced by maintaining a low friction coefficient in the wheel-rail contacts. Note that according to the Archard model, wear is only occurring in sliding contact.
- Independent of friction coefficient and move, the maximum wear damage is generated on the side of the switch rail at 4 – 5 m from the front of the turnout.
- RCF damage (prediction based on shakedown theory and the use of a penalty function to suppress damage in cases with very high energy dissipation *Tγ*) is reduced significantly by maintaining a low friction coefficient in the wheel-rail contact. In particular, cases with dry wheel-rail contact (high friction) lead to very high RCF damage impact.

- In facing move, for friction coefficient ≤ 0.3 the maximum RCF damage occurs on the switch rail at about 3.5 – 5.5 m from the front of the turnout (during two-point contact). For higher friction coefficients, the maximum RCF damage occurs on the switch rail after the full wheel transition from the stock rail (about 10 – 11 m from the front of the turnout).
- In trailing move, the maximum RCF damage is generally occurring on the stock rail after the full wheel transition from the switch rail (about 1 – 2.5 m from the front of the turnout).

Calculated accumulated damage (wear and RCF) due to the passage of 10 vehicles (total of 40 wheelsets and each vehicle with a different worn wheel profile) in either facing or trailing move is summarised in Table 3.1.4. The damage has also been calculated assuming rail grade R350HT. The following conclusions can be made:

- Wear is reduced significantly by selecting rail grade R350HT instead of R260 (same conclusion as for the case with S1002 profiles).
- Wear is reduced by maintaining a low friction coefficient in the wheel-rail contacts (same conclusion as for the case with S1002 profiles).
- Independent of friction coefficient and move, the maximum wear damage is generated on the side of the switch rail. However, in contract to the case with S1002 profiles, the position of maximum wear is shifted closer to the switch rail tip to about 3 – 4.5 m from the front of the turnout.
- RCF damage is reduced significantly by maintaining a low friction coefficient in the wheel-rail contact. In particular, cases with dry wheel-rail contact (high friction) lead to very high RCF damage impact (same conclusion as for the case with S1002 profiles).
- In facing move, independent of friction coefficient, the maximum RCF damage occurs on the switch rail after the full wheel transition from the stock rail (about 9 – 11 m from the front of the turnout).
- In trailing move, independent of friction coefficient, the maximum RCF damage occurs on the stock rail after the full wheel transition from the switch rail (at about 2 m from the front of the turnout).

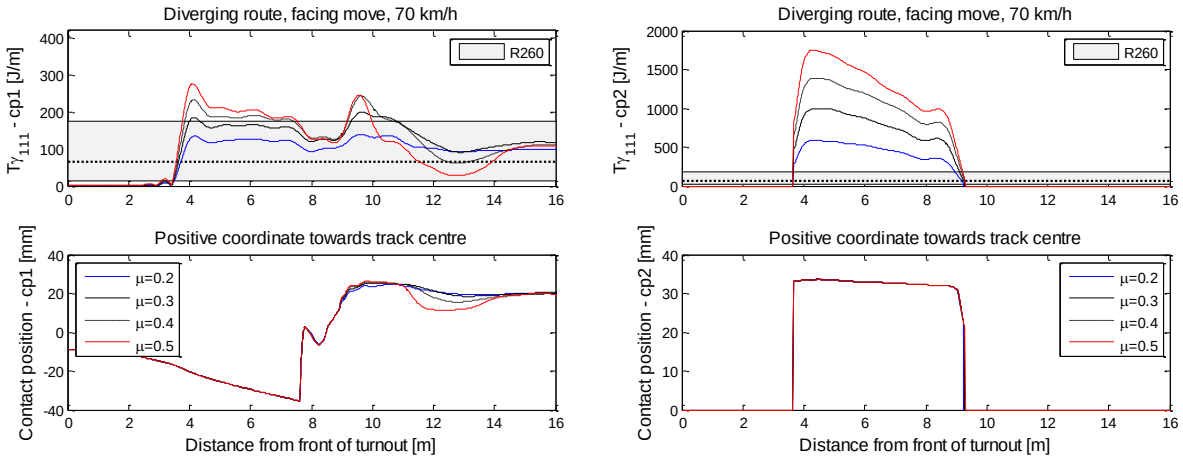

(a) (b)

Figure 3.1.36. Influence of friction coefficient on damage function Tγ and contact position (two contact points) in diverging route. S1002 wheel profile, vehicle speed 70 km/h, rail profile 60E1i30 cut 60. Leading wheel in leading bogie, facing move

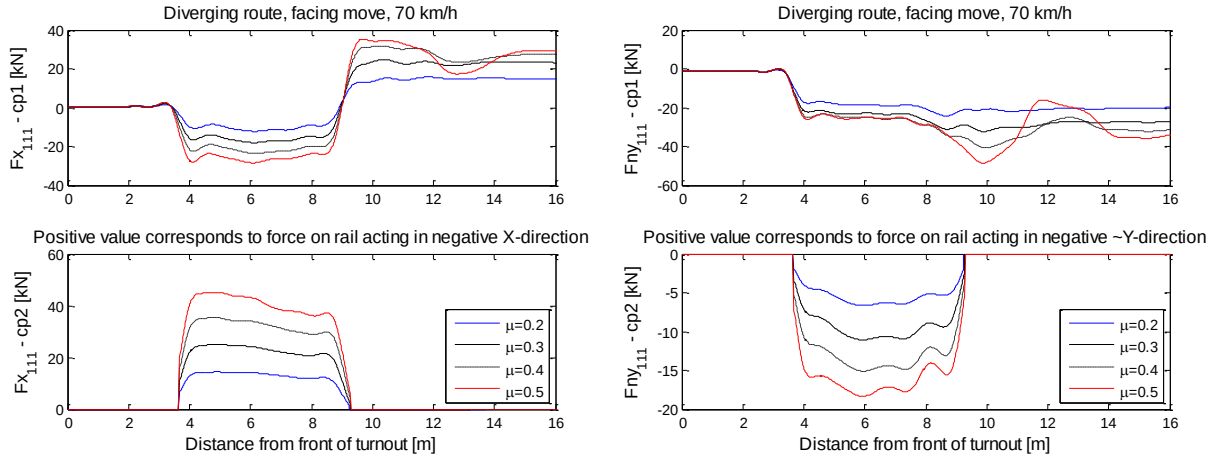

(a) (b)

Figure 3.1.37. Influence of friction coefficient on tangential wheel-rail contact forces (two contact points) in diverging route. S1002 wheel profile, vehicle speed 70 km/h, rail profile 60E1i30 cut 60. Leading wheel in leading bogie, facing move

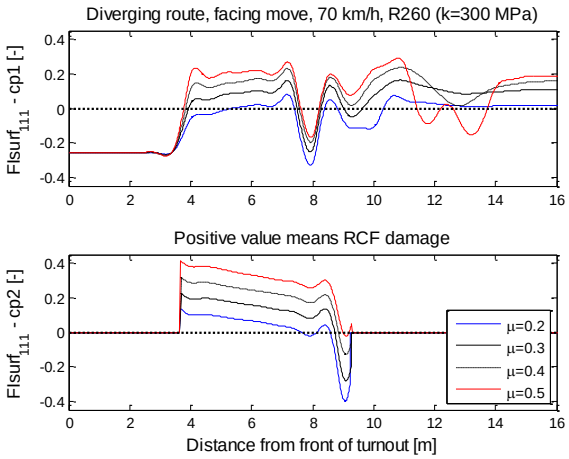

Figure 3.1.38. Influence of friction coefficient on FIsurf (two contact points) in diverging route. S1002 wheel profile, vehicle speed 70 km/h, rail profile 60E1i30 cut 60. Leading wheel in leading bogie, facing move

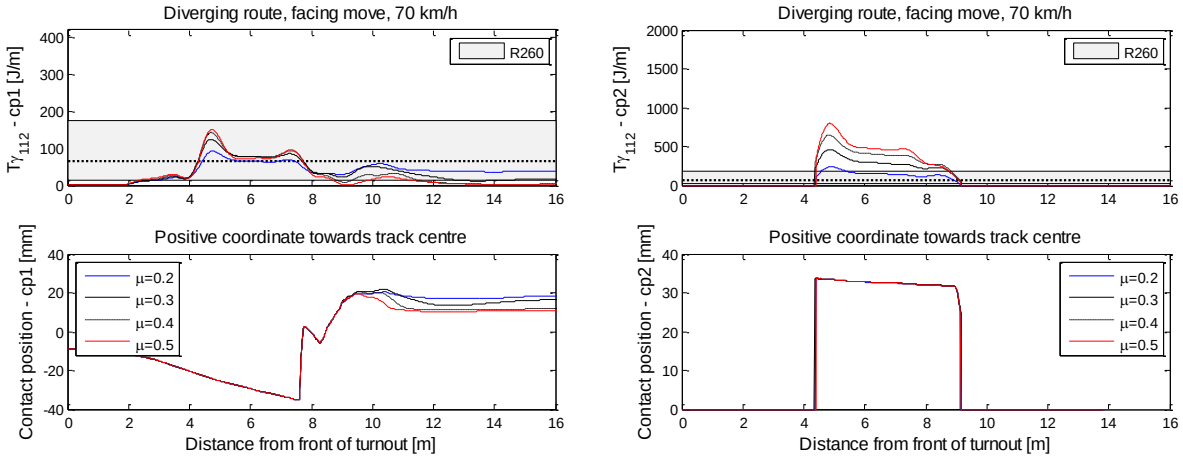

(a) (b)

Figure 3.1.39. Influence of friction coefficient on damage function Tγ and contact position (two contact points) in diverging route. S1002 wheel profile, vehicle speed 70 km/h, rail profile 60E1i30 cut 60. Trailing wheel in leading bogie, facing move

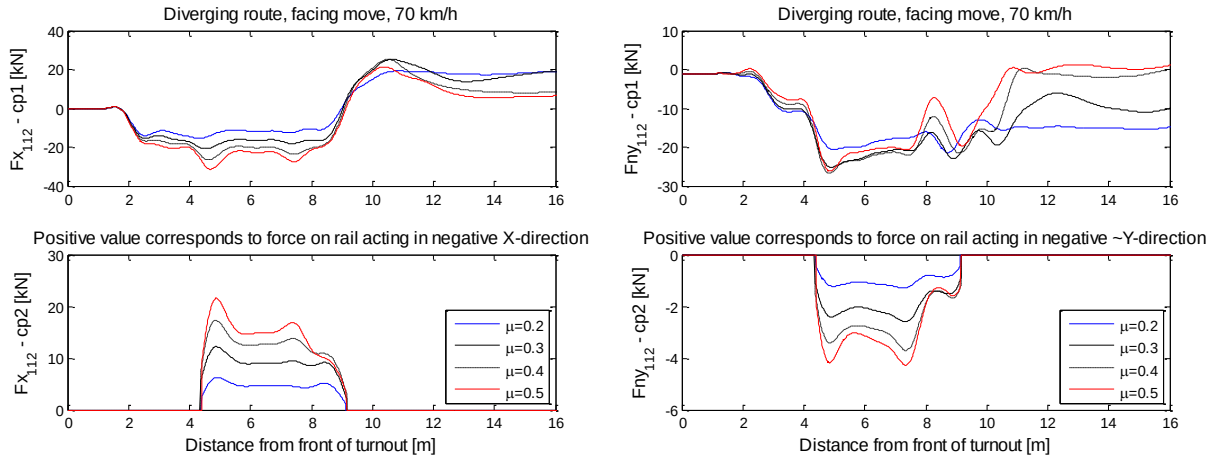

(a) (b)

Figure 3.1.40. Influence of friction coefficient on tangential wheel-rail contact forces (two contact points) in diverging route. S1002 wheel profile, vehicle speed 70 km/h, rail profile 60E1i30 cut 60. Trailing wheel in leading bogie, facing move

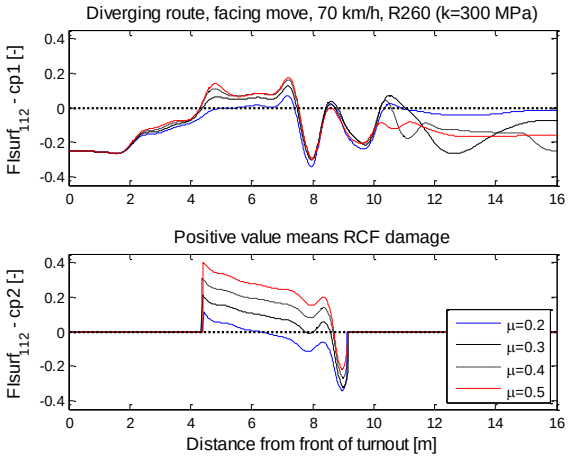

Figure 3.1.41. Influence of friction coefficient on FI_{surf} (two contact points) in diverging route. S1002 wheel profile, vehicle speed 70 km/h, rail profile 60E1i30 cut 60. Trailing wheel in leading bogie, facing move

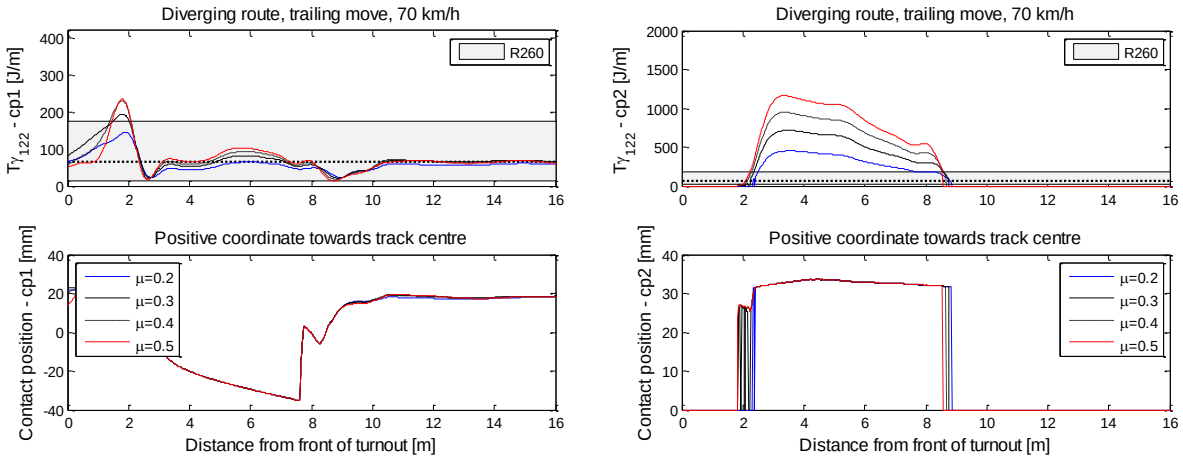

(a) (b)

Figure 3.1.42. Influence of friction coefficient on damage function Tγ and contact position (two contact points) in diverging route. S1002 wheel profile, vehicle speed 70 km/h, rail profile 60E1i30 cut 60. Leading wheel in leading bogie, trailing move

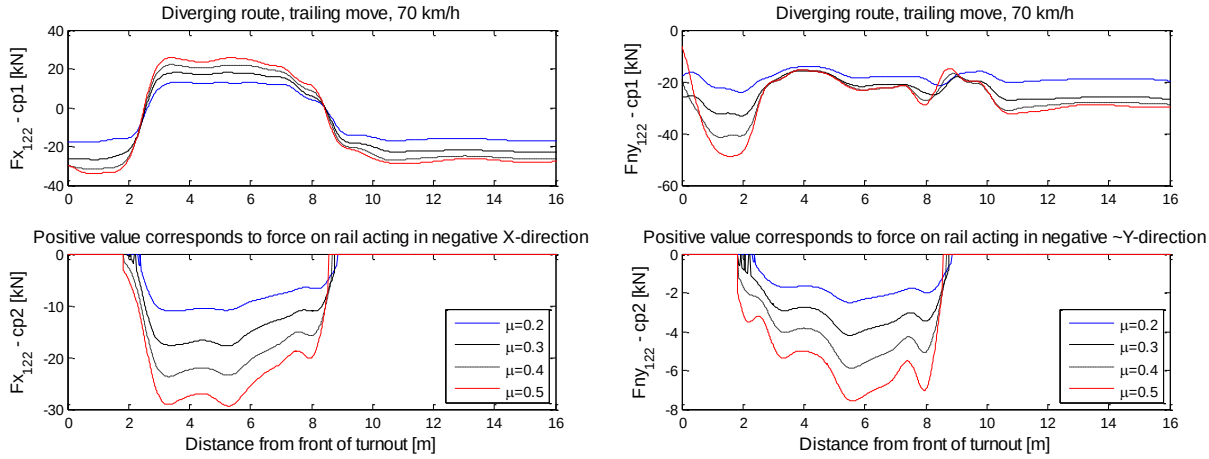

(a) (b)

Figure 3.1.43. Influence of friction coefficient on tangential wheel-rail contact forces (two contact points) in diverging route. S1002 wheel profile, vehicle speed 70 km/h, rail profile 60E1i30 cut 60. Leading wheel in leading bogie, trailing move

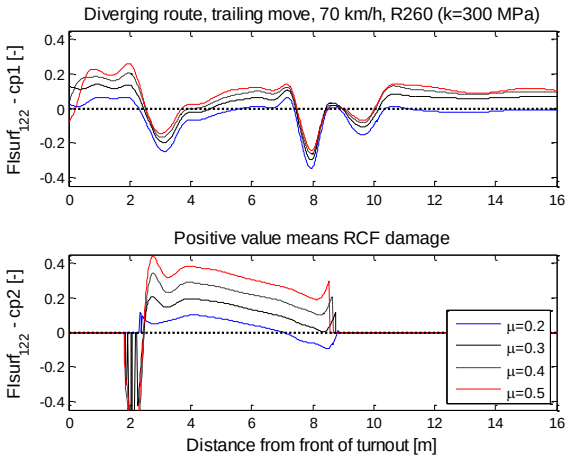

Figure 3.1.44. Influence of friction coefficient on FI_{surf} (two contact points) in diverging route. S1002 wheel profile, vehicle speed 70 km/h, rail profile 60E1i30 cut 60. Leading wheel in leading bogie, trailing move

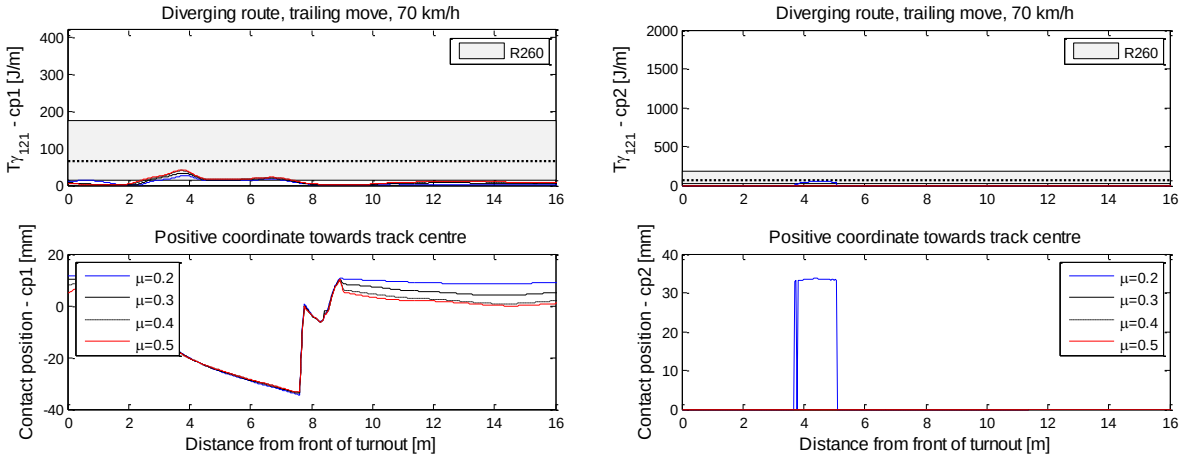

(a) (b)

Figure 3.1.45. Influence of friction coefficient on damage function Tγ and contact position (two contact points) in diverging route. S1002 wheel profile, vehicle speed 70 km/h, rail profile 60E1i30 cut 60. Trailing wheel in leading bogie, trailing move

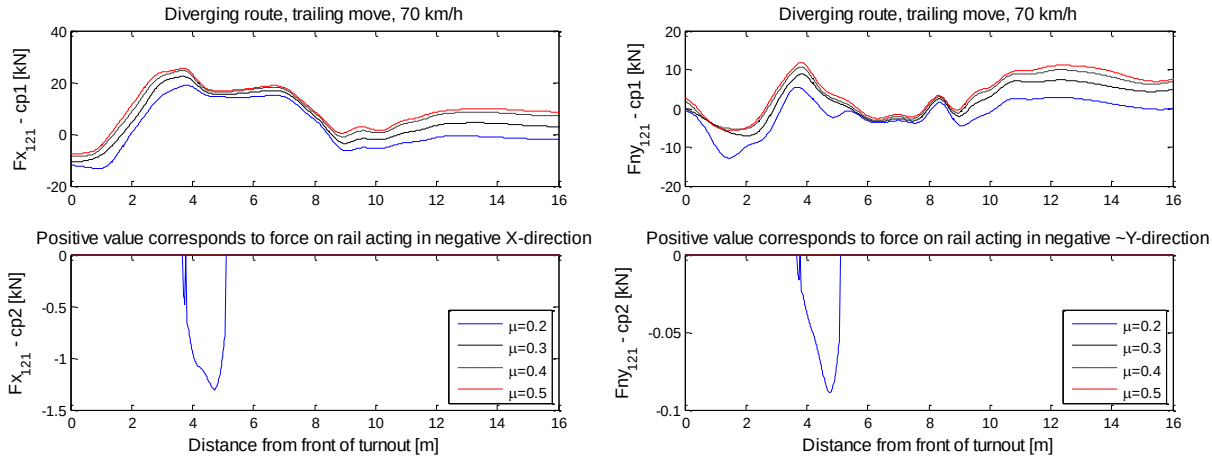

(a) (b)

Figure 3.1.46. Influence of friction coefficient on tangential wheel-rail contact forces (two contact points) in diverging route (direction of forces as explained in the figure). S1002 wheel profile, vehicle speed 70 km/h, rail profile 60E1i30 cut 60. Trailing wheel in leading bogie, trailing move

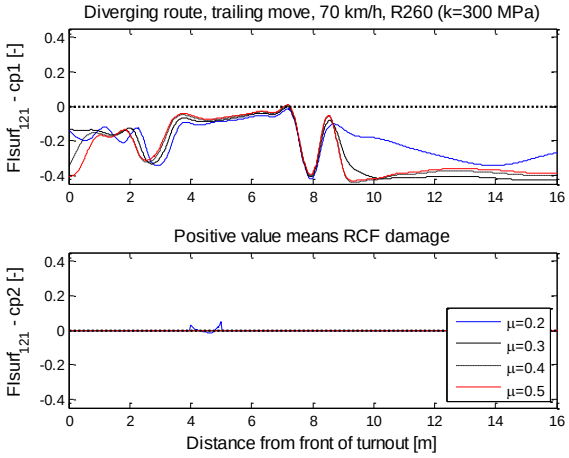

Figure 3.1.47. Influence of friction coefficient on FIsurf (two contact points) in diverging route. S1002 wheel profile, vehicle speed 70 km/h, rail profile 60E1i30 cut 60. Trailing wheel in leading bogie, trailing move

Table 3.1.3. Influence of friction coefficient on maximum accumulated wear and RCF damage for one Y25 vehicle (four wheelsets) in diverging route. S1002 wheel profile, vehicle speed 70 km/h, rail profile 60E1i30 cut 60. Damage is normalised with respect to damage calculated for the case marked with grey colour

Rail profile	Move	Max wear [μm]	Position [m]	Max RCF damage [10^{-6}]	Position [m]	Max wear [μm]	Position [m]	Max RCF damage [10^{-6}]	Position [m]
		R260				R350HT			
μ=0.2	Facing	0.77	x=4.45 m y=3.37 cm	0.52	x=4.39 m y=3.37 cm	0.12	x=4.45 m y=3.37 cm	0.43	x=3.66 m y=3.31 cm
μ=0.3	Facing	1	x=5.12 m y=3.33 cm	1	x=5.64 m y=3.27 cm	0.15	x=4.45 m y=3.37 cm	2.68	x=4.35 m y=3.37 cm
μ=0.4	Facing	1.15	x=5.06 m y=3.33 cm	1.44	x=10.97 m y=2.45 cm	0.16	x=4.45 m y=3.37 cm	13.17	x=10.80 m y=2.49 cm
μ=0.5	Facing	1.18	x=5.02 m y=3.35 cm	12.61	x=10.21 m y=2.59 cm	0.16	x=4.49 m y=3.37 cm	33.61	x=10.48 m y=2.57 cm
μ=0.2	Trailing	0.99	x=4.06 m y=3.35 cm	0.40	x=2.32 m y=3.15 cm	0.12	x=4.06 m y=3.35 cm	0.21	x=2.32 m y=3.15 cm
μ=0.3	Trailing	1.10	x=4.06 m y=3.35 cm	1.34	x=8.66 m y=3.17 cm	0.16	x=4.06 m y=3.35 cm	1.31	x=1.01 m y=2.47 cm
μ=0.4	Trailing	1.10	x=4.06 m y=3.35 cm	7.29	x=2.39 m y=1.89 cm	0.16	x=4.06 m y=3.35 cm	7.00	x=1.01 m y=2.53 cm
μ=0.5	Trailing	1.07	x=4.06 m y=3.35 cm	16.81	x=2.35 m y=2.01 cm	0.16	x=4.06 m y=3.35 cm	28.01	x=1.07 m y=2.51 cm

Table 3.1.4. Influence of friction coefficient on maximum accumulated wear and RCF damage for 10 Y25 vehicles (40 wheelsets) in diverging route. 10 combinations of worn wheel profile and vehicle speed 70 km/h, rail profile 60E1i30 cut 60. Damage is normalised with respect to damage calculated for the case marked with grey colour

Rail profile	Move	Max wear [μm]	Position [m]	Max RCF damage [10^{-6}]	Position [m]	Max wear [μm]	Position [m]	Max RCF damage [10^{-6}]	Position [m]
		R260				R350HT			
μ=0.2	Facing	0.69	x=4.08 m y=3.39 cm	0.11	x=9.02 m y=1.99 cm	0.06	x=3.95 m y=3.41 cm	0.19	x=10.58 m y=2.39 cm
μ=0.3	Facing	1	x=4.14 m y=3.39 cm	1	x=9.23 m y=2.15 cm	0.08	x=3.97 m y=3.41 cm	2.88	x=10.47 m y=2.43 cm
μ=0.4	Facing	1.19	x=4.24 m y=3.39 cm	2.85	x=10.08 m y=2.43 cm	0.09	x=3.97 m y=3.41 cm	15.42	x=10.47 m y=2.47 cm
μ=0.5	Facing	1.31	x=4.38 m y=3.39 cm	6.74	x=9.06 m y=2.85 cm	0.11	x=3.97 m y=3.41 cm	24.61	x=9.17 m y=2.59 cm
μ=0.2	Trailing	2.14	x=3.69 m y=3.43 cm	0.15	x=2.37 m y=1.95 cm	0.14	x=3.36 m y=3.43 cm	0.36	x=1.75 m y=2.25 cm
μ=0.3	Trailing	2.70	x=3.93 m y=3.41 cm	2.97	x=2.33 m y=1.99 cm	0.19	x=3.36 m y=3.43 cm	4.06	x=2.00 m y=2.21 cm
μ=0.4	Trailing	2.78	x=3.93 m y=3.41 cm	14.59	x=2.19 m y=2.09 cm	0.19	x=3.42 m y=3.45 cm	18.99	x=2.00 m y=2.23 cm
μ=0.5	Trailing	2.74	x=3.67 m y=3.43 cm	23.54	x=2.10 m y=2.15 cm	0.18	x=3.42 m y=3.45 cm	44.19	x=1.98 m y=2.29 cm

3.1.8 REFERENCES

[3.1.1] B.A. Pålsson, Optimisation of railway switches and crossings, PhD thesis, Department of Applied Mechanics, Chalmers University of Technology, Gothenburg, Sweden, 2014

[3.1.2] C4R Deliverable 13.1, Operational failure modes of S&C, September 2014, 51 pp

[3.1.3] B.A. Pålsson and J.C.O. Nielsen, Track gauge optimisation of railway switches using a genetic algorithm, *Vehicle System Dynamics*, 2012, **50**(S1), pp 365-387

[3.1.4] B.A. Pålsson, Design optimisation of switch rails in railway turnouts, *Vehicle System Dynamics*, 2013, **51**(10), pp 1619-1639

[3.1.5] J.C.O. Nielsen, B.A. Pålsson and P.T. Torstensson, Switch panel design based on simulation of accumulated rail damage in a railway turnout, *Proceedings 10th International Conference on Contact Mechanics and Wear of Rail/Wheel Systems*, Colorado Springs, CO, USA, September 2015

[3.1.6] J.F. Archard and W. Hirst, The wear of metals under unlubricated conditions, *Proceedings*

of the Royal Society of London. Series A. Mathematical and Physical Sciences, 1956, **236**, pp 397-410

[3.1.7] U. Olofsson and T. Telliskivi, Wear, plastic deformation and friction of two rail steels – a full-scale test and a laboratory study, *Wear*, 2003, pp 80-93

[3.1.8] R. Enblom and M. Berg, Proposed procedure and trial simulation of rail profile evolution due to uniform wear, *Proceedings IMechE, Part F, Journal of Rail and Rapid Transit*, 2008, **222**, pp 15-25

[3.1.9] A. Ekberg, E. Kabo and H. Andersson, An engineering model for prediction of rolling contact fatigue of railway wheels, *Fatigue Fract Engng Mater Struct*, 2002, **25**, pp 899-909

[3.1.10] A. Ekberg, B. Åkesson and E. Kabo, Wheel/rail rolling contact fatigue – Probe, predict, prevent, *Wear*, 2014, **314**(1), pp 2-12

[3.1.11] B. Dirks and R. Enblom, Prediction model for wheel profile wear and rolling contact fatigue, *Wear*, 2011, **271**, pp 210-217

[3.1.12] B. Dirks, R. Enblom, A Ekberg and M. Berg, The development of a crack propagation model for railway wheels and rails, *Fatigue and Fracture of Engineering Materials and Structures*, 2015, **38**(12), pp 1478-1491

[3.1.13] M.C. Burstow, Whole life rail model application and development for RSSB – continued development of an RCF damage parameter, Rail Standards and Safety Board, London, 2004

[3.1.14] J.R. Evans, T.K.Y. Lee, and C.C. Hon, Optimising the wheel/rail interface on a modern urban rail system, *Vehicle System Dynamics*, 2008, **46**, pp 119-127

[3.1.15] B. Dirks, Simulation and measurement of wheel on rail fatigue and wear, PhD thesis, Department of Aeronautical and Vehicle Engineering, Royal Institute of Technology, Stockholm, Sweden, 2015

[3.1.16] INNOTRACK D4.1.5, Definitive guidelines on the use of different rail grades, 2009 (downloaded from www.innotrack.net/Reports in November 2015)

[3.1.17] TATA Steel Rail technical guide, 2014 (downloaded from www.tatasteeleurope.com/static_files/Downloads/Rail/Rail%20technical%20guide%20Eng.pdf in March 2016)

[3.1.18] K. Mädler, A. Zoll, R. Heyder and M. Brehmer, Rail materials – alternatives and limits, *Proc 8th World Congress on Railway Research (WCRR2008)*, Seoul, Korea, 2008

[3.1.19] R. Heyder and K. Mädler, The influence of wheel and rail material on the wear of the respective contact partner, *Proceedings 10th International Conference on Contact Mechanics and Wear of Rail/Wheel Systems*, Colorado Springs, CO, USA, September 2015

[3.1.20] R. Heyder and M. Brehmer, Empirical studies of head check propagation on the DB network, *Wear* 314, 36-43, 2014

[3.1.21] R. Heyder and M. Brehmer, Empirische Erkenntnisse zum HeadCheck-Wachstum und zur Verschleissentwicklung, ZEVrail 137, 4 April, 2013

[3.1.22] R. Heyder and T. Hempe, Extending rail life on DB's core network, *Railway Gazette International*, April 2010

[3.1.23] R. Heyder and G. Girsch, Testing of HSH rails in high-speed tracks to minimize rail damage, *Wear* 258, 1014-1021, 2005

[3.1.24] INNOTRACK D4.1.4, Rail degradation mechanisms, 2009 (downloaded from www.innotrack.net/Reports in November 2015)

[3.1.25] H. Ossberger, VAE GmbH, personal communication, 2015-11-18

[3.1.26] S.C. Lim and M.F. Ashby, Wear-mechanism maps, *Acta Metallurgica* 35(1), 1-24, 1987

[3.1.27] R. Lewis and U. Olofsson, Mapping rail wear regimes and transitions, *Wear* 257, 721-729, 2004

[3.1.28] U. Olofsson and T. Telliskivi, Wear, plastic deformation and friction of two rail steels – a full-scale test and a laboratory study, *Wear* 254, 80-93, 2003

[3.1.29] T. Jendel, Prediction of wheel profile wear – comparisons with field measurements, *Wear* 253, 89-99, 2002

[3.1.30] G. Vasic, Modelling of wear and crack initiation in rails, PhD thesis, The University of Newcastle, 2013

[3.1.31] E.J. Pavlina and C.J. van Tyne, Correlation of yield strength and tensile strength with hardness for steels, *Journal of Materials Engineering and Performance* 17(6), 888-893, 2008

[3.1.32] J. Ahlström and B. Karlsson, Fatigue behavior of rail steel – a comparison between strain and stress controlled loading, *Wear* 258, 1187-1193, 2005

[3.1.33] M. Schilke and J. Ahlström, Laboratory tests of material properties, In INNOTRACK deliverable 3.1.6, Recommendation of, and scientific basis for, optimization of switches & crossings – part 2, www.innotrack.net/Reports

[3.1.34] GENSYS [Internet]. Available from www.gensys.se

[3.1.35] T. Jendel, Dynamic analysis of a freight wagon with modified Y25 bogies, M.Sc. thesis, Department of Vehicle Engineering, Royal Institute of Technology, Stockholm, Sweden, 1997

[3.1.36] E. Kassa, C. Andersson, and J.C.O. Nielsen, Simulation of dynamic interaction between train and railway turnout, *Vehicle System Dynamics*, 2006, **44**(3), pp 247-258

[3.1.37] B.A. Pålsson, and J.C.O. Nielsen, Dynamic vehicle–track interaction in switches and crossings and the influence of rail pad stiffness – field measurements and validation of a simulation model, *Vehicle System Dynamics*, 2015, **53**(6), pp 734-755

[3.1.38] E. Berggren, Railway track stiffness – dynamic measurements and evaluation for efficient maintenance, Ph.D. thesis, Aeronautical and Vehicle Enginering, Royal Institute of Technology, Stockholm, Sweden, 2009

[3.1.39] J.J. Kalker, A fast algorithm for the simplified theory of rolling contact, *Vehicle System Dynamics*, 1982, **11**(1), pp 1-13

[3.1.40] B.A. Pålsson, and J.C.O. Nielsen, Wheel–rail interaction and damage in switches and crossings, *Vehicle System Dynamics*, 2012, **50**(1), pp 43-58

3.2 MEDIUM-TERM DESIGN SOLUTIONS

While Section 3.1 focuses on short-term solutions in switch panels, this section focuses on medium-term solutions in crossing panels. Crossing panels also suffer from discontinuity in both support and kinematic guidance of the vehicle's axles, leading to a large range of damage from rail materials, cast crossings structural fatigue, ballast support deterioration (voids) and fatigue of components (pads and bearers) – see the failure catalogue report [3.2.1]. Section 3.2 has been written by the University of Huddersfield, except Section 3.2.7 which has been written by VCSA.

3.2.1 SOURCE OF DAMAGE IN CROSSING PANELS

Similarly to the switch panel, the wheelset traversing a crossing experiences rapid changes in contact conditions. The point of contact on the wheel running on the crossing is moving outwards (towards field side) as the wheel passes the throat of the crossing and the wing rail diverges at the crossing angle. The wheel therefore rolls onto a decreasing rolling radius and its centre of gravity moves down, until a second point of contact appears between the root of the wheel flange and the crossing nose; this is what is called the load transfer (from wing to nose and vice versa in facing and trailing move respectively). This sudden upward motion of the wheel on the nose topping resembles an inverted triangle (Figure 3.2.) and can be characterised by the dip angle value [3.2.2] which is known to be directly related to the magnitude of the vertical dynamic impact force induced by this load transfer (see analogy with dip joints [3.2.3]), as evidenced by simulation output in Figure 3.2.3. The same behaviour occurs in the reverse direction of movement. The dynamic impact force contains a very high frequency peak value (P1) and a medium frequency oscillatory response (P2) as illustrated in Figure 3.2.2. The P1 force corresponds to the wheel mass moving against the rail mass and mainly corresponds to energy deformation in the contact zone. It is generally ignored within standard practice when dealing with track damage, however due to the high magnitude of stress generated it may arguably be a key driver for damage within the rail material. The P2 force is associated with the movement of the wheel mass coupled with the rail against the sleeper and its support. It is therefore leading to damage of the support in crossing panels, especially linked to ballast deterioration. Table 3.2.1 shows calculation of typical semi-wavelength for the P1 and P2 forces, showing that the P1 is concentrated over a few tens of millimetres of rail while the P2 force covers a longer span ranging from ca. 50 to 450 mm.

In addition to the vertical dynamic impact load, the rolling radius difference generated between left and right wheels induces a rapid change of angle of attack around the load transfer area (LTA) (similar to that explained in the switch panel in Section 3.1) which leads to sudden lateral dynamic forces also impacting on rail damage as well as support and lateral geometry degradations. The magnitude of the wheel force, although lower than vertical impact, can be in the order of 20 to 30 kN typically. A typical output from simulation results is presented in Figure 3.2.7 (bottom).

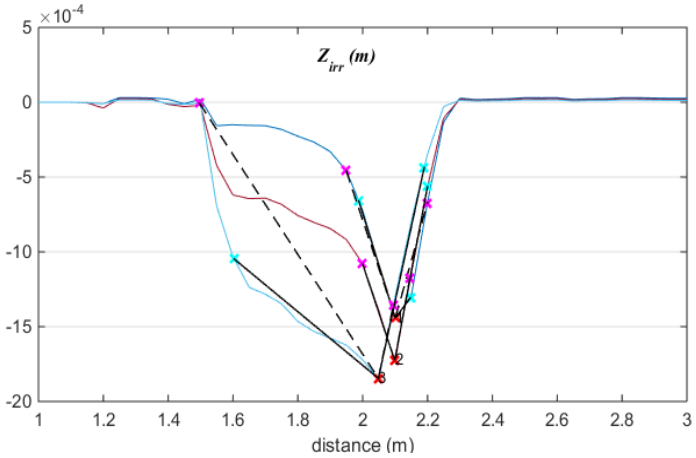

Figure 3.2.1. Unsprung mass vertical motion (meters) and points for corresponding equivalent dip angle calculation, for one wheel negotiating one crossing geometry at three different lateral positions [3.2.2]

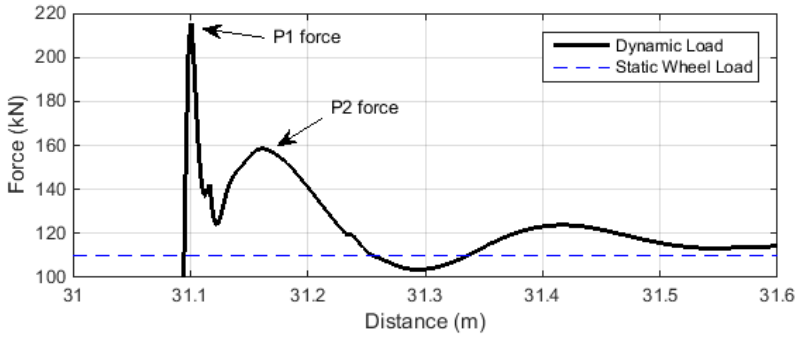

Figure 3.2.2. Typical P1 and P2 calculated force response against distance

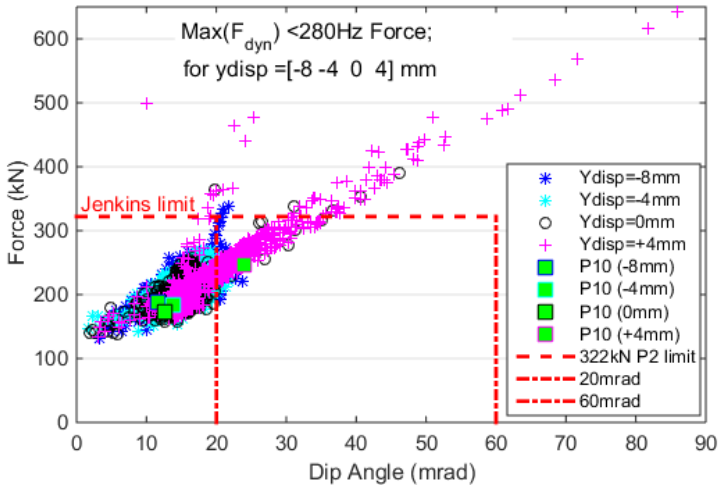

Figure 3.2.3. Relation between equivalent dip angle and P2 force level simulated for a range of wheel profiles [3.2.2]

Table 3.2.1. Typical semi-wavelength for P1 and P2 impact forces

		P1 frequency		P2 frequency	
		low	high	low	high
	Hz	600	800	80	140
	semi-period (*ms*)	0.8	0.6	6.3	3.6
km/h	*m/s*	Length of semi-walength in mm			
40	11.11	9	7	69	40
80	22.22	19	14	139	79
120	33.33	28	21	208	119
180	50.00	42	31	313	179
250	69.44	58	43	434	248

Vehicle speed

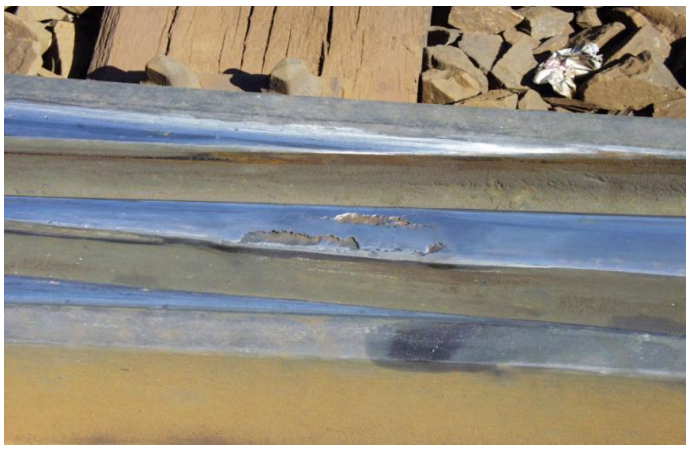

Figure 3.2.4. Example damage on crossing nose – spalling

Figure 3.2.5. Example damage of wing rail – plastic deformation and localised crushing in contact area

Examples of damage at crossing nose related to the P1 force are shown in Figure 3.2.4 and Figure 3.2.5 taken from [3.2.1]. The very local nature of the discrete damage can be observed in the narrow location of the load transfer area (LTA), on the crossing nose and on the wing rail. Examples of damage of support linked to the P2 force are shown in Figure 3.2.6, where damage location can be extended away from the load transfer area due to the longer wavelength of the P2 force.

Figure 3.2.6. Illustration of vertical support damage due to the P2 vertical force: voided sleeper (left) and fatigued cast crossing (right) occurring some distance away from the LTA

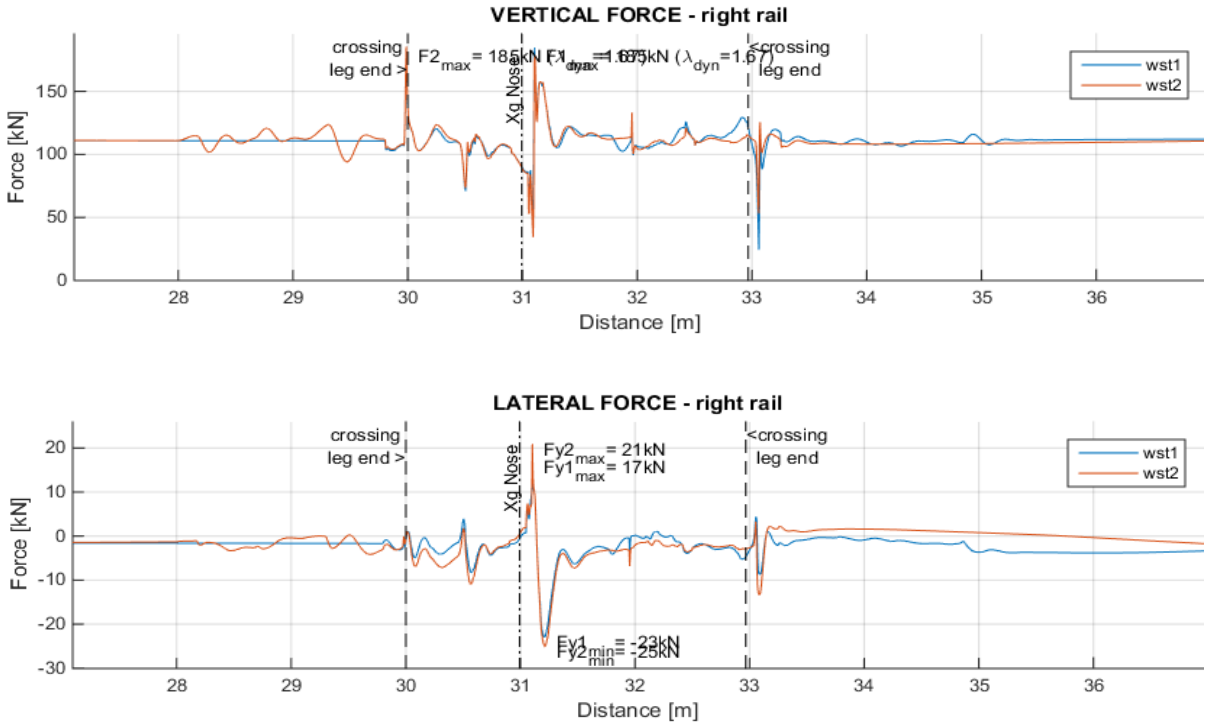

Figure 3.2.7. Typical vertical (top) and lateral (bottom) forces by the wheel on a crossing from leading and trailing axles

3.2.2 PARAMETERS OF INFLUENCE

A range of parameters influencing the magnitude and location of the damaging dynamic forces are discussed below:

- Axle Payload: The vehicle axle load is one of the main drivers for vertical damage. The heavier the axle load (heavy freight and locomotives), the higher the wheel-rail contact stresses and therefore the higher the potential damage in rail materials.
- Vehicle type (*PYS*): running gears properties like primary yaw stiffness (*PYS*) influence steering ability and creep forces in LTA, as well as wheelset attitude in diverging route - angle of attack and lateral shifted position – both of which are key parameters in predicting dynamic forces, contact conditions and resulting damage (see Figure 3.2.3 for the effect of axle lateral displacement on force level). In curves, the leading axle in a bogie will typically tend to move towards the high rail with a higher angle of attack, while the trailing axle can move in opposite direction or be closer to the track centreline. Friction based freight bogies running gears are particularly prone to generate poor steering conditions in turnouts. Therefore both axles in a bogie need to be considered in terms of cumulative damage in S&C.
- Vehicle type ($M_{unsprung}$): P1 and P2 forces are directly proportional to the wheelset unsprung mass ($M_{unsprung}$) – heavy running gears such as motor bogies with partly unsuspended gear box and traction motors and brake discs lead to higher impact loads.
- Vehicle speed (*V*): The faster the speed of the vehicle (*V*) the more the energy spent in making the unsprung mass change direction in the LTA, therefore the higher the damage. However in practice this is dealt with having different S&C categories for specific ranges of speed (C, D, E, etc… types) and higher speed category have shallower crossing angles or even movable crossing for dedicated high speed making damage more controllable. The work in this project is concentrated on improving medium speed category and mixed traffic (C to E types).
- Vehicle wheel shapes: In combination with PYS and V, the wheel shapes are a key driver for the axle behaviour in the crossing panel and the resulting dynamic forces and wheel-rail contact conditions. In [3.2.2] it was demonstrated that the wheel shape can have a strong influence on the vertical wheel motion and therefore on the magnitude of the P1 and P2 forces. Figure 3.2.3 shows the scatter in force level as a function of wheel shape. It was also demonstrated that some characteristics of the wheel for example as the equivalent slope at the nominal radius increases with wear this tend to lead to higher dynamic load factor. Hollow worn shapes also lead to very different dynamic behaviour and damage, and therefore a representative range of wheels need to be considered in the design and optimisation of a crossing.
- Rail material: The type of crossing and associated material governs the behaviour under high load conditions. Two main categories are in use. On the one hand fabricated or built up crossing generally use standard grade R260 steel but can also easily accommodate better

resisting steels (see Section 3.2.7 on material consideration). On the other hand, cast manganese (Mn) block, which are more expensive, are primarily used because they offer work hardening under initial loading to increase the material hardness and the resistance to wear and plastic deformation. Additionally the one piece casting ensures good bending strength and resistance in track. There can also be Explosive Depth Hardened (EDH) cast manganese crossings so that high resistance is achieved form the start thus limiting the initial deformation in traffic. Within Section 3.2.7.1, a new bainitic steel material is proposed for improved performance of crossing nose.

- Wheel-rail interface properties: the materials, surface roughness, weather conditions and any other types of lubrication influence the coefficient of friction between wheel and rail and therefore influence dynamic behaviour and damage in the contact. Artificial lubrication is not a subject of study but a realistic range of friction values needs to be taken into account in the optimisation process.

- Crossing geometry: The shape of the crossing geometry and in particular the cross-sections at specific locations along its length, are key to the wheel-rail contact dynamic behaviour. Key areas of optimisation concern the nose shape and its toping angle – how fast it rises, as well as the wing rail slope and its height with respect to the nose. A number of research has been looking at the crossing nose optimisation [3.2.4 to 3.2.6] and so far little work has been done on the understanding of existing wing rail shapes and how to optimise performance by modifications to the wing rail. This is a key area of research identified in this project.

- Track geometry: Poor and degraded vertical track geometry (horizontal irregularities) attributed to the poorly supported sleepers (ballast degradation) and uneven stiffness along the crossing panels lead to increased dynamic effects in and around the LTA. These conditions obviously result in a feedback loop mechanism where dynamics vertical forces and vertical degradation are amplified and accelerated.

- Crossing types: Two main types of crossing can be found which are acute or common crossing and obtuse. The first one is far more common as the name indicates. Obtuse although much less prominent in numbers are reported to have higher rate of damage and failures. The key difference is that on an obtuse crossing the wing rail is placed on one side and acts as load support for the wheel in both directions. This means that at the crossing point, the wing rail shape is compromised and cannot be optimised for a single direction independently from the other. This report focuses on common crossing as obtuse is a particular case to be dealt with separately, however modelling techniques presented in this report can also be employed for obtuse crossings in the future.

- Crossing angle (*1:N*): This parameter has an obvious influence on the dynamic forces and damage observed as a wider angle (lower *N* value) leads to a shorter LTA with potential less support for the wheel tread as the wing rail diverges more rapidly. Turnout categories C to E switch lengths for NR56 and NR60 designs in the UK include natural angles from $9^{1/4}$ to 15 and from 9.5 to $15^{3/4}$ respectively. This range is of interest in the project as they are common

types on intercity lines with mixed traffic. CV type switches tend to represent a large population in track and $9^{1/4}$ crossings can see significant speeds in the through routes, therefore leading to higher dynamics effects.

- Track support: Track support stiffness is a key driver for the P2 impact force. The overall resilient stiffness of the crossing panel governs the load spreading capabilities along the panel and therefore the peak load in the LTA. The quality of the ballast support underneath sleepers, mass/bending properties of the long bearers, their connection with the rest of the panel, the rail pads stiffness used between the cast crossing and the sleepers, the bending properties of the cast crossing and mass; all are governing parameters in terms of track stiffness reaction and damage level. In this project the influence of rail pad resilience stiffness as well as use of USP is discussed in terms of previous results [3.2.2] and additional study. The move away from conventional ballasted track towards more consistently supported track is also discussed with a preliminary study on linking sleepers together to effectively make the crossing panel closer to a slab in terms of its dynamic behaviour (Section 3.2.6).
- Check rail lateral position (tolerances and maintenance): maintaining correct check rail gauge position ensures that the wheels do not move too close to the crossing nose. The fact that flange contact increases the chances for high damage has been demonstrated in SUSTRAIL output [3.2.2].

The key challenges in terms of medium-term optimisation have been identified as:

- Geometry optimisation of the crossing to minimise vertical dynamics impact loads and lower steering force damage in the contact areas. This involves parametric variation analysis related to wing rail angle, height and transversal length, wing topping gradient along the crossing length.
- Dynamic load mitigation (ballast protection) through rail pad stiffness optimisation and use of USP.
- Dynamic load mitigation (ballast protection) through use of connecting elements between sleepers.
- Validation of simulation processes, including prediction of plastically deformed crossing shapes.
- Novel material in crossing nose and wing rails to resist fatigue, wear and plastic deformation.

3.2.3 BRIEF REVIEW ON DAMAGE PREDICTION AND OPTIMISATION OF CROSSINGS

The following provide a brief overview of recent research output on the use of numerical modelling for predicting crossing damage according to the topics:

3.2.3.1 State of the art: vehicle-track modelling at crossings

In the SustRail project [3.2.2], an extensive technology review about the mathematical modelling of train/turnout interaction have been carried out, referring to models that use both a multi-body approach (e.g. [3.2.7-3.2.9]) or a finite element (FE) approach ([3.2.10, 3.2.11]).

In [3.2.12] a practical methodology to determine the location and the entity of two contact patches in a turnout is presented and applied to optimise the top height of the nose. The results show a drastic reduction of the main parameters considered, including contact forces and wheelset, rail and sleeper vertical accelerations.

A new computer program called WEAR, which is an extension of the CONTACT algorithm of Kalker, is described in [3.2.13]. It takes into account conformal contact situations by using influence numbers for a quasi-quarter space and by using the local and varying spin creepage in each element in the contact patch.

Similarly, [3.2.14] presents a semi-Hertzian method to solve the wheel/rail contact problem in case of high-speed switches with moveable frog. This consists on dividing the rail in narrow strips and associating a stiffness, which depends on the local curvatures and elastic properties of the material, to each of them. It has been then implemented in the VOCOLIN multi-body research software to estimate contact forces and contact stresses at the crossing panel.

3.2.3.2 State of the art: FE models of wheel-crossing simulation

A comparison between four methods (i.e. Hertzian contact theory, non-Hertzian contact theory implemented in CONTACT, elastic FE contact model and elastic-plastic FE contact model) based on calculated contact pressure, contact patch size and penetration depth is established in [3.2.15]. The results show similar level of magnitude in case of first three approaches. However, significant discrepancies appear when the elastic-plastic theory is considered, with differences in the maximum contact pressure up to 42%.

In [3.2.16], a dynamic FE model of wheel/rail interaction at the crossing panel is presented to calculate impact forces as well as stress levels and accumulated equivalent plastic strain. It has been demonstrated how high stresses are reached in the crossing nose even in cases of moderate contact forces. Using the FE approach, it is also possible to predict where the plastic deformation may occur taking into account the material properties.

3.2.3.3 Predicting wheel-rail contact degradation (capabilities and limitations)

As part of the WP 3.1 in Capacity4Rail project [3.2.1], a catalogue of the most common failure modes occurring at turnouts, including a detailed description, possible causes and corrective/preventive measures, has been compiled. Regarding the plastic deformation, a detailed investigation is carried out in [3.2.17], where the evolution of the cross-section at the crossing nose has been assessed with a quasi-static model taking into account two different materials types (i.e. “soft” and “hard” material). Similarly, [3.2.18] shows how the dynamic outputs of vehicle/turnout interaction are used in the FE analysis to calculate the evolution of the profile and the stress field at a given position of the switch/stock rail assembly.

Instead of calculating the actual evolution of the profile, which can be very costly and sometimes not necessary for the scope of the work, a good indication of plastic deformation is given by the accumulated equivalent plastic strain (PEEQ), calculated through a FE analysis (e.g. [3.2.19]). That quantity can be used to compare different design solutions.

An example of numerical modelling of wear prediction using the commercial software Vampire at the crossing panel is shown in [3.2.20]. The optimum travelling speed for the given vehicle and track conditions is found to minimise wear.

Usually, wear and plastic deformation are damage mechanisms that contribute simultaneously to the geometry evolution. Therefore it is necessary to sum the effects to correctly model the degradation process. For example, in [3.2.21] a methodology for the simulation of time evolution of rail profiles in turnouts is presented taking into account non-linear material properties and plasticity effects. It can be used in a design stage to reduce costs and increase the life of track components.

3.2.3.4 Predicting sub-surface stresses (capabilities and limitations)

The distributions of contact stress fields and residual stress fields can be calculated using elastic-plastic FE method, as presented in [3.2.22]. It has been demonstrated how the combined effect of the stresses considered plays important roles in fatigue crack initiation in the nose rail. Also, the speed influences the region of residual stresses.

Another approach consists on calculating an index, as proposed in [3.2.23], which gives an indication of sub-surface stress level. It is necessary to underline that this study has not been developed specifically for application in turnouts, but it is still possible to use it for a qualitative/quantitative comparison.

3.2.3.5 Predicting component damage and structural fatigue

Cracked sleepers in a turnout represent a considerable risk for derailment. The main aim of study presented in [3.2.24] is to examine current designs to aid failure analysis.

Other studies focus on the requirements of material in terms of resistance to wear and crack development. For example, an investigation on five different steel grades used to create frogs have been conducted in [3.2.25], covering a various steel microstructures and macroscopic hardness values. The results can be used as input data for FE analyses in the design stage.

3.2.3.6 Support degradation and ballast deterioration

It is possible to analyse the support degradation undertaking a statistical approach, when measured data are available, or a numerical modelling approach.

An example of key study using the first approach is presented in [3.2.26]. It has been demonstrated that each turnout needs to be treated individually. Also, there is a limit for the crossing position settlement: before reaching that limit, the higher degradation rate occurs at the crossing point, while it propagates in the vicinity afterwards.

Several papers (e.g. [3.2.27]) adopt an iterative procedure to numerically calculate the track settlement in a turnout. The results obtained can used both in a design and maintenance phase.

Finally, a practical application of ballast reinforcement to reduce track settlement at the crossing is established in [3.2.28]. It has been demonstrated how it helps greatly to save up to 30 maintenance cycles, as the site has never required any operation for 10 years.

	Ref	Year	Model	Practical application	Notes
State of the art vehicle-track modelling at crossings	[3.2.12]	2010	X		• Methodology for two contact point • Optimisation of the top height of the nose
	[3.2.13]	2014	X		• Methodology for conformal contact
	[3.2.14]	2006	X		• Methodology using semi-Hertzian contact • Application to high-speed crossings
State of the art FE models of wheel-crossing simulations	[3.2.15]	2008	X		• Comparison between four contact solving methodologies • Remarkable differences in the elastic-plastic theory
	[3.2.16]	2012	X		• Methodology to calculate impact forces and contact stresses • Prediction where plastic deformation may occur
Predicting wheel-rail contact conditions	[3.2.1]	2014		X	• Catalogue of the most common failure modes at the S&C
	[3.2.17, 3.2.18]	2008, 2006	X		• Evolution of the cross-section due to *plastic deformations*
	[3.2.19]	2012	X		• Prediction where *plastic deformation* may occur through a quantitative index (PEEQ)
	[3.2.20]	2011	X		• *Wear* qualitative prediction using VAMPIRE software
	[3.2.21]	2011	X		• Evolution of the cross-section due to *wear* and *plastic deformations*
Predicting sub-surface stresses (capabilities/limitations)	[3.2.22]	2014	X		• Distribution of contact stress fields and residual stress fields • Influence of the combined effects depending on the speed
	[3.2.23]	2002	X	X	• Qualitative prediction of sub-surface fatigue • Not tuned for crossing materials
Predicting component damage and structural fatigue	[3.2.24]	2016	X		• Investigation of current designs to aid *sleeper* failure analysis
	[3.2.25]	2014		X	• Test of five different steel grades used to create frogs • Results can be used as input in FE analyses in a design stage
Support degradation / ballast deterioration	[3.2.26]	2013	X	X	• Statistical analysis of measured data of longitudinal level at the turnout
	[3.2.27]	2014	X		• Numerical modelling of the evolution of track geometry
	[3.2.28]	2013		X	• Practical application of ballast reinforcement in a turnouts • No maintenance needed for 10 years

3.2.4 GEOMETRY OPTIMISATION OF WING RAIL

The geometry of the wing rail significantly influences the magnitude of the dynamic forces that occur in the load transfer area, i.e., when the wheel load is transferred from the wing rail to the nose, or vice versa. The passage of a freight wagon over two acute crossings with different wing rail geometries (CEN56 half and full cant) is analysed in this section. Since the wheel shape strongly influences the wheel-rail interaction, a representative set of wheels composed of the profile P10 and 20 worn wheels was selected out of a population of more than 800 wheels.

3.2.4.1 Modelling of the 3D geometry of the crossing

The 3D geometry of the crossing is modelled using SOLIDWORKS [3.2.29], as shown in Figure 3.2.8. This software allows to quickly modify and test key design parameters in order to obtain an optimised solution. The model is created based on an initial solid block and then all the geometrical operations are defined sequentially by adopting a similar methodology to that used in the machining process. The main geometrical operations are illustrated in Figure 3.2.9. Since the crossing is symmetric, a half block is modelled and mirrored in the end. The grooves are cut in steps (b) and (c) and the throat relief planning is performed in step (d). These three steps define a significant part of the crossing geometry. The rails are modelled in step (e) and the half-model is mirrored in step (f).

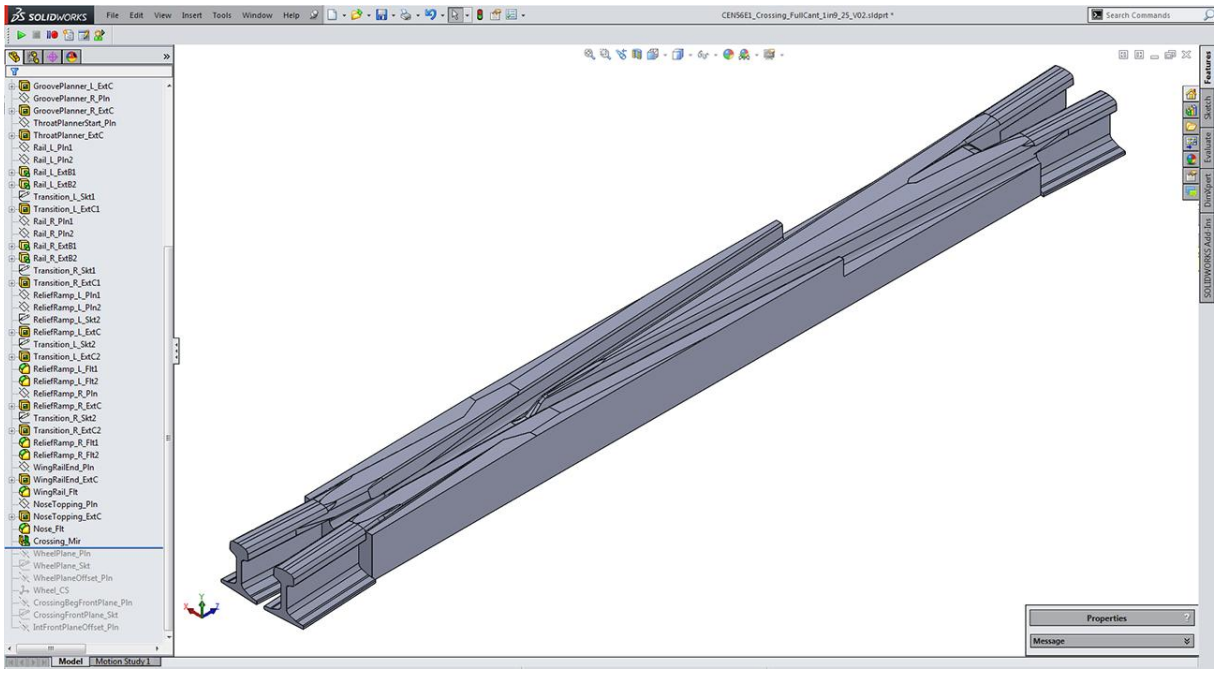

Figure 3.2.8. 3D geometry of the crossing modeled in SolidWorks.

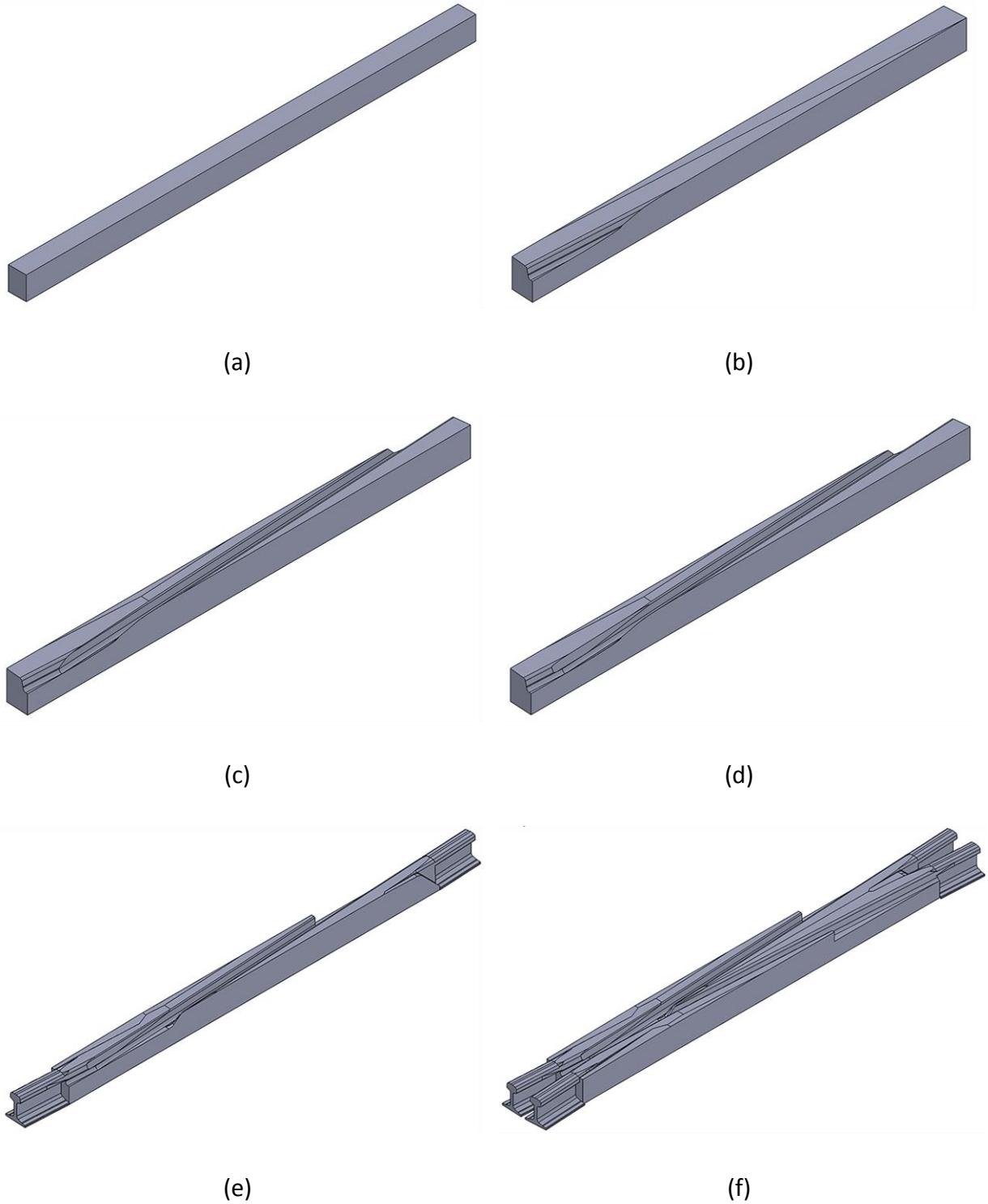

Figure 3.2.9. Main geometric operations used to create the 3D model

After the geometry is completely defined, the 2D cross-sections are exported to IGES using a computer code developed in Visual Basic for Applications for SOLIDWORKS. In order to optimise the computational time required by the multibody simulation software (MBS), a key number of cross-sections that accurately define the 3D surface are selected. The IGES containing the information of the geometric entities of the cross-sections (see Figure 3.2.10) are imported to ANSYS [3.2.30] and are meshed in order to obtain the keypoints that are used by the MBS software to define the cross-sections (see Figure 3.2.11). The lateral and vertical coordinates of the keypoints are then exported to text files. All these steps are performed automatically using the APDL scripting language [3.2.31].

The 2D cross-sections are imported to MATLAB and are further pre-processed (trimmed, smoothed, etc.) to obtain the final geometry that is used in the MBS software (see Figure 3.2.12). The dynamic analyses are performed using the software Vi-Rail, which uses an online contact search algorithm that interpolates the profiles of the crossing for each time step in order to calculate the wheel-rail contact data. All the profiles of the crossing imported to MATLAB are resampled in order to obtain an accurate 3D online profile interpolation. The 3D surface obtained is represented in Figure 3.2.13.

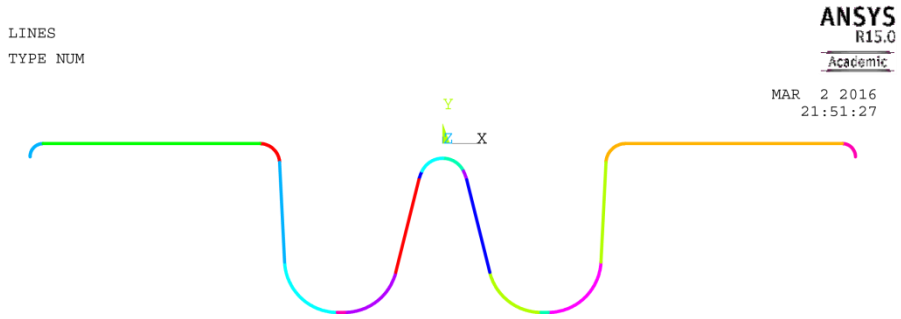

Figure 3.2.10. Geometric entities of the cross-section

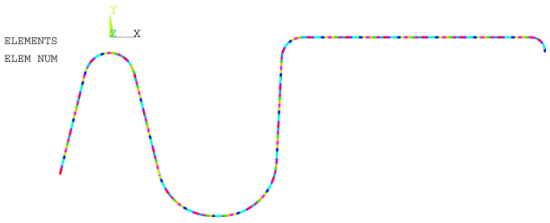

Figure 3.2.11. Mesh of the cross-section created using ANSYS

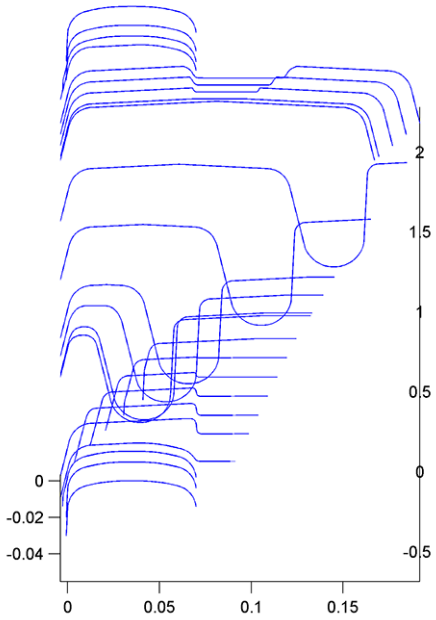

Figure 3.2.12. Cross-sections used in the MBS software

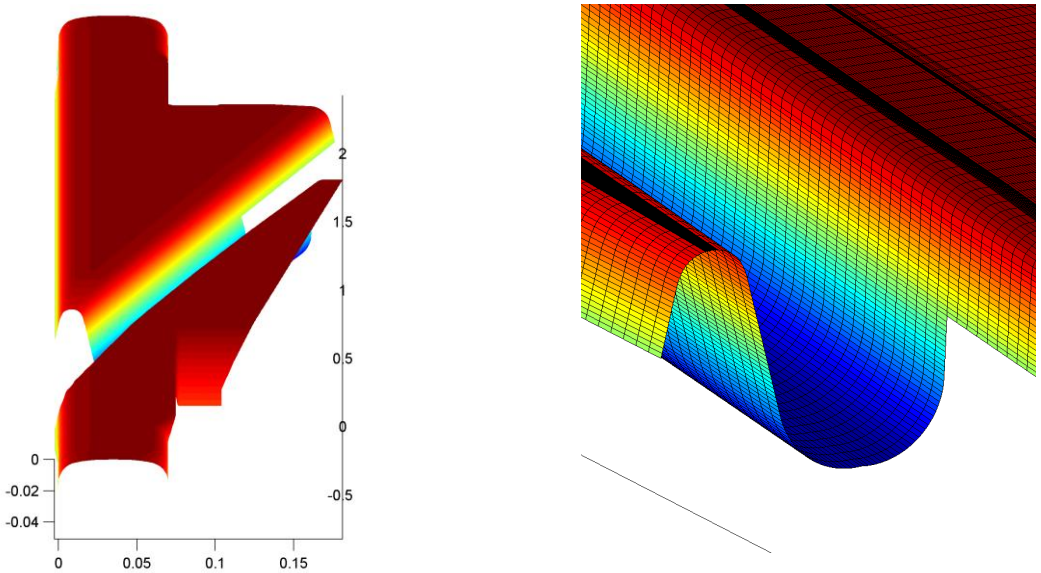

Figure 3.2.13. 3D surface of the crossing

3.2.4.2 Comparison of full cant and half cant geometry in the UK

The main difference between the cutters used to manufacture the acute crossings CEN56 half and full cant used in the UK is illustrated in Figure 3.2.14. The dashed lines represent the height of the gauge corner and the top of the rail head. In the half cant, the cutter is inclined (has a cant) up to the top of the rail head (half width of the rail head) and then is horizontal, whereas in the full cant, the cutter is inclined along the full width of the rail head. A comparison between some cross-sections of the half and full cant crossings is shown in Figure 3.2.15.

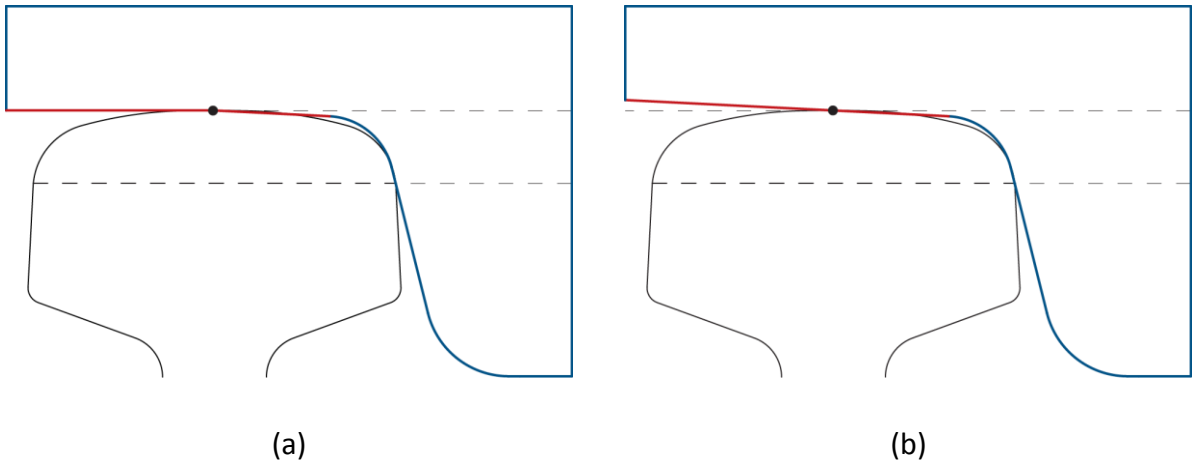

Figure 3.2.14. Main difference between the cutters used for machining the (a) half and (b) full cant crossings

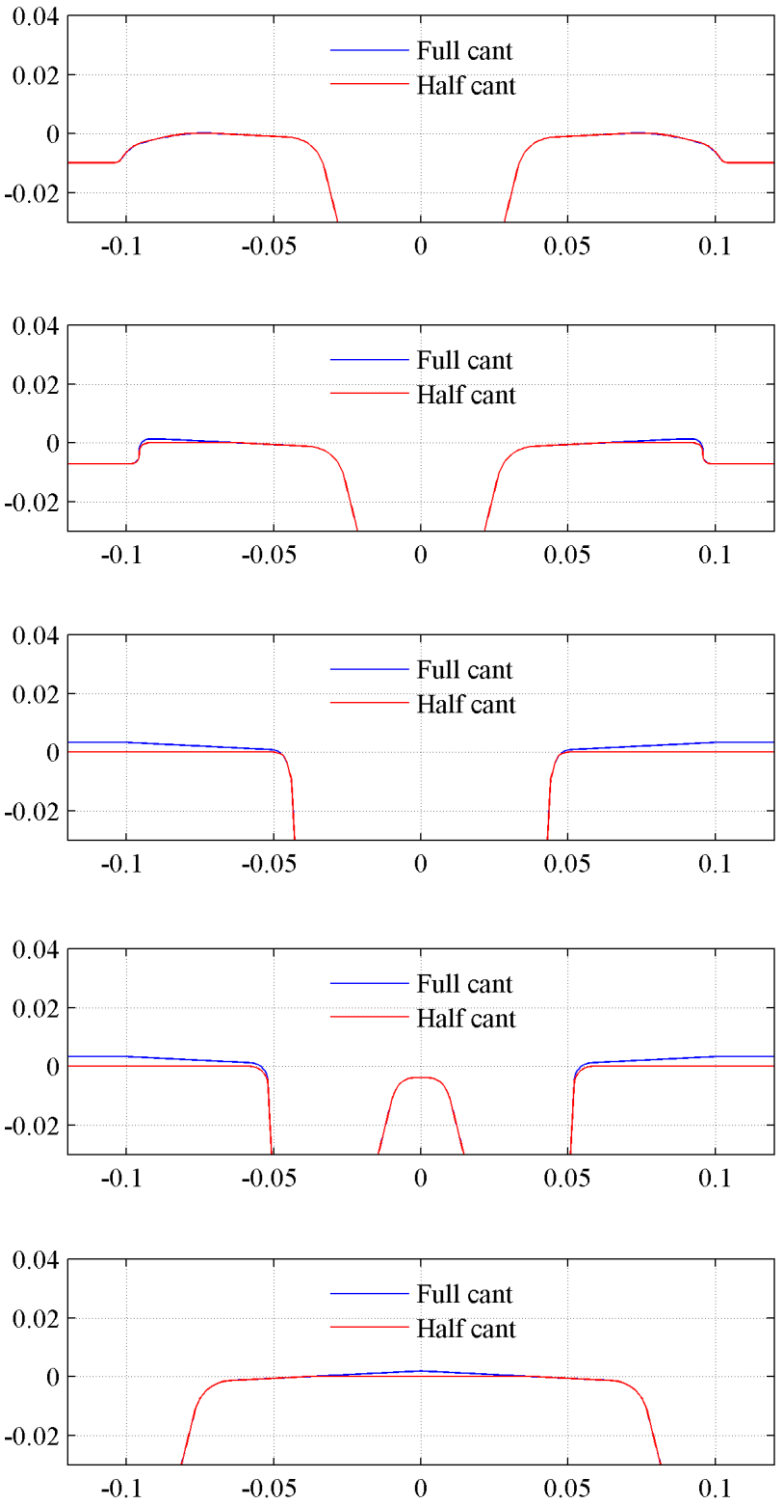

Figure 3.2.15. Comparison between some cross-sections of the half and full cant crossings

3.2.4.3 Dynamic simulation of wing geometry considering the effect of wheel shapes

The two crossing geometry presented above are simulated to predict the wheel-rail contact response and predicted damage level. The software Vi-Rail is used which offers the advantage of a non-Hertzian multi-point contact algorithm with on-line calculation of contact condition (actual rail profile interpolation at each time step). The quality of the simulation therefore depends on the pre-processing work and assumption made while preparing the geometry as explained in Section 3.2.4.1 above. Simulation conditions are as follows:

- Vehicle: freight wagon with x2 Y-series friction damped bogies. 22.5T axle load.
- Speed: 40km/h
- Wheel profiles: variable with reference P10 wheel.
- Wheel-rail interface: coefficient of friction 0.35.
- Track: straight track (through routes only) – facing move only.
- Crossing angle: $9^{1/4}$

A sample of 20 worn wheels have been selected out of a population of over 800 wheel pairs using Latin Hypercube sampling method in three dimension so as to respect the characteristics of the original sample (Figure 3.2.16) in terms of (a) Flange height, (b) Flange thickness and (c) Slope in the root of the flange (ca 50-20). This is the measure of the cone angle 50 mm from flange back (20 mm inward from the nominal radius), over a distance of 20 mm. This selection also shows a very good coverage of the equivalent conicity distribution. The selected wheels are shown in Figure 3.2.17 showing a very representative spread around the reference P10 (new) according to all characteristics above and also one selected hollow wheel.

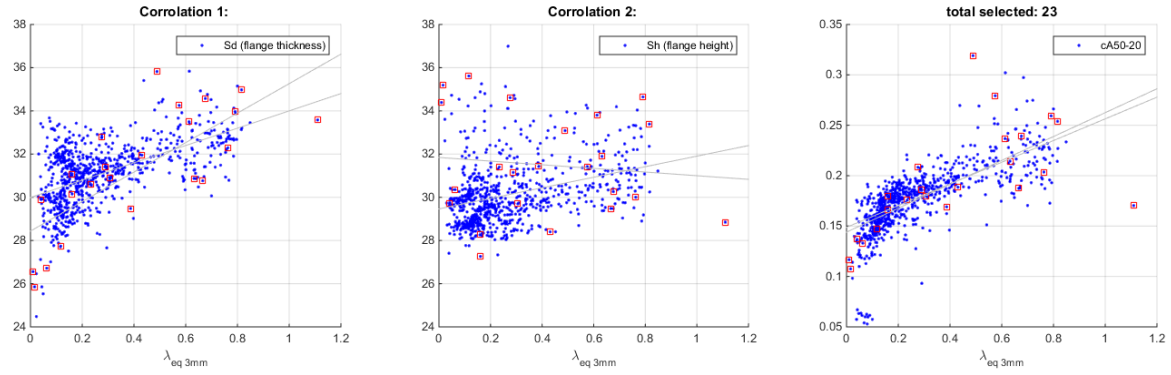

Figure 3.2.16. Selected wheels (red square) out of original population as a function of flange thickness (left), flange height (middle) and slope near flange root (right)

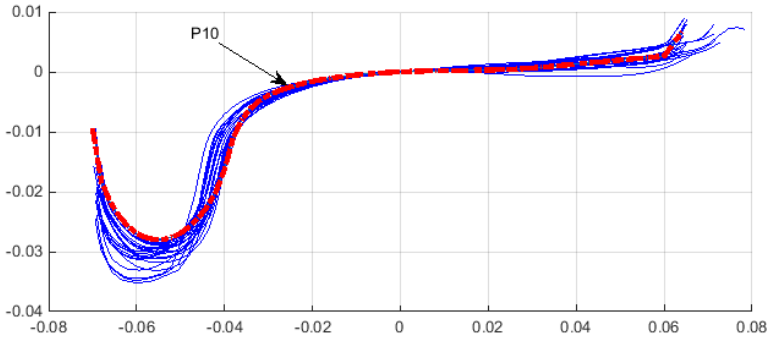

Figure 3.2.17. Selected worn wheels (solid blue) and reference P10 wheel (dashed red)

Results are hereafter presented for leading (solid lines) and trailing axle (dashed lines) of front bogie only (no major differences at straight through routes). Worn wheels are plotted in a range of blue-green hue colors while the reference P10 is plotted in bold back lines, and one selected hollow wheel is in magenta color. Leg ends and theoretical crossing point locations are indicated with vertical dashed lines.

3.2.4.3.1 Results for the half cant design geometry

In Figure 3.2.18, it is shown that in correspondence with the crossing nose, the axle experiences a small kink in the lateral direction, accompanied by a small yaw angle of attack. The wheel shape leads to some degree of variation, which is amplified after passage over the crossing.

In Figure 3.2.19, it is visible that the vertical position and movement of the wheel is affected by its shape. All wheels tend to rise up a little when they enter the crossing leg end, and some wheels move to a lower position while transiting from wing to nose, but without necessarily affecting the equivalent dip angle. The hollow worn wheel has a peculiar behaviour as it is able to maintain its height over a longer distance before it contacts with the crossing nose further along the vee, thus maintaining a higher vertical position and less amplitude of vertical movement.

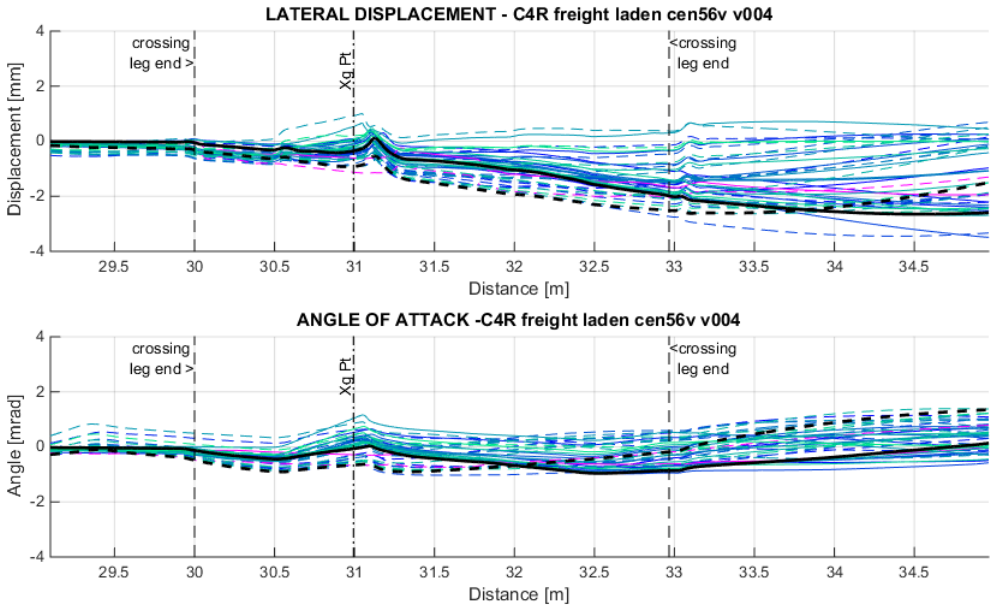

Figure 3.2.18. Axle lateral displacement (top) and angle of attack (bottom)

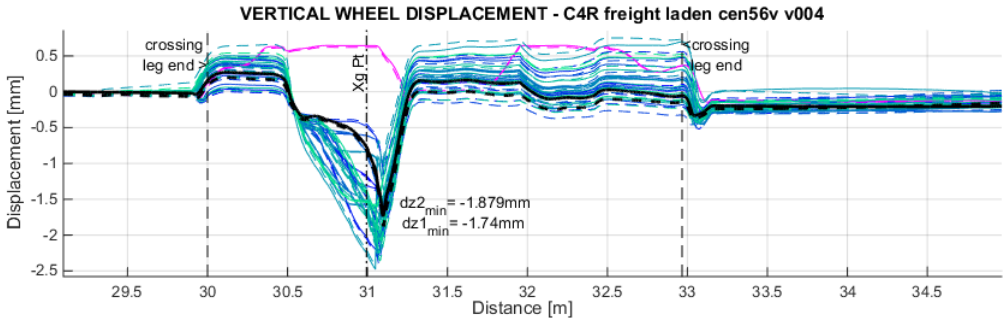

Figure 3.2.19. Wheel vertical displacement showing lowest point

In Figure 3.2.20, the lateral forces on both left and right rails show dynamic input in the area of the load transfer (crossing nose). The force can be significant on both rails up to 25 kN. Some minor dynamic effects are also observed in the leg ends reflecting a change in contact condition when the shape of the rail changes from normal to the crossing machined shape. Further dynamic effects are also seen in correspondence with the wing rail diverging, also leading to a change in contact conditions.

In Figure 3.2.21, the dynamic vertical wheel force on the crossing is in the order of twice the nominal wheel load for the P10 wheel. This also induces increased dynamic force on the opposite rail about 1.3 higher than nominal. Some variations are observed because of wheel shape. One particular wheel leads to larger force as it takes an earlier contact with the crossing nose. This is a wheel with on average increased conical shape, meaning it drops down faster as the wing rail moves away and therefore contacts the crossing nose on an earlier part with a more drastic change in vertical acceleration and therefore force. The hollow worn wheel on the other hand contacts the nose at a further position and shows less vertical impact load.

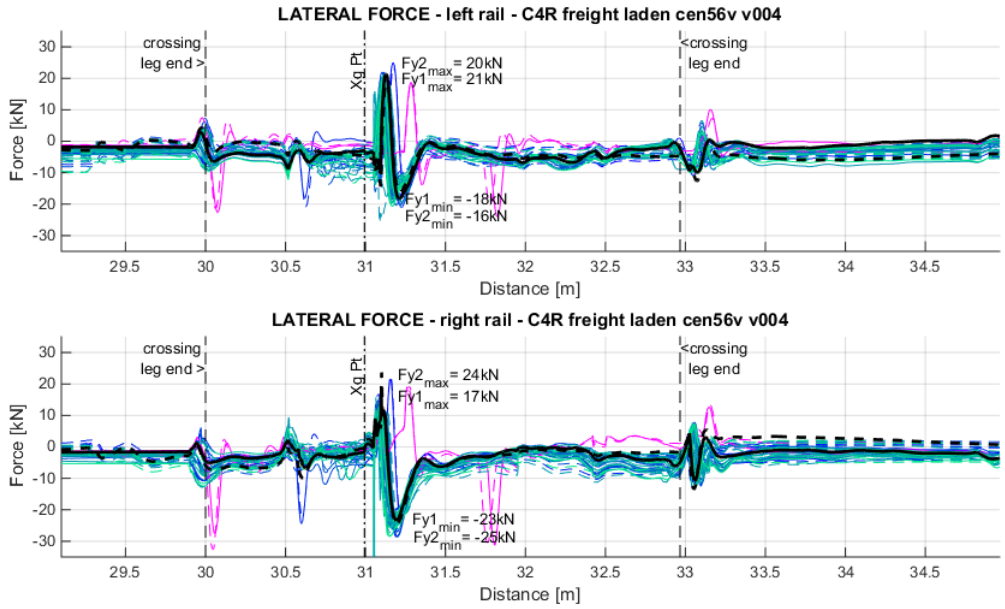

Figure 3.2.20. Lateral forces on half cant crossing rail (bottom) and opposite rail (top)

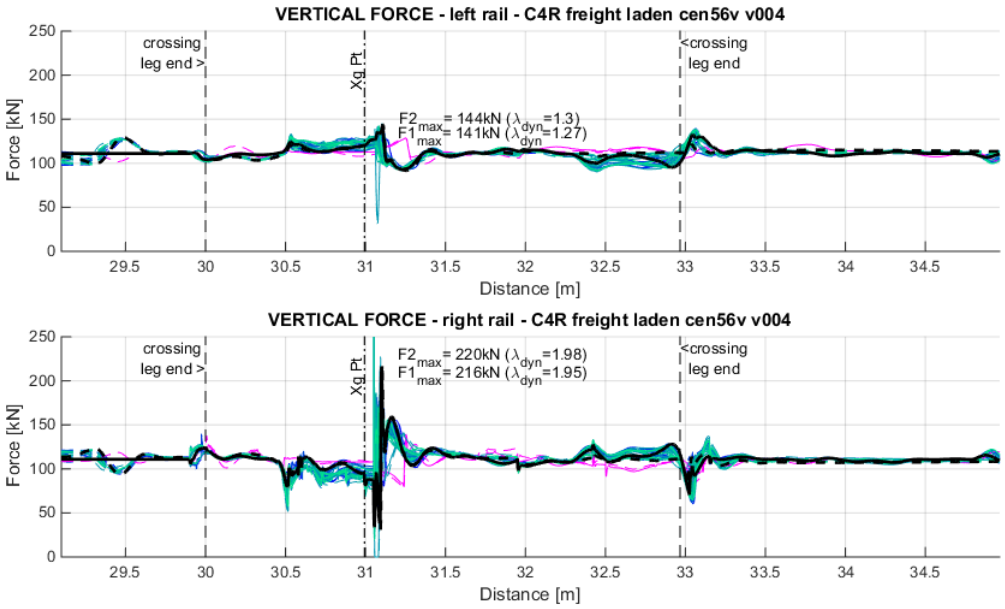

Figure 3.2.21. Vertical forces on half cant crossing rail (bottom) and opposite rail (top)

In Figure 3.2.22, the contact stresses are shown to increase by two or three times on the crossing geometry with respect to the normal running rail as the contact conditions are compromised by the machined shape of the crossing. The highest stresses are seen at the crossing nose load impact zone, while on the wing rail they are generally lower.

In Figure 3.2.23, surface fatigue is shown on the crossing nose and with the range of wheels, further fatigue may appear where the wing rail changes direction and in correspondence with the crossing nose, as well as further along the vee. Subsurface index in Figure 3.2.24 shows similar behaviour with the highest index on the crossing nose.

In Figure 3.2.25, the contact energy Tγ is locally very high on the crossing nose at the load transfer location. High energy is also observed on the opposite rail in correspondence with the contact moving away on the wing rail. Depending on the wheel state this might translate in RCF or in wear. Further, high energy is seen toward the exit leg end as the axle tends to oscillate away from centrally aligned position. This is clearly explained in Figure 3.2.26 showing in red contact conditions with high energy leading to fatigue damage and in green those leading to wear. Not that limits for grade 350 are used for the crossing and grade 260 for the opposite rail. The change of contact conditions is clearly visible at both leg ends, while a wider contact band occurs on the wing rail and a much thinner one on the crossing nose. The hollow wheel contacts in a completely different location towards the field side.

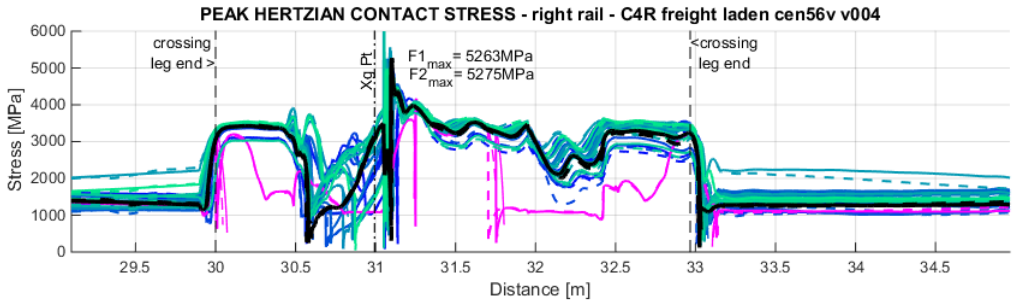

Figure 3.2.22. Equivalent Hertzian contact stress on half cant crossing rail

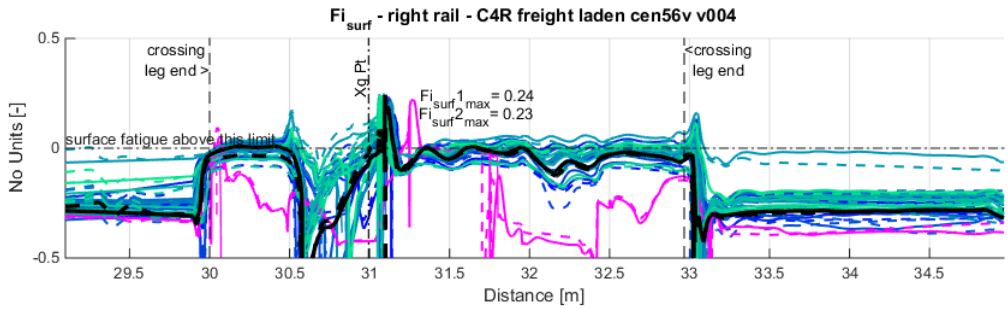

Figure 3.2.23. Surface fatigue index on half cant crossing rail

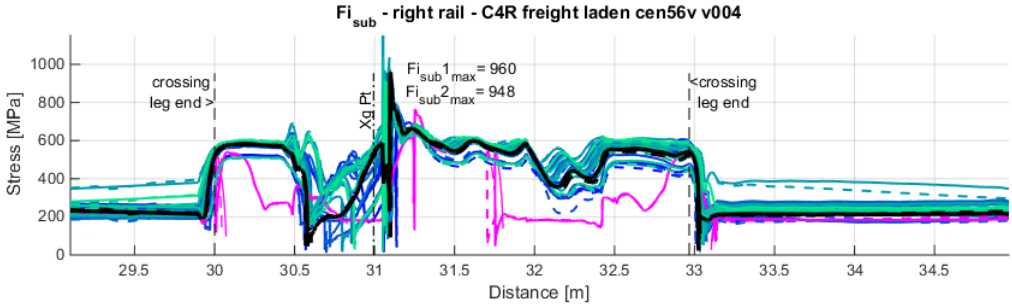

Figure 3.2.24. Subsurface fatigue index on half cant crossing rail

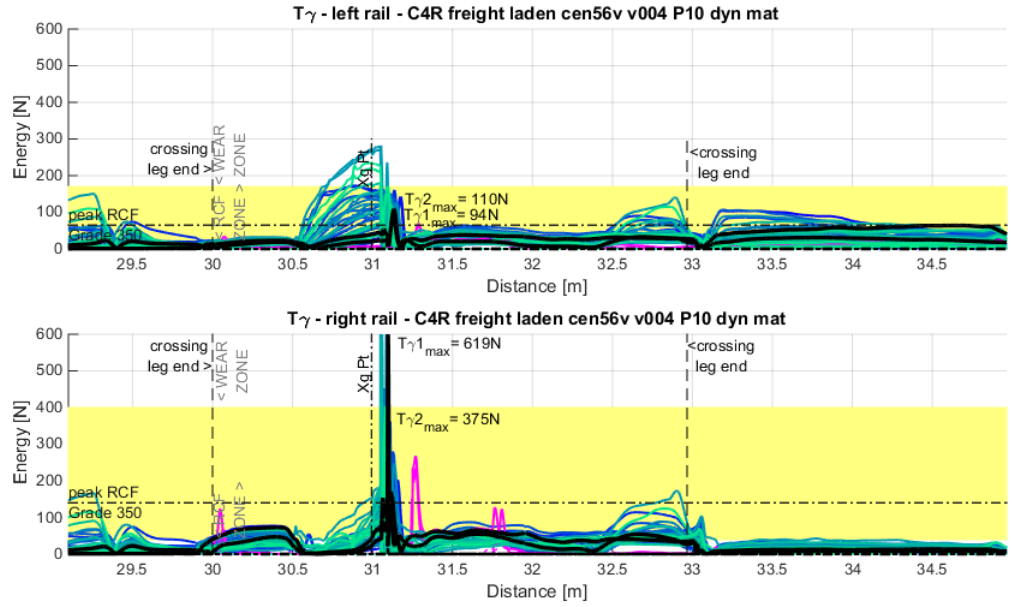

Figure 3.2.25. Tgamma energy on half cant crossing rail (bottom) with 350HT equivalent damage limits and opposite rail (top) with R260 damage limits – area in yellow indicates risk of RCF

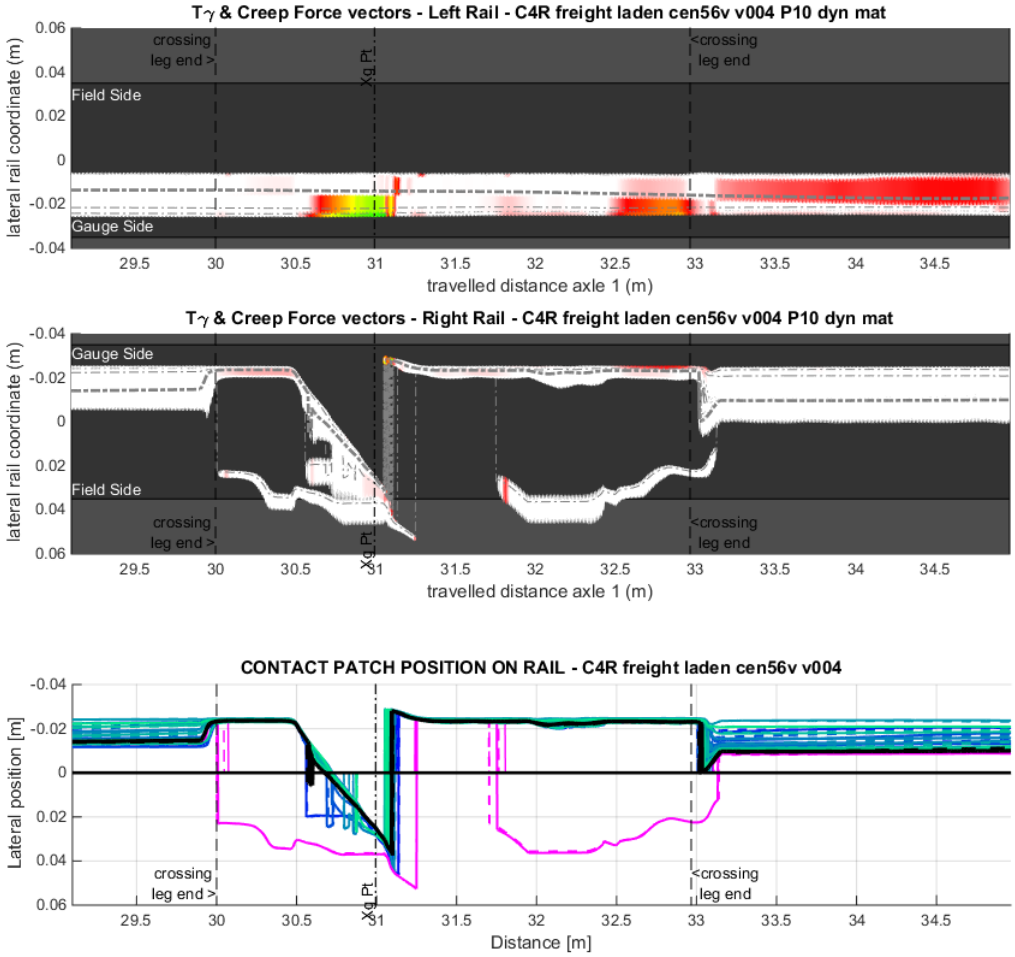

Figure 3.2.26. Cumulative contact band and coloured Tgamma damage level based on R350 grade on half cant crossing rail (bottom and middle) and opposite rail (top) based on R260 grade

3.2.4.3.2 Results for CEN56 full cant design geometry

In Figure 3.2.27, it is shown that in correspondence with the crossing nose, the axle also experiences a small kink in the lateral direction, accompanied by a small yaw angle of attack. The difference with the half cant is that, at least for the new wheel P10, the axle remains more centrally aligned through the crossing, while worn wheels are diverging some more. It is also visible on the full cant that the hollow wheel shows more deviation than the other worn wheels.

In Figure 3.2.28, it is visible again that the vertical position and movement of the wheel is affected by its shape. Some wheels move to a lower position but again without necessarily affecting the equivalent dip angle. The hollow worn wheel again has a peculiar behaviour where it is raised higher by the full cant wing rail until it eventually contact onto the crossing nose further along than the

other wheels. There is also a change of contact condition and height as it move onto the wider part of the vee.

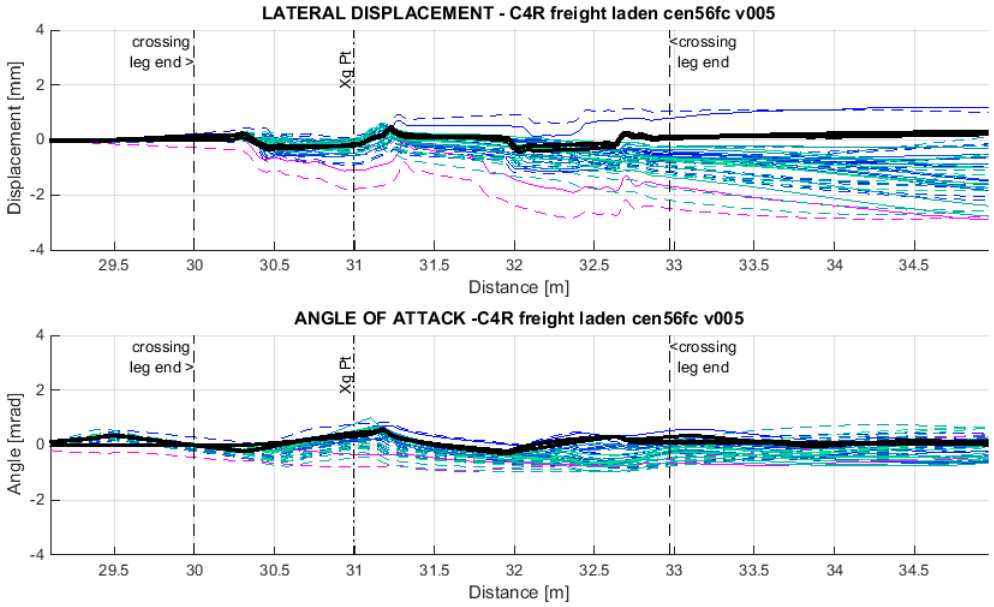

Figure 3.2.27. Axle lateral displacement (top) and angle of attack (bottom)

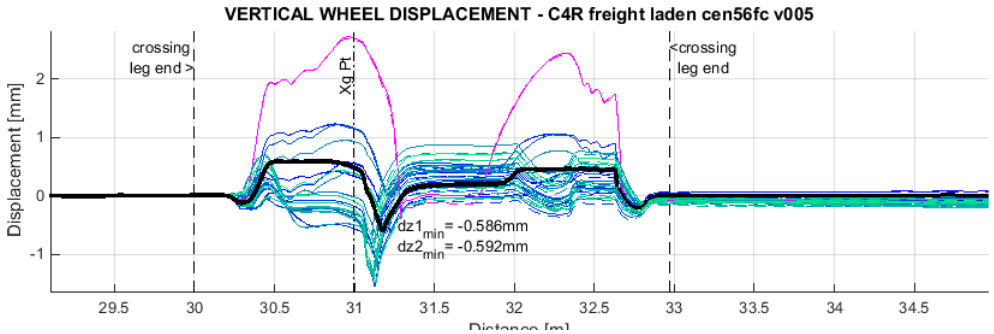

Figure 3.2.28. Wheel vertical displacement showing lowest point

In Figure 3.2.29, the lateral forces on both left and right rails are also significant in the area of the load transfer (crossing nose). However with the full cant we also notice significant forces elsewhere around the leg ends and also on the wider part of the vee, associated with changes in contact conditions (double point contact and contact on the field side). This result is most likely exaggerated by the unworn crossing geometry and by not accounting for manual grinding around the leg ends which would normally smooth and blend somehow the geometries in those areas. The hollow worn wheel shows higher impact lateral forces associated with these areas.

In Figure 3.2.30, the dynamic vertical wheel force on the full cant crossing is this time much lower for the reference wheel P10 with less than 1.3 times the nominal force (as opposed to 2 times for the half cant). This also translates in less dynamic force on the opposite rail of less than 1.2 times

nominal (as opposed to 1.3 times for the half cant). On the other hand the worn wheels generally show an increase in dynamic force which approaches that seen on the half cant (up to 2 times nominal). Increased conicity does not affect the response as much as on the half cant because the inclined wing rail allows a better support for most wheels thus maintaining their height better when the wing rail diverges. The hollow wheel however this time shows a large peak of high frequency force (P1) when it contacts the crossing nose.

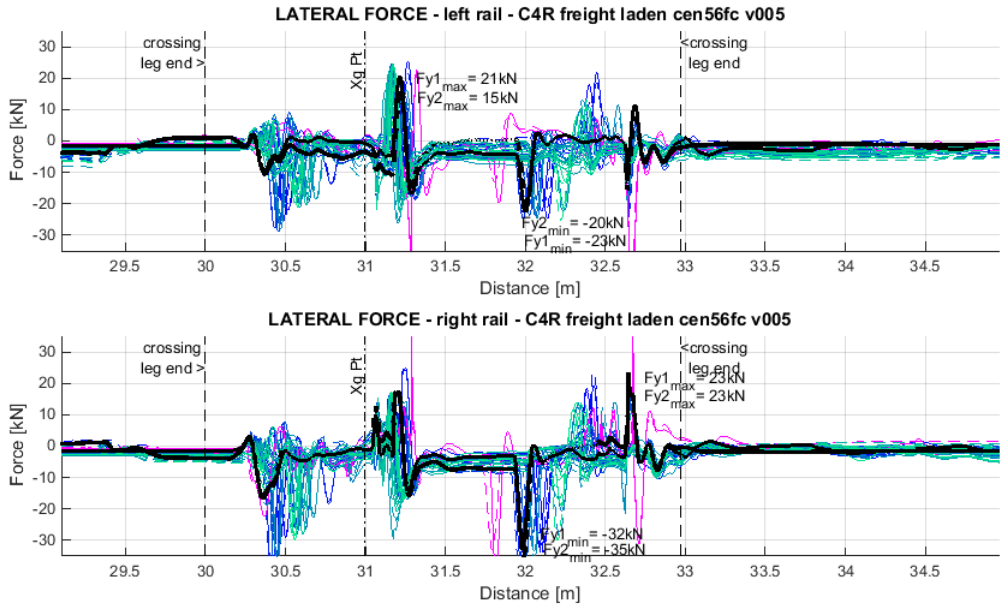

Figure 3.2.29. Lateral forces on full cant crossing rail (bottom) and opposite rail (top)

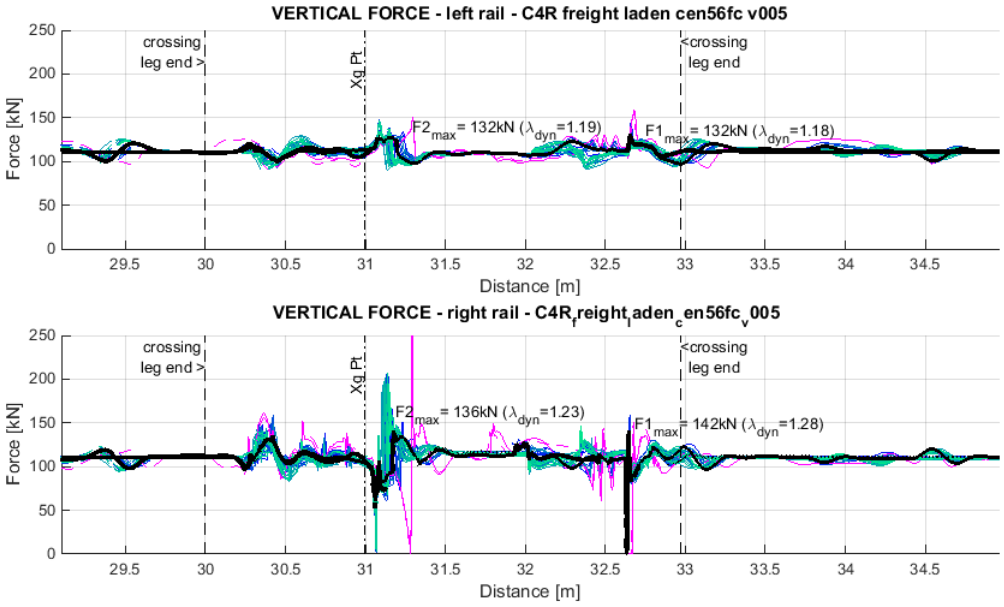

Figure 3.2.30. Vertical forces on full cant crossing rail (bottom) and opposite rail (top)

In Figure 3.2.31, the contact stresses are shown to be maintained better on the full cant with respect to the nominal running rail and for the reference P10, until it reaches the crossing vee. The highest stresses are seen right at the loads transfer onto the nose (smaller contact radius and highest force). The wheels otherwise show a lot of variation on the rest of the casting, towards either leng ends.

In Figure 3.2.32, surface fatigue is shown predominantly on the crossing nose and with the range of worn wheels, further fatigue appears on the crossing vee and where changes in contact condition occur.

Subsurface index in Figure 3.2.33 shows similar behaviour with the highest index on the crossing nose. The hollow wheel might also show some higher risk associated with changes in contact conditions.

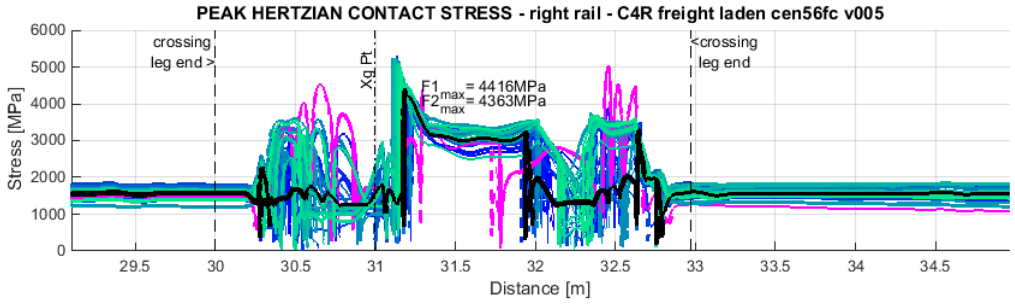

Figure 3.2.31. Equivalent Hertzian contact stress on full cant crossing rail

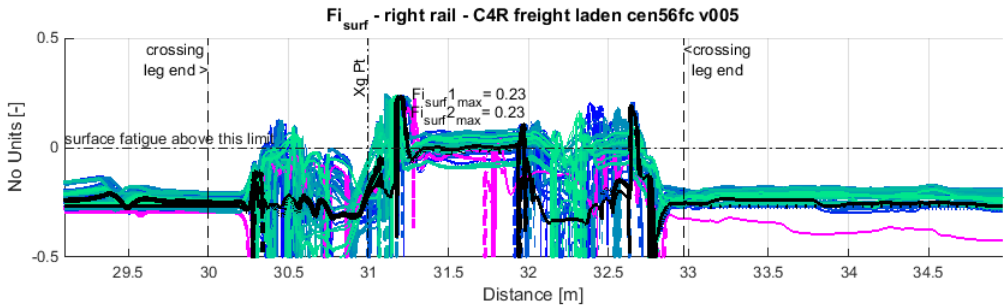

Figure 3.2.32. Surface fatigue index on crossing rail

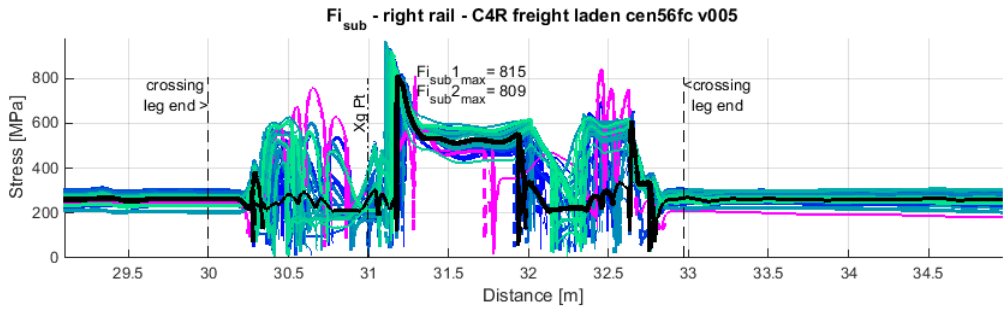

Figure 3.2.33. Subsurface fatigue index on full cant crossing rail

In Figure 3.2.34, the contact energy Tγ is locally very high on the crossing nose at the load transfer area. With respect to the half cant geometry, the range of wheels appears to show more variations both in amplitude and in longitudinal position of the peak wear damage on the nose. Higher energy closer to the peak RCF are visible along the crossing in other parts. High energy is also observed on the opposite rail in correspondence with the wing rail diverging. Further, high energy is also seen toward both leg ends. The contact conditions presented in Figure 3.2. clearly show in red contact conditions with high energy leading to fatigue damage both on the crossing and on the opposite rail. The increase in rail damage of the full cant with respect to the half cant is clearly visible here.

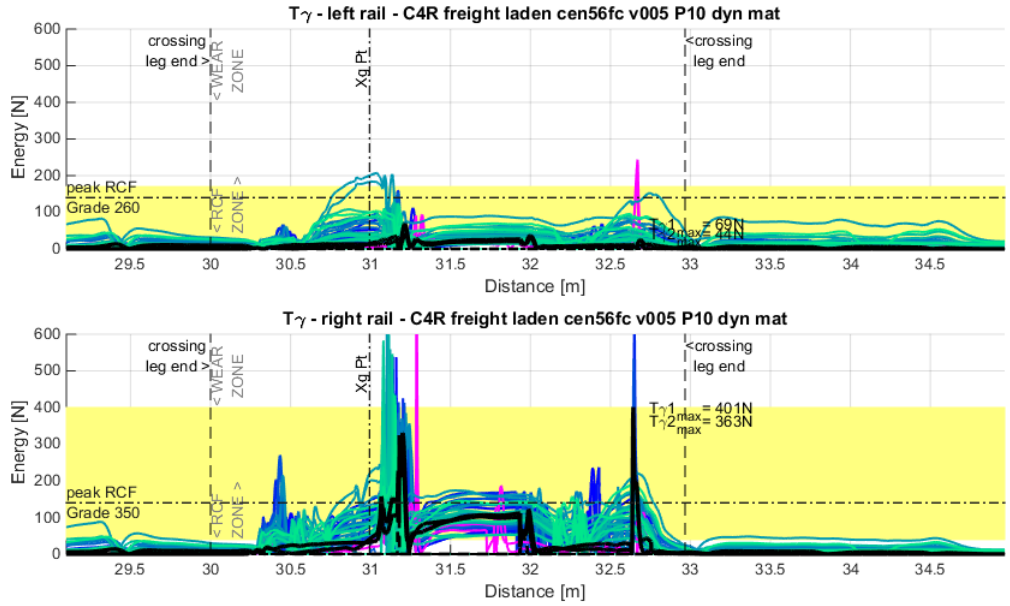

Figure 3.2.34. Tgamma energy on full cant crossing rail (bottom) with R350 equivalent damage limits and opposite rail (top) with R260 equivalent damage limits – area in yellow indicates risk of RCF

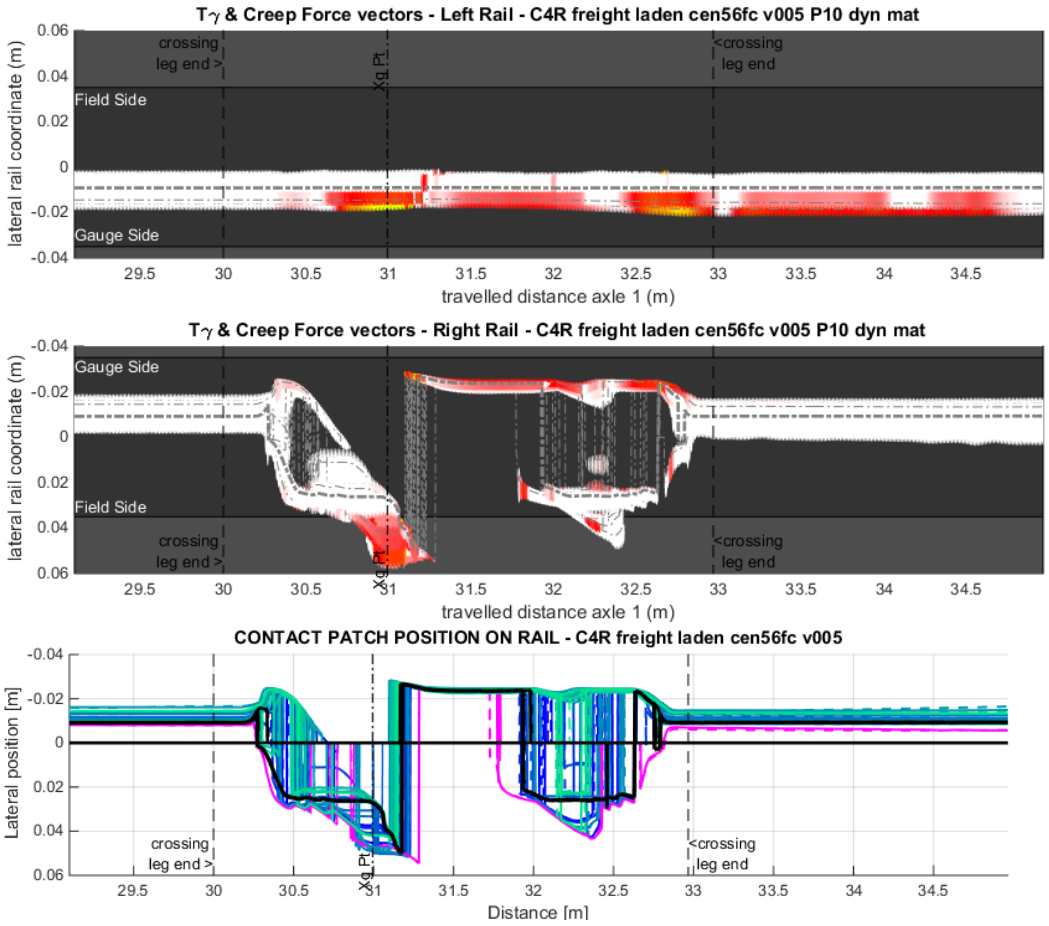

Figure 3.2.35. Cumulative contact band and coloured Tgamma damage level on full cant crossing rail based on R350 grade (middle and bottom) and opposite rail based on R260 grade (top)

3.2.4.3.3 Final comparison of half cant and full cant

Figures 3.2.36 and 3.2.37 show the lowest vertical wheel position (at load transfer point) and the corresponding peak dynamic force magnitude, respectively. The reference P10 and mean values for all wheels are indicated with horizontal black and red lines respectively, for full cant (solid) and half cant (dash). It is clear that the full cant leads to lower vertical movement of the wheel and therefore lower vertical peak forces on average. Note that the half cant shows a few wheels imposing a very high dynamic impact load. This has implications on the damage made to support elements and ballast, as well as potentially to casting fatigue. Taking into account worn wheels shows on average an increase in dynamic behaviour. On the other hand damage of the rail surface and subsurface is more complicated to compare, but the half cant appears to be less affected than the full cant by both RCF and wear. More detailed analysis and update of the damage models based on reliable material data for cast Mn is required to take these conclusions further.

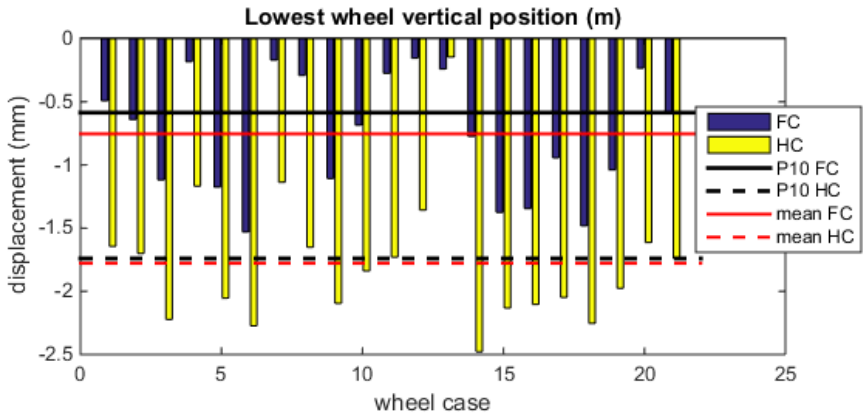

Figure 3.2.36. Peak lowest vertical position of wheel comparing half cant and full cant for all wheels

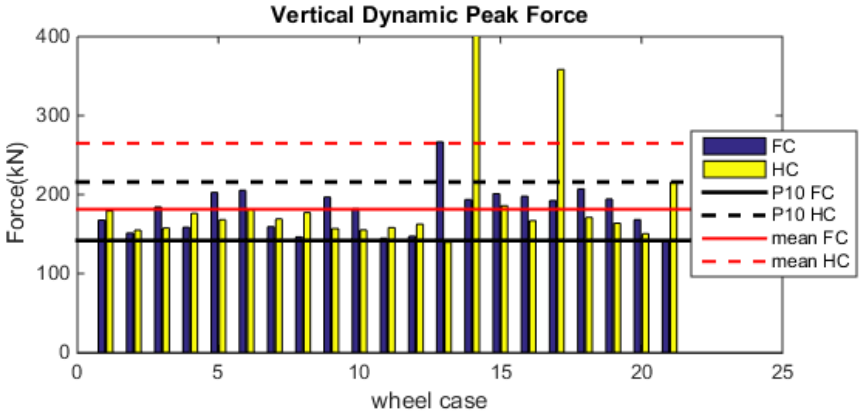

Figure 3.2.37. Peak vertical dynamics force comparing half cant and full cant for all wheels

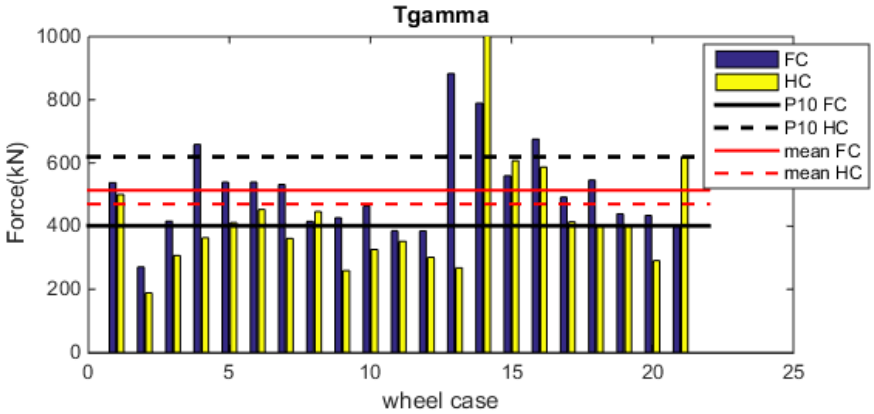

Figure 3.2.38. Peak Ty comparing half cant and full cant for all wheels

3.2.5 OPTIMISATION OF SUPPORT STIFFNESS IN BALLASTED TRACK

The potential benefit of support optimisation has been demonstrated within INNOTRACK project, however this numerical optimisation was carried out model with model having idealized constant moving track model [3.2.32]. Two S&Cs (UIC60-760-1:15) were eventually installed at Eslöv, Sweden and tested under dense traffic conditions, one of which had lower vertical stiffness and resilient baseplates. The simulation presented here aims to advance on the methodology used in Innotrack by introducing a discrete Finite Element description of the track support to show how this optimization process can be used. Results show that reducing the track stiffness from 500 to 85 kN/mm leads to significant lower normal contact forces. This reduction increases further with increasing speed. Therefore, the modification of track support stiffness in the crossing panel indicates a high potential [3.2.32] and advanced simulation techniques can be used to help identify such optimum designs.

3.2.5.1 Review of rail-pad stiffness: static and dynamic tests

In the railway system, there are two main ways to link the rail to the sleeper (Figure 3.2.39):

- Direct fastening through rail-pads (e.g. in case of 56E1 profile as reference rail profile).
- Indirect fastening through baseplate system, that includes a rail-pad and a baseplate pad (e.g. in case of 60E1 or 60E2 profile as reference rail profile).

Table 3.2.2. Static and dynamic stiffness of rail-pads and baseplate pads (pad reference dimensions: 140 x 140 mm)

Description	Thickness [mm]	Static stiffness [kN/mm]	Dynamic stiffness [kN/mm]	Dynamic/static ratio	Visual identification
Rail pad	5.5÷10.5	50÷120	80÷200	1.2÷2.4	Soft pad
Rail pad	5÷10	150÷520	600÷1300	2÷3	Medium pad
Rail pad	5	550	-	-	Hard pad
Baseplate pad	5÷10	15÷30	20÷40	1.3	
Baseplate pad	3÷5	50÷80	90÷140	1.8	

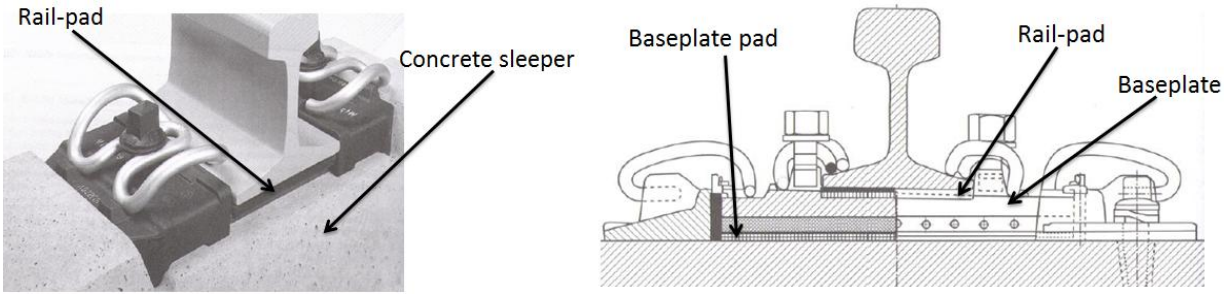

(a) (b)

Figure 3.2.39. (a) Direct fastening (Vossloh 300 fastening) and (b) indirect fastening [3.2.33]

In Table 3.2.2, some examples of static stiffness and dynamic stiffness are reported referring to an equivalent 140 x 140 mm pad.

Usually, in the crossing panel soft pads are used in case of direct fixing and medium/hard pads with soft baseplate pads in case of indirect fixing.

3.2.5.2 validation of the track model

The main scope of this investigation is to compare the model which is currently used for the dynamic simulations performed at UoH [3.2.34] and the FE model of the complete turnout currently used at Chalmers [3.2.27].

3.2.5.2.1 Description of the models used in the assessment

A representation of the UoH track model is shown in Figure 3.2.40.

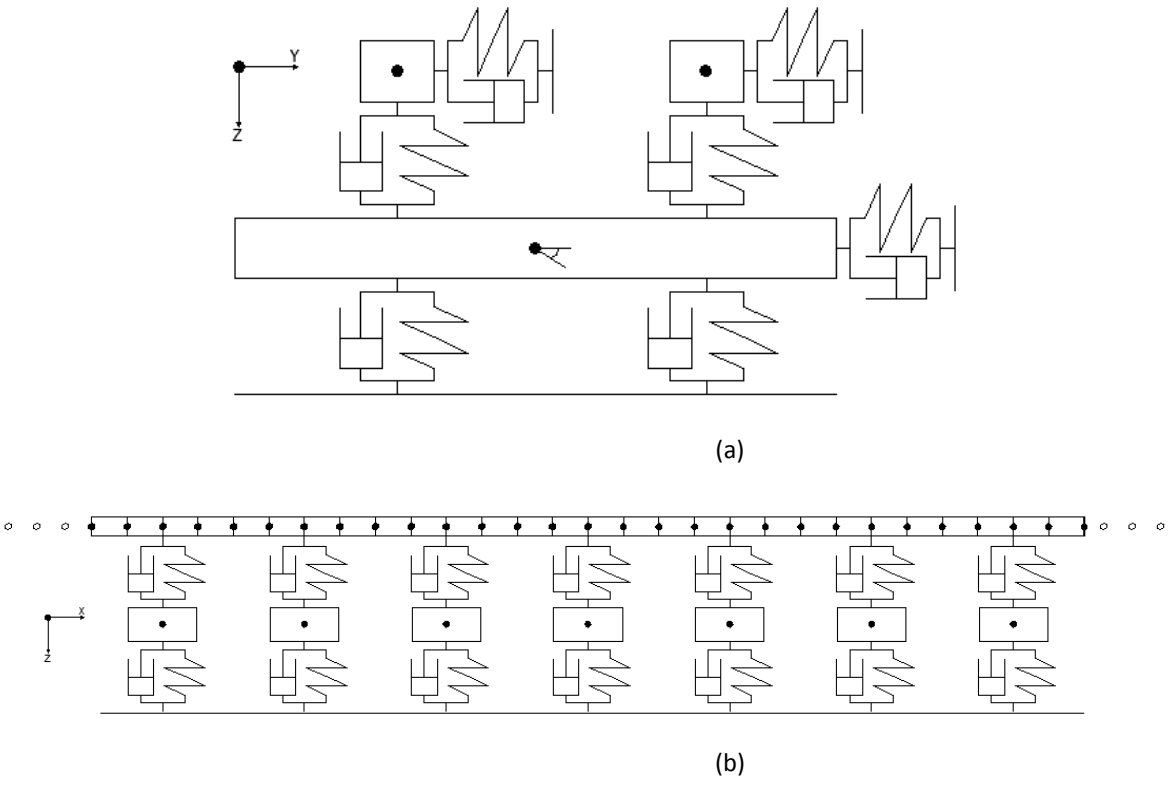

Figure 3.2.40. UoH track model in (a) y-z plane and (b) x-z plane [3.2.34]

The track is modelled as a two-layer discretely supported ballasted track, which includes the rail pad and the sleeper support resilient layers. Each node has four degree of freedom (DOFs): vertical and

lateral displacement and rotations around the y and z axes. In order to obtain accurate results and capture correctly the abrupt change in the geometrical properties, four Timoshenko beam elements are considered within each sleeper spacing. The sleepers are modelled as rigid bodies with 3 DOFs: vertical and lateral displacement and roll rotation. Note that the track properties, including the sleeper length, support stiffness and rail properties, are variable along the crossing panel, matching the site general arrangement and the crossing panel drawings.

A representation of the Chalmers track model is shown in Figure 3.2.41.

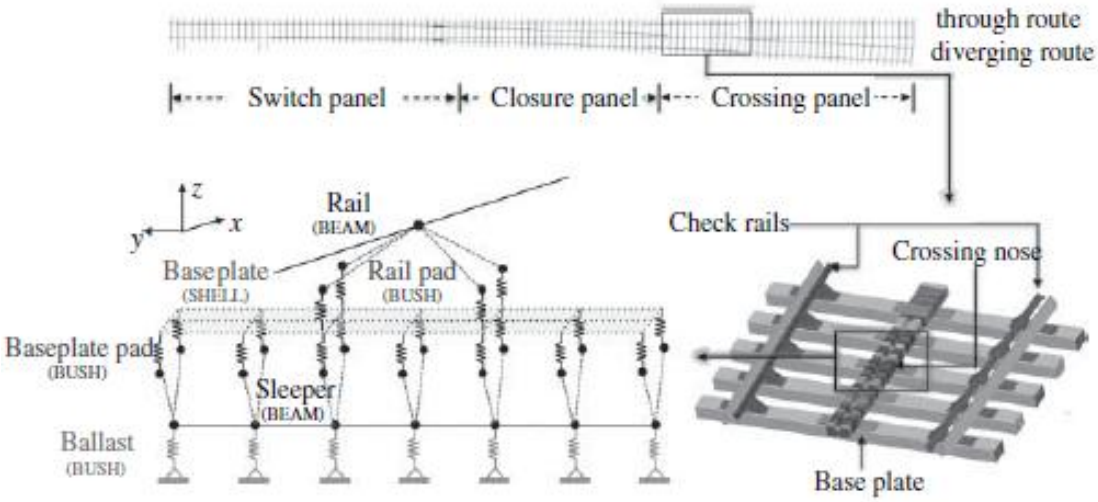

Figure 3.2.41. Chalmers FE model [3.2.27]

The FE model of a complete 60E1–760–1:15 turnout includes the switch panel, the closure panel and the crossing panel considering all the rails (stock rails, switch rails, closure rails, crossing nose, wing rails and check rails), rail pads, baseplates, baseplate pads and sleepers laying on ballast. In particular, the rails and the sleepers are modelled using beam elements and the remaining components are modelled using linear spring-dampers elements. Note that the parameter values are set in order to match the field measurements of sleeper strains and wheel-rail contact forces in a turnout at Eslöv (Sweden).

The main input data used in the two models are presented in Table 3.2.3.

Note that the UoH model does not include the baseplate system since it is common practice to have direct fixing of CEN56 crossing type to concrete sleepers.

Table 3.2.3. Main input parameters for the vehicle/track interaction model[1]

Parameter	UoH	Chalmers
Rail type	56E1	60E1
Crossing angle	1:13	1:15
Check rail type	CEN33C1	Not given
Sleeper spacing	0.71 m	Not given
Rail-pad stiffness	Ref. [2]	Ref. [2]
Support stiffness	150 MN/m³	150 MN/m³
Baseplate system	No	Yes

3.2.5.2.2 Receptance at the crossing nose

In the frequency domain, assuming stationary harmonic vibration, the equations of the vertical motion can be written as:

$$(-\omega^2[M] + i\omega[C] + [K])\hat{z}(\omega) = \hat{F}(\omega) \quad (1)$$

where:

ω = frequency of excitation [Hz] (ω=2πf);

[M], [C], [K] = mass, damping, stiffness system matrices [kg], [Ns/m], [N/m];

$\hat{z}(\omega)$ = amplitude of the complex-valued displacement [m];

$\hat{F}(\omega)$ = amplitude of the complex-valued input force [N].

Track receptance H(ω) at frequency ω is then calculated as:

$$H(\omega) = abs\left(\frac{\hat{z}(\omega)}{\hat{F}(\omega)}\right) = \frac{1}{(-\omega^2[M] + i\omega[C] + [K])} \quad (2)$$

The results from the two models in terms of receptance of the inner rail and outer rail at the crossing nose are compared in Figure 3.2.42.

Figure 3.2.42 shows a general good agreement of the results. The main differences are listed in Table 3.2.4.

The differences in terms of magnitude can be explained with the fact that the Chalmers model uses a heavier rail (60E1) than the one used in the UoH model (56E1). Also the use of baseplates shifts the resonance mode towards lower frequency due to an added mass and stiffness.

[1] The support stiffness is converted to linear spring taking into account the actual sleeper area.

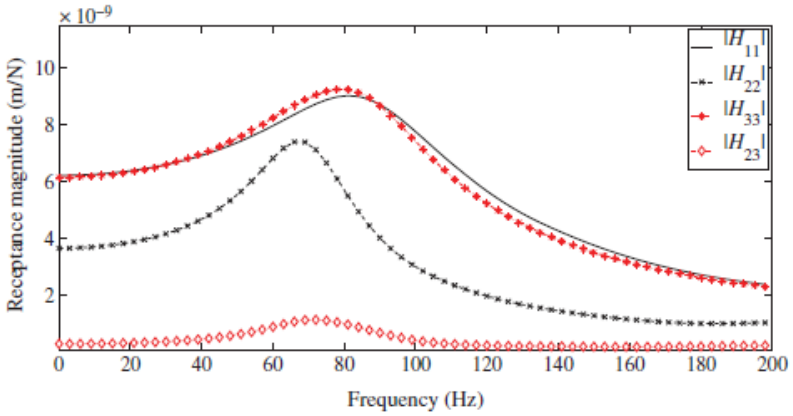

(a)

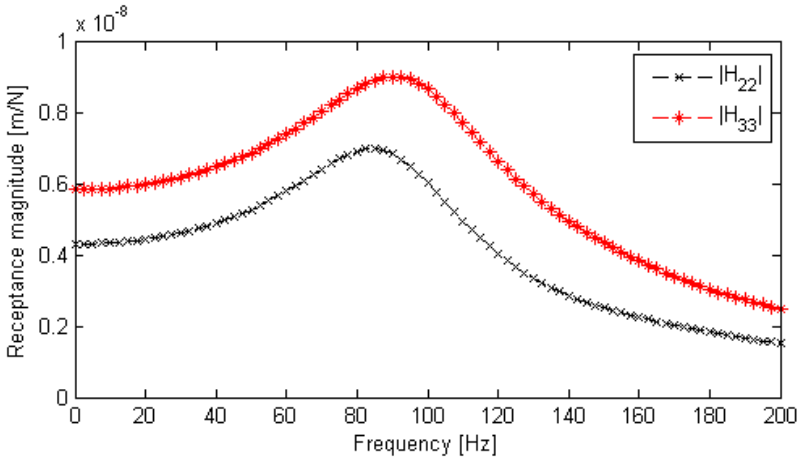

(b)

Figure 3.2.42. Receptance magnitude at the crossing nose for the (a) Chalmers model and (b) UoH model ($|H_{22}|$: direct receptance at the inner rail; $|H_{33}|$: direct receptance at the outer rail)

Table 3.2.4. Main differences between the UoH model and Chalmers model

	UoH	Chalmers	Difference
Frequency at the peak – Inner rail	90 [Hz]	79 [Hz]	14%
Frequency at the peak – Outer rail	82 [Hz]	65 [Hz]	26%
Magnitude at the peak – Inner rail	9.03 [10^{-8} m/N]	9.7 [10^{-8} m/N]	-7%
Magnitude at the peak – Outer rail	7 [10^{-8} m/N]	7.3 [10^{-8} m/N]	-4%
Magnitude at 0 Hz – Inner rail	5.9 [10^{-8} m/N]	6 [10^{-8} m/N]	-2%
Magnitude at 0 Hz – Outer rail	4.3 [10^{-8} m/N]	3.95 [10^{-8} m/N]	9%

3.2.5.2.3 Static stiffness along the crossing panel

The normalised static track stiffness has been evaluated for the complete crossing panel and the results are compared in Figure 3.2.43.

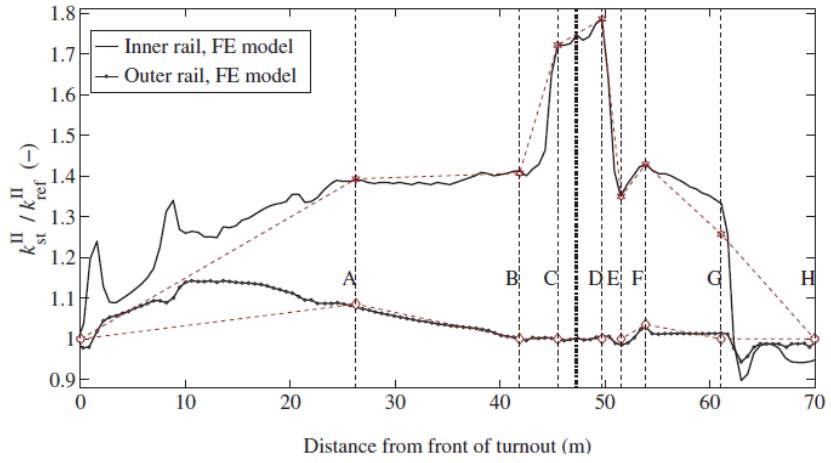

(a)

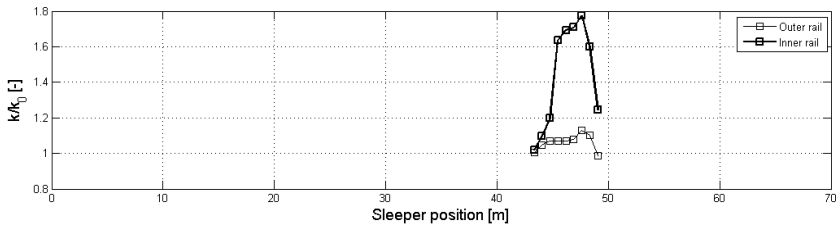

(b)

Figure 3.2.43. Normalised static track stiffness along through route of turnout for the (a) Chalmers model and (b) UoH model

Also in this case it is possible to notice a good agreement between the two models. For example, at the crossing nose the normalised track stiffness for the inner rail is ca. 1.74 in the Chalmers model and ca. 1.7 in the UoH model, with a relative difference of 3%.

The main difference between the two models is at the outer rail in correspondence of the crossing panel, with a relative difference of ca. 6%. This discrepancy can be explained with the fact that in the

UoH model the check rail is considered as an additional mass to the nominal profile and a different cross section is used to calculate inertial properties.

3.2.5.3 Theoretical considerations on optimising track stiffness

Theoretical considerations about optimising the total track stiffness along the crossing panel are presented, without considering the dynamic behaviour of the system.

3.2.5.3.1 Optimisation of the track support stiffness

In a crossing panel there is a significant longitudinal variation of the vertical track stiffness mainly due to the increase casting bending properties and the use of long bearers. This contributes to dynamically induced vibrations and accelerations of the panel and associated degradation processes. Accepting that bearers, casting and ballast support cannot easily be changed, the profile of overall stiffness may be partially controlled by choosing appropriate bearer to casting support stiffness elements in order to obtain an overall rigidity as smooth as possible along the panel.

In this study, an optimisation process has been implemented in order to find the pad stiffness distribution along the crossing panel that makes the track overall stiffness as smooth as possible. The track model is established in Section 3.2.5.2.1.

Five variables are used in the optimisation process when a crossing angle equal to 1 in 9.25 is considered and seven variables for longer crossings (i.e. crossing angle equal to 1 in 13). They represent the rail-pad stiffness at each sleeper along the crossing panel. The range considered for both variables is from 20 to 400 MN/m with steps of 10 MN/m. It is based on typical values for commercial very soft and soft railway pads [3.2.35].

The optimisation problem can be written as follows:

$$\min_{x \in X_{possible}} F(x) \tag{3}$$

where:

x = vector of the rail-pad stiffness [MN/m];

$X_{possible}$ = range of possible values for the rail-pad stiffness [MN/m];

$F(x)$ = objective function:

$$F(x) = \sum_{i=1}^{n_s} \frac{|H(i) - \bar{H}(i)|}{\bar{H}(i)} \tag{4}$$

where:

n_s = number of sleepers considered;

H(i) = track stiffness at the *i*-th sleeper [MN/m];

$\overline{H}(i)$ = target value of track stiffness at the *i*-th sleeper [MN/m].

It is necessary to guarantee that the track stiffness function is monotonously increasing until the sleeper n.5 and monotonously decreasing afterwards.

Thus, in the ascending part of the curve:

$$0 \leq \sum_{i=1}^{n_{cr}} \frac{H(i+1) - H(i)}{H(i)} \leq 20\% \tag{5}$$

and in the descending part of the curve:

$$-20\% \leq \sum_{i=n_{cr}+1}^{n_s} \frac{H(i+1) - H(i)}{H(i)} \leq 0 \tag{6}$$

where:

n_{cr} = sleeper number at the crossing nose.

3.2.5.3.2 Results

Figure 3.2.44 shows the trend of track stiffness along the crossing panel considering both optimised and constant rail-pad stiffness.

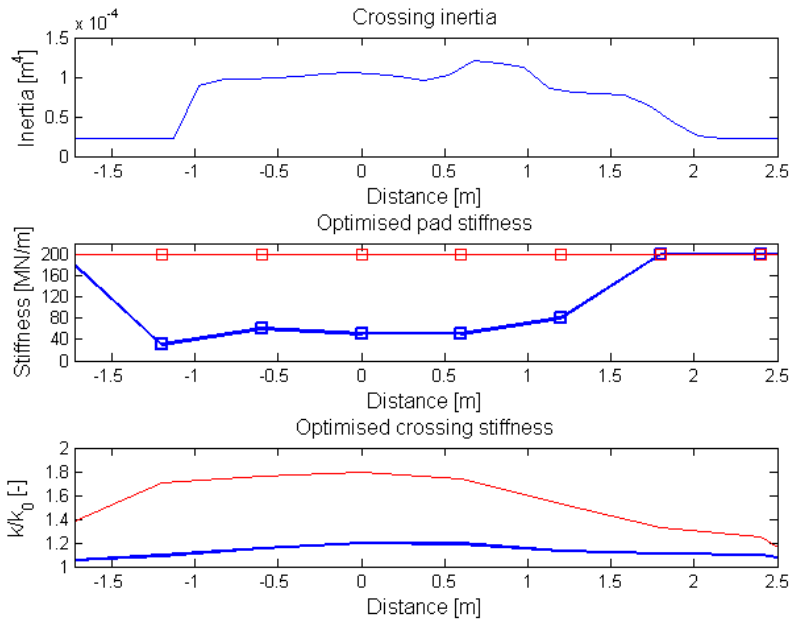

(a)

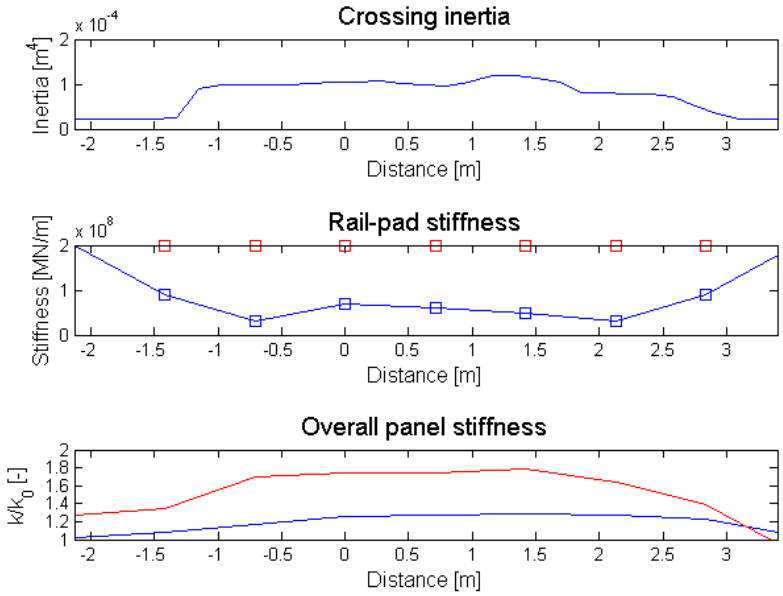

(b)

Figure 3.2.44. Crossing inertia, rail-pad stiffness and normalised track stiffness along the crossing panel versus distance for (a) 1 in 9.25 angle and (b) 1 in 13 angle (—: constant rail-pad stiffness; —: optimised rail-pad stiffness)

From Figure 3.2.44 it is possible to notice that it is possible to obtain the desired parabolic stiffness support distribution using one parameter (X_1) along the crossing panel in case of short crossings and two optimisation variables (X_1 and X_2) along the crossing panel and at the edges in case of longer crossings.

3.2.5.4 Methodology of the support optimisation at the crossing panel

The flow chart describing the optimisation process used in the present study is shown in Figure 3.2.45.

The long-term behaviour of the system is assessed through macro indices which can give an indication of severity, velocity and location of the degradation. Three main degradation modes associated with the most common causes of failures are considered: settlement of the ballast layer, wear and Rolling Contact Fatigue (RCF) of the rails and fatigue of the track components. The macro-indices examined are:

- *Settlement*: sleeper acceleration, ballast pressure;
- *Wear/RCF*: wear, RCF;
- *Fatigue in the components*: rail-pad forces, stresses on the rail foot, stresses on the rail head.

Each of these macro-indices has been calculated as the relative difference between the case examined and the reference case. The optimum solution that minimises the total damage calculated

due the passage of a wheelset over the crossing panel is found using a genetic algorithm by varying the rail-pad stiffness.

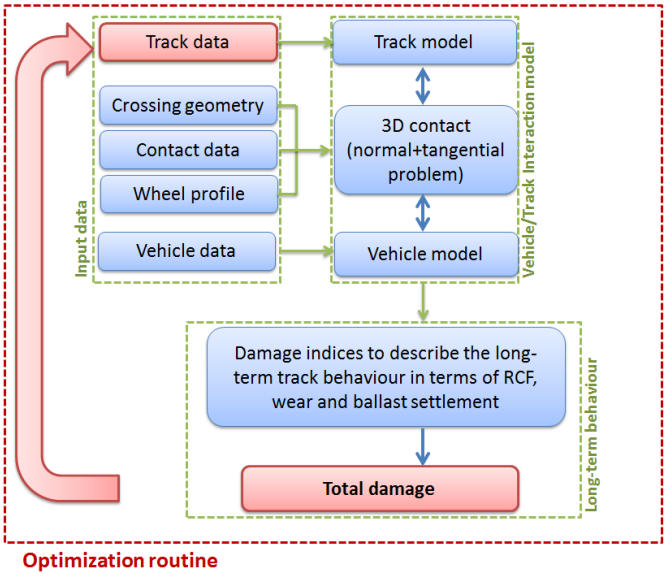

Figure 3.2.45. Flow chart of the optimization process

Since the turnout used in the simulation is a short turnout with 1 in 9.25 crossing angle (Section 3.2.5.3), it has been decided to use only one optimisation variable (Figure 3.2.46).

The range considered is based on typical values for commercial soft and medium railway pads (Table 3.2.2) from 40 to 700 MN/m with a step of 15 MN/m. Note that the reference case for dynamic rail-pad stiffness is 200 MN/m along the entire crossing panel, as well as in the plain line.

Constraints have been applied in order to obtain a variation of the track stiffness along the crossing as smooth as possible. Also, it is necessary to limit the increase of stresses at the rail foot to a reasonable range.

The vehicle/track interaction model used to calculate the dynamic response of the system is shown in Figure 3.2.47.

The track is modelled as described in Section 3.2.5.2.1.

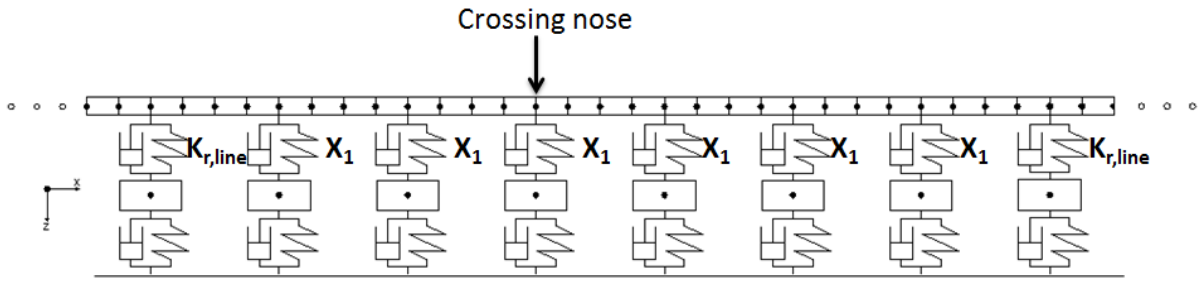

Figure 3.2.46. Choice of optimisation variable X_1

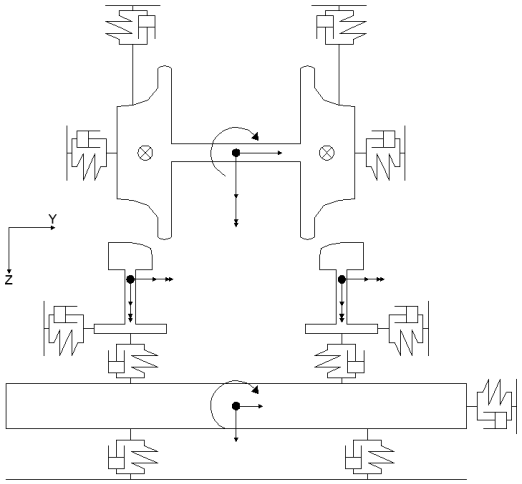

Figure 3.2.47. Vehicle/track interaction model in the y-z plane

Table 3.2.5. Main properties of the vehicle/track model

	Parameter	Value
TRACK INPUT	Rail type	56E1 vertical
	Crossing type	CEN56 1in9$^{1/4}$ acute crossing
	Check rail type	CEN33C1
	Sleeper type	Concrete sleeper
	Support stiffness	70/150/200 MN/m^3
	Baseplate system	No
VEHICLE INPUT	Axle load	22.5 t
	Unsprung mass	1500 kg
	Longitudinal and lateral primary suspension stiffness	3.6 MN/m
	Vertical primary suspension stiffness	5 MN/m
	Wheel profile	P10 profile (new/medium worn/heavily worn)
	Vehicle speed	80 km/h

A rigid single axle with primary suspensions is considered and the weight of the vehicle is applied as external force. Four DOFs are considered: vertical and lateral displacements; roll and yaw rotations.

The contact element used takes into account the normal and tangential forces present at the wheel-rail interface. The normal forces are modelled using the non-linear Hertzian theory and the tangential forces using the linear Kalker theory, corrected according to Shen, Hedrick and Elkins theory. The on-line approach is used to calculate the contact data, since it is more suitable than using contact tables in presence of significant variation of the rail cross-sections along the longitudinal direction.

The main properties of the vehicle/track model are presented in Table 3.2.5.

3.2.5.5 Results

3.2.5.5.1 Sensitivity analysis

First of all, quantitative considerations have been drawn per each macro-index by varying rail-pad stiffness. In order to perform this sensitivity study, two variables have been used: X_1 for the three sleepers along the load transfer area and X_2 at the edges of the load transfer area.

Two travelling speeds (40 and 80 km/h) are considered in this sensitivity. Note that the lowest stiffness values (20 to 40 MN/m) are investigated for sake of completeness. Usually, the super soft pads (20-40 MN/m) are used in plain line for some applications with slab track systems, while soft pads (60-90 MN/m) in the crossing panel.

In Appendix A the three dimensional plots of each degradation mode indicator varying the pad stiffness X_1 and X_2 are presented and discussed in detail. Table 3.2.6 shows a summary of the findings in terms of best solution and maximum theoretical improvement achievable per each indicator and per each speed considered.

Table 3.2.6. Summary of findings in terms of best solution and maximum theoretical improvement achievable per each indicator and per each speed considered

Degradation mode	Indicator	Speed = 40 km/h		Speed = 80 km/h	
		Best solution	Improvement (w.r.t. nominal case)	Best solution	Improvement (w.r.t. nominal case)
Settlement	Sleeper acceleration	Nominal case	0%	Medium/stiff pads	90%
	Ballast pressure	Soft pads	15%	Soft pads	80%
Wear/RCF	Wear	-	-	-	-
	RCF	Soft pads	13%	Soft pads	8%
Fatigue in the components	Rail-pad forces	Soft pads	20%	Soft pads	20%
	Stresses on the rail foot	Stiff pads	5%	Stiff pads	12%
	Stresses on the rail head	Stiff pads	5%	Stiff pads	18%

Examining the results presented in Table 3.2.6, it is possible to conclude that the maximum reductions in terms of ballast pressure, RCF and forces in the rail-pads are obtained by using soft pads, and the maximum reductions in terms of rail stresses (both on the foot and in the head) are obtained by using stiff pads.

Regarding the reduction levels, it can be noticed that they are typically higher in case of the speed equal to 80 km/h than in case of 40 km/h. This can be explained with the fact that increasing the speed leads to more severe impact forces and, therefore, to a bigger fluctuation between force levels in case of different pad stiffness.

It has been demonstrated in Appendix A how the indicators of the objective function have different trends and orders of magnitude and, therefore, it is not straightforward to combine them together. Thus, in this study only the indicator ballast pressure is considered. This assumption has been made since the ballast pressure is the main driver for settlement, which is the one that leads to the highest maintenance and renewal costs amongst the three considered (see Section 3.2.5.4).

An example of ballast pressure indicator is shown in Figure 3.2.48. The reference case is identified with a black marker.

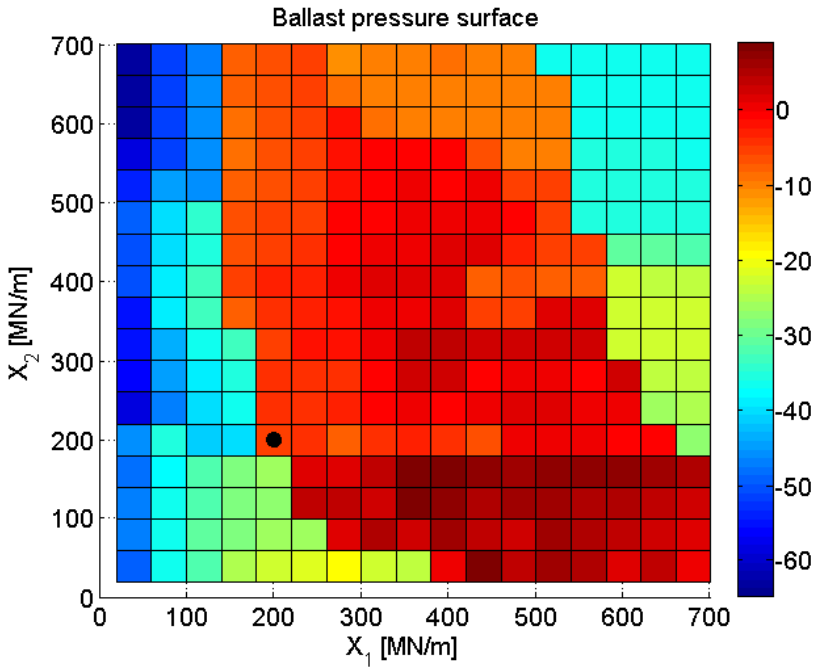

Figure 3.2.48. Ballast pressure indicator (speed = 80 km/h; K_{sup} = 150 MN/m^3). The reference case is identified with a squared black marker

3.2.5.5.2 Optimisation results

Considering medium quality support (150 MN/m^3), the optimisation algorithm has found the best solution in correspondence of rail-pad dynamic stiffness equal to 130 MN/m (Figure 3.2.49). This value refers to an equivalent 140 X 140 mm pad.

Figure 3.2.49 shows that choosing a soft rail-pad type can effectively help to smooth the overall stiffness along the crossing panel. Allowing for a maximum dynamic/static ratio of 1.3, the optimized stiffness corresponds to a static value of ca. 100 MN/m (soft category). This means that slightly stiffer pads than the ones currently used in the crossing panel should be implemented in case of medium quality support.

Note that the increase in the crossing inertia after the nose is due to the fact that the crossing used in the simulations is a Cast Centre Block (CCB) crossing.

Figure 3.2.50 shows the comparison between the nominal pad stiffness and the optimised pad stiffness in terms of contact forces, ballast forces, rail-pad forces, sleeper accelerations and bending stresses at the crossing nose and the rail displacement at the leg end. The percentage differences of the optimised case w.r.t. the nominal case are reported in Table 3.2.7.

Figure 3.2.50 and Table 3.2.7 show that there is a decrease in all the major indicators, including contact forces, ballast forces, rail-pad forces and sleeper acceleration. On the other hand, there is a slight increase in the bending stresses and a negligible increase in the displacement at the leg end.

Figure 3.2.51 shows the optimum pad stiffness for different support stiffness varying the line speed.

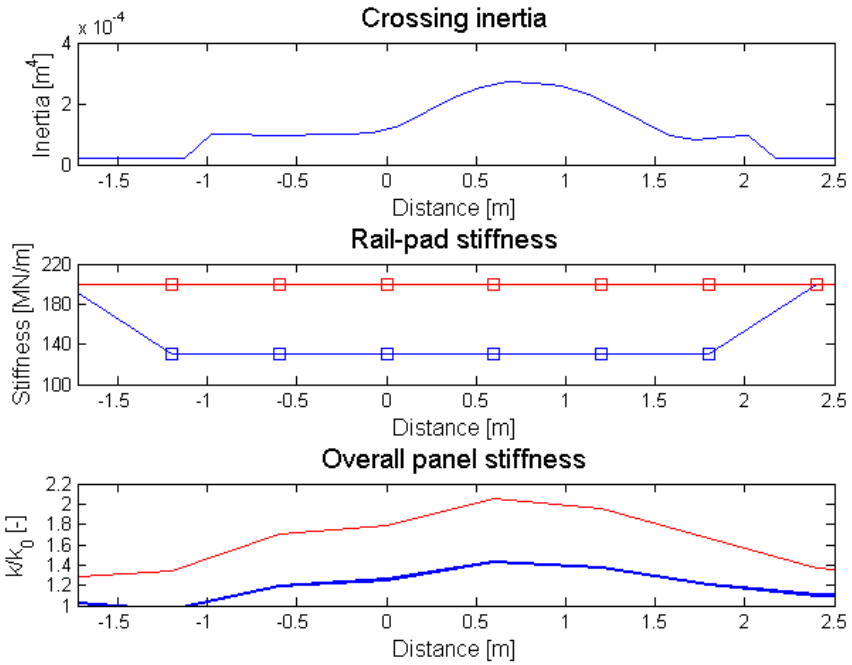

Figure 3.2.49. Overall normalised panel stiffness for the optimum solution (blue line) and the reference case (red line)

Table 3.2.7. Percentage differences of the optimised case w.r.t. the nominal case

Parameter	Differences
Contact force	-7% (P1); -3% (P2)
Ballast forces	-15%
Rail-pad forces	-10%
Sleeper acceleration	-12%
Bending stresses at the rail-foot	+4%
Displacement at the leg end	+2%

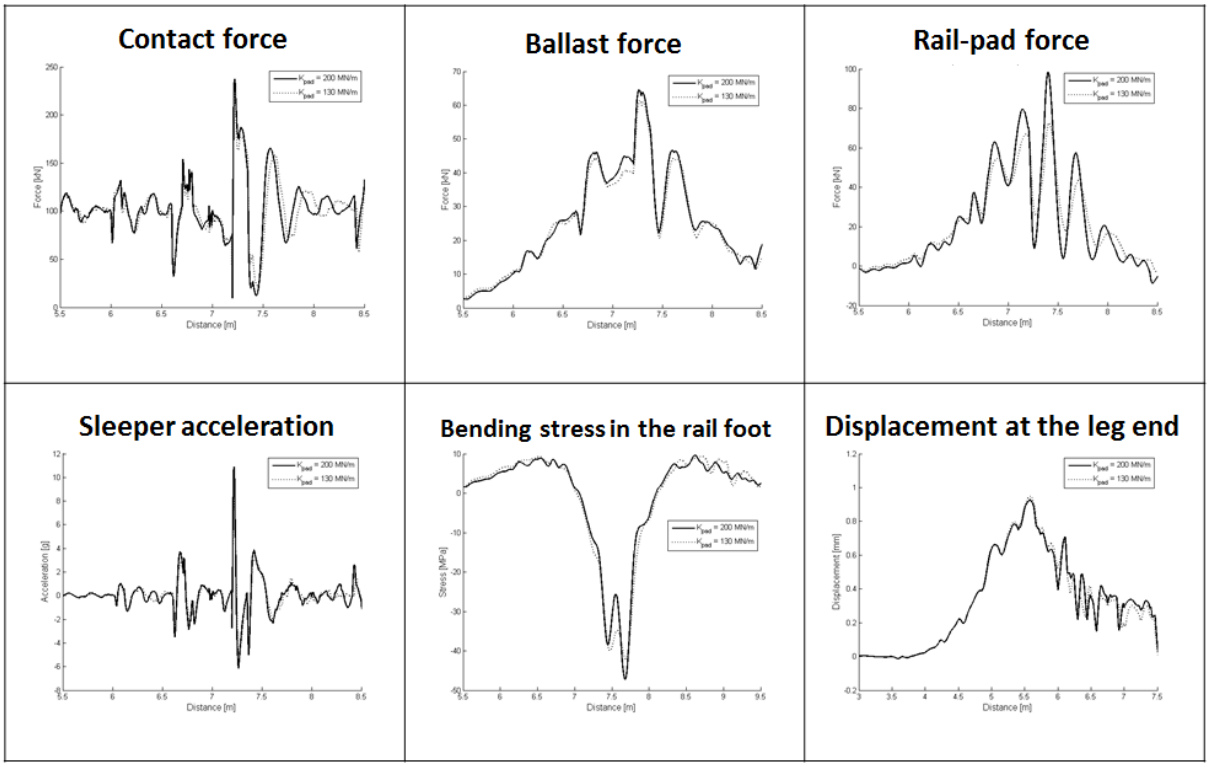

Figure 3.2.50. Comparison between the nominal pad stiffness (continuous line) and the optimum pad stiffness in terms of contact forces, ballast forces, rail-pad forces, sleeper accelerations and bending stresses (crossing nose) and rail displacement at the leg end

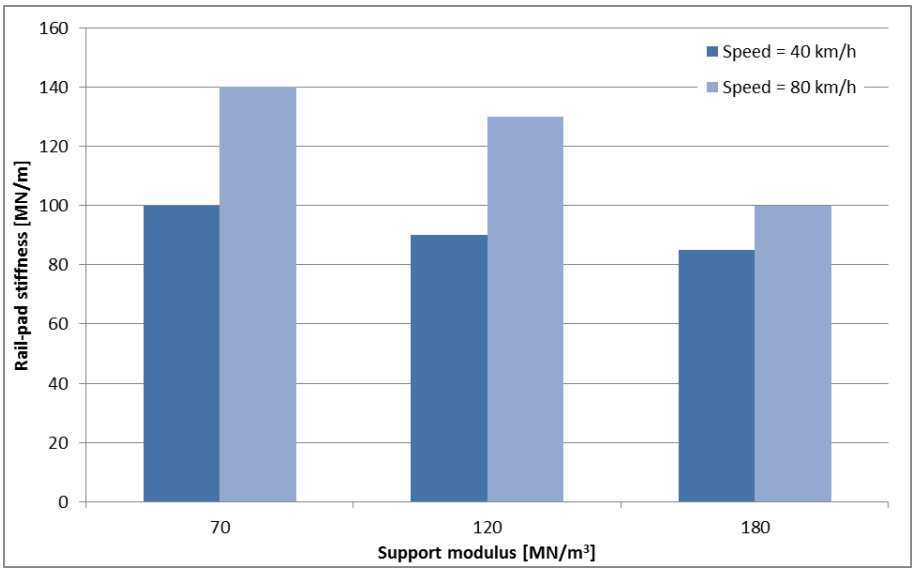

Figure 3.2.51. Optimum pad stiffness for different support stiffness varying the line speed

3.2.5.6 The effect of USPs

In this Section, the role of Under Sleeper Pads (USP) in track stiffness and dynamic quantities is investigated considering the case of medium support and speed equal to 80 km/h.

The methodology established in Section 3.2.5.4 is applied adding a second variable X_2 to represent the Under Sleeper Pad (USP) stiffness (Figure 3.2.52).

The range considered for the first variable X_1 is the same adopted in Section 3.2.5.4 and the range considered for the second variable X_2 is based on typical values for commercial soft, medium and hard pads from 40 to 120 MN/m (Ref. [3.2.36]) with a step of 10 MN/m.

The optimisation algorithm has found the best solution in correspondence of rail-pad dynamic stiffness equal to 130 MN/m, corresponding to soft pads, and USP dynamic stiffness equal to 80 MN/m, corresponding to medium USPs. This finding is in line with Ref. [3.2.37].

The optimised track stiffness along the crossing panel is shown in Figure 3.2.53.

Figure 3.2.53 demonstrates how the use of USPs can lead to reasonably continuous track stiffness all along the crossing panel, counterbalancing the effect of increased rail inertia. This fact may be beneficial to reduce drastically the formation of voids in the sleeper-ballast interface and, consequently, the differential settlement.

Nevertheless, it is necessary to check that the other dynamic quantities, including bending stresses and displacement at the leg end, change within a reasonable range (Figure 3.2.54 and Table 3.2.8).

Figure 3.2.54 and Table 3.2.8 show that using USPs it is possible to achieve further decreases in ballast forces and even more on ballast pressure. In fact, it is well known that the main advantage of USPs is to increase the contact area between sleeper and ballast by ca. 20-25% ([3.2.38]) thus acting as a protection layer. Nevertheless, there is a critical increase of stresses at the rail foot, which can cause transversal cracks in the casting reducing drastically the LCCs. Therefore, it is necessary to critically analyse the choice of using USPs in relation to each case considered and particularly the available ballast quality and stiffness.

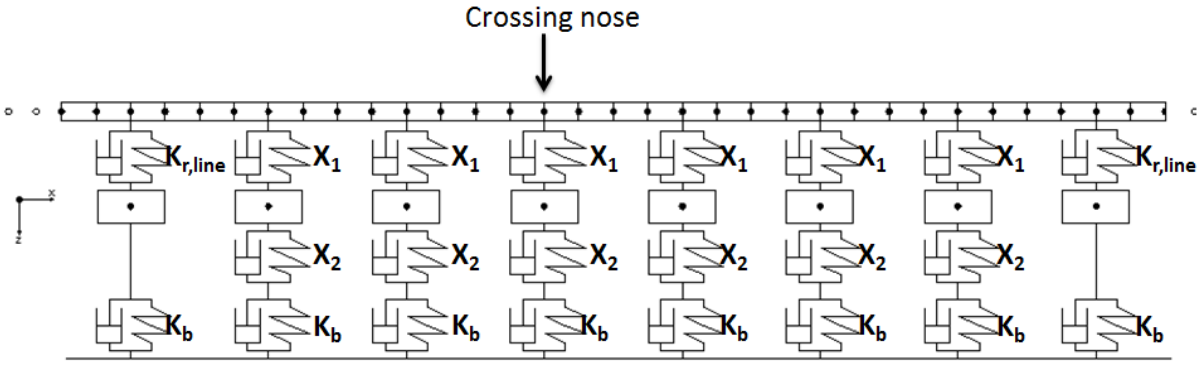

Figure 3.2.52. Optimisaion variables X_1 and X_2

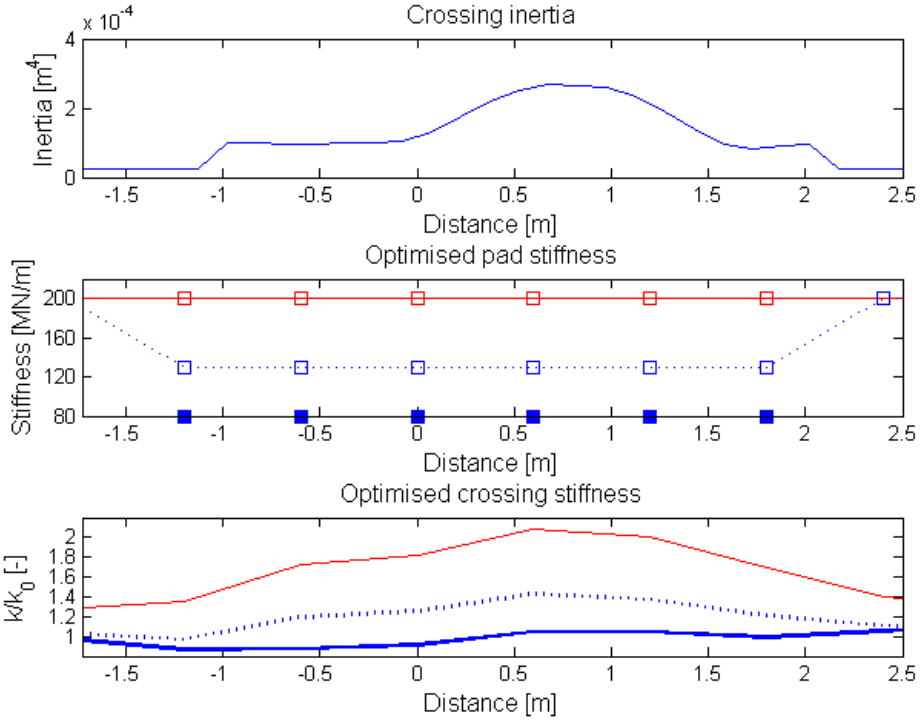

Figure 3.2.53. Overall normalised panel stiffness for the optimum solution with USP (blue continuous line), the optimum solution without USP (blue dotted line) and the reference case (red line)

Table 3.2.8. Percentage differences of the optimised case without and with USPs w.r.t. the nominal case

Parameter	Optimised without USPs	Optimised with USPs
Contact force	-7% (P1); -3% (P2)	-7% (P1); -15% (P2)
Ballast forces	-15%	-35%
Rail-pad forces	-10%	-6%
Sleeper acceleration	-12%	-4%
Bending stresses at the rail-foot	+4%	+15%
Displacement at the leg end	+2%	+4%

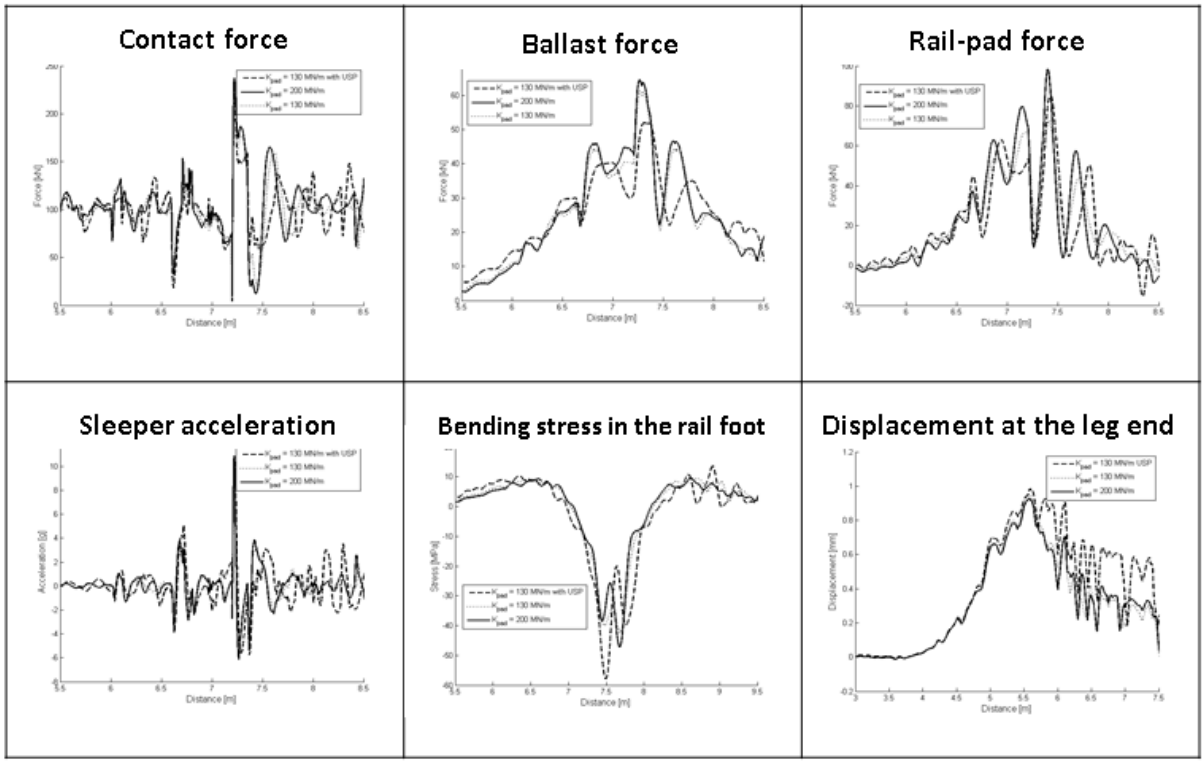

Figure 3.2.54. Comparison between the nominal pad stiffness (continuous line), the optimum pad stiffness (dotted line) and optimum pad stiffness with USPs (dashed line) in terms of contact forces, ballast forces, rail-pad forces, sleeper accelerations and bending stresses (crossing nose) and rail displacement at the leg end

3.2.6 OPTIMISATION OF SUPPORT STIFFNESS IN BALLASTED TRACK LINKING SLEEPER BEHAVIOUR

The previous Section demonstrated how it is possible to improve significantly the performances of a given crossing panel changing the rail pad characteristics. In order to achieve even better results, it is necessary to go in the direction of a uniform support as in ballastless track system. A medium-term solution has been proposed and consists in linking longitudinally the sleepers below the load transfer area in order to achieve a more continuously supported track system. Potential benefits may include reduction of sleeper vertical and lateral accelerations as well as forces transmitted to the ballast layer with potential reductions in differential settlement. Another beneficial effect may be a reduction in sleeper roll limiting uneven loading between the left and right side on turnout with wide bearers.

The practical details of how to implement such a solution are not discussed here and the work is intended to remain theoretical at this stage. It is however envisaged that this could be done rather simply by retro-engineering the desired properties at a low cost, so as to enhance ballasted S&C to behave more alike a slab track solution, without a complete renewal and associated costs.

Section 3.2.6.1 shows a pilot study to quantitatively assess potential benefits of the solution proposed.

3.2.6.1 Pilot study

3.2.6.1.1 Methodology

The vehicle/track interaction model used in this pilot study is shown in Figure 3.2.55.

Only vertical dynamic loads are considered in this initial study. The vertical irregularity input representing the vertical crossing geometry is calculated as explained in [3.2.39].

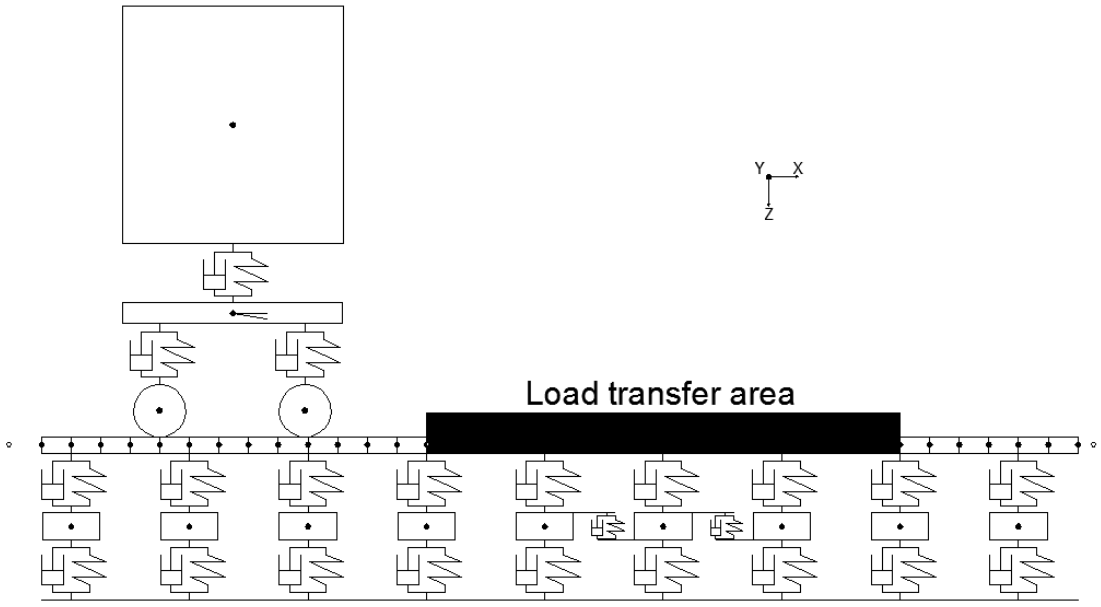

Figure 3.2.55. Two-dimensional vehicle/track interaction model with two longitudinal sleeper connections

The main parameter values adopted are as follows:

- *Crossing type*: CEN56 1 in 9.25 acute crossing;
- *Rail type*: 56E1 vertical profile;
- *Sleeper type*: concrete sleepers. The mass are variable between circa 410 kg and 470 kg as the length is not constant;
- *Support stiffness:* vertical stiffness equal to 80 MN/m (typical of medium support quality [3.2.40]).

The main vehicle data is:

- *Unsprung axle mass*: 1500 kg (typical of a freight wagon);
- *Axle load*: 20 t;
- *Primary linear suspension stiffness*: 13 MN/m**;**
- *Secondary linear suspension stiffness*: 6.2 MN/m**.**

Different conditions in terms of vehicle speed, number of links and longitudinal bar stiffness are considered, as following:

- *Vehicle speed*: 60/90/120/150 km/h;
- *Number of links*: 2/4;
- *Longitudinal bar stiffness*: 100/150/300/450 MN/m.

3.2.6.1.2 Early results

Figure 3.2.56 shows an example of the time history of ballast forces at the crossing panel for different longitudinal bar stiffness.

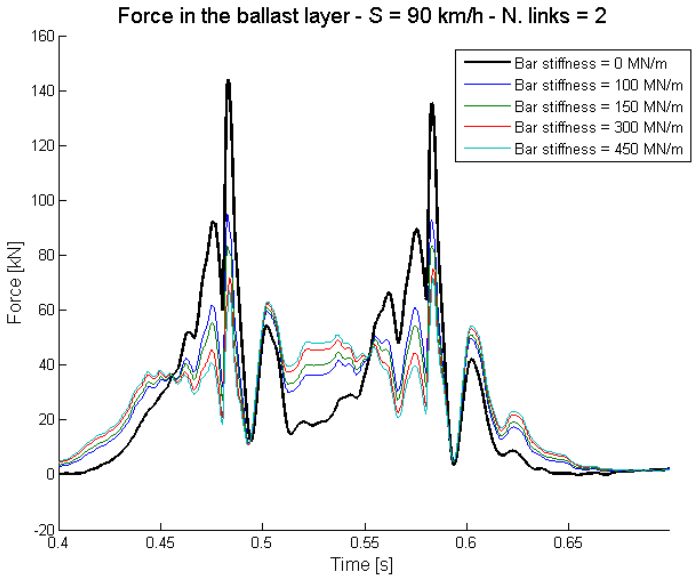

Figure 3.2.56. Ballast forces versus time (Speed = 90 km/h; number of links = 2)

Table 3.2.9. Percentage difference between the case considered and the baseline scenario (decreases are in blue and increases in red)

	2 links				4 links			
Output***Speed [km/h]**	***60***	***90***	***120***	***150***	***60***	***90***	***120***	***150***
Contact forces (average) **DECREASE**	0.6-1.2	2-4	2-5	5-7	2-4	5-10	8-15	8-18
Contact forces (maximum) **DECREASE**	10-15	9-18	5-14	12-17	10-20	11-16	15-21	15-20
Force in rail-pad (average) **INCREASE**	20-34	16-30	10-22	8-18	22-41	15-38	9-23	9-21
Force in rail-pad (maximum) **INCREASE**	45-80	41-67	40-60	39-72	45-85	40-80	40-75	40-80
Force in the support (average) **DECREASE**	30-50	32-53	32-53	32-53	32-61	34-63	36-68	35-66
Force in the support (maximum) **DECREASE**	40-66	37-61	39-61	39-58	51-88	41-72	46-76	45-74
Acceleration of sleeper (average) **DECREASE**	17-48	13-48	23-43	24-56	16-52	12-44	20-52	20-57
Acceleration of sleeper (maximum) **DECREASE**	39-90	43-90	50-90	60-89	37-95	41-94	42-90	40-96

From Figure 3.2.56, it is possible to conclude that the longitudinal connection between sleepers helps to lower the ballast forces, as expected. This diminution depends on the bar stiffness, with reduction from ca. 35% in case of low stiffness (100 MN/m) to ca. 50% in case of high stiffness (450 MN/m). Moreover, introducing a longitudinal connection between sleepers is beneficial to homogenise the ballast force levels across the area considered, similarly to slab track systems [3.2.41].

The percentage differences between the case considered and the baseline scenario are presented in Table 3.2.9 varying the travelling speed and the number of connections. The decreases are shown in blue and the increases in red.

The main conclusions that can be drawn from this pilot study are:

- *Contact forces*: the change in the contact forces is reasonably negligible in case of two links and in all the speed cases. Nevertheless, the maximum reduction starts becoming noteworthy with four links at the highest speeds considered (i.e. 120-150 km/h), reaching 15-20% decrease.
- *Forces in rail-pads*: generally speaking, in both cases considered there is an increase in the rail-pad forces. The increase is higher in case of low travelling speeds (60-90 km/h) as additional dynamic behaviour due to impact at crossing nose occurs at higher speed (120-150 km/h). Therefore, as stated previously, this mid-term solution requires further investigations for an adequate fastening system in order to avoid sleeper fatigue.
- *Force in the support*: a remarkable decrease of forces in the support appears when sleepers are connected longitudinally. As pointed in the previous Section, there is also a beneficial effect of homogenising the force level along the interested area, similarly to the slab track concept. The effect of speed is almost negligible.
- *Sleeper acceleration*: in addition to decreases of forces in the support, further noteworthy decreases in sleeper accelerations are found with increasing speed.

The last two quantities considered (force in the ballast and sleeper acceleration) are generally recognised as the main drivers of the ballast settlement. Therefore, the proposed solution may be

beneficial to help preventing differential settlement, geometry degradation, void generation and casting fatigue, and therefore a mitigation measure could be envisage on a case by cases basis to react against these specific problems.

As further work, it is necessary to explore the implication of lateral dynamics benefits and combined lateral/vertical using a three-dimensional model as the one described in Section 3.2.5.4.

3.2.7 MATERIAL CONSIDERATION

3.2.7.1 New material

It is widely accepted that fixed point crossings are one of the most sensitive components of a switch and crossing (S&C) layout. The crossing is exposed not only to rolling contact, but also to dynamic high energy shocks during the transfer of the wheel from the crossing nose to wing rail or vice-versa.

A significant proportion of S&C for railway systems are currently manufactured from cast austenitic-manganese steel (AMS). AMS has traditionally been used owing to its good resistance to abrasion, high work hardening capacity on impact and excellent toughness following solution treatment and water quenching. The primary reason is the rapid work hardening rate that results in high hardness and the associated increase in resistance to wear. Without the rapid work hardening, resistance to abrasion, wear, and plastic deformation of AMS is poor. The nominal chemical analysis of AMS is 1.2% C, 13% Mn, 0.5% Si, which produces bulk hardness in the region of 200 to 250 HB. Following the passage of several MGT of traffic AMS S&C can reach hardness levels of 500 to 550 HB. However, there are a number of drawbacks with the use of AMS, which has prompted S&C suppliers to explore the use of alternative materials. Furthermore, AMS relies on work hardening to achieve optimum resistance to wear. Time taken to reach optimum hardness depends on axle load and for light rail applications the time to reach optimum hardness is inevitably considerably longer than that for heavy axle load applications. An alternative solution consists in pre-hardening the frog through explosion; this solution however means extra costs.

The low 0.2% yield stress (typically in the range 300-400 N/mm2) can sometimes be a disadvantage in service as the deformation due to impact commonly experienced in railway switches and crossings increases the proof strength to levels more resistant to plastic flow but the associated dimensional changes are undesirable. Where work hardening is slow the AMS requires frequent weld repairs to restore deformation height loss as evidenced in Deliverable D13.1 “Operational Failure modes of S&C” *(**1.4.3** plastic deformation of the crossing nose for fixed crossings and **1.4.12** spalling of crossings)*

AMS is not an easy material to cast or machine into complex shapes needed for switches and crossings. The narrow freezing range of AMS results in many cavity type defects. Casting defects are

common and are often the starting point of cracking seen in service. The presence of sub-surface casting cavities also increases the difficulty of weld restoration. Thus, the presence of such cavities restricts the permissible magnitude of vertical wear. This has been clearly demonstrated with the AMS points/crossings installed where the severe casting defects have resulted in cracking appearing on the running surface necessitating weld repair *(Deliverables D13.1* ***section 1.4.4*** *casting defect leading to cracking and* ***1.4.5*** *transverse crack on the crossing nose)*. After approximately 10 years service the extent of the defects has become so severe that it has become uneconomical to continue remedial weld repair and the crossings have had to be replaced.

A further problem with AMS is the thermal instability of the austenitic structure, which renders it difficult to weld repair in track should material break-outs occur (as evidenced by *Deliverable D13.1* ***section 1.4.10*** *material break-outs on manganese crossings)*. Another major disadvantage of AMS crossings is that they cannot be inspected by ultrasonic or eddy current techniques.

The direct weld connection between manganese crossings and carbon steel rails cannot be carried out with the usual welding processes (e.g., thermit welding, shielded manual arc welding, etc.) nor directly with processes such as flash-butt welding, This is due to the metallurgical incompatibility of the two steels. The crossing to rail connection is made possible by using a stainless steel insert that is flash-butt welded, first to the frog and then to the carbon-steel rail, thus minimising the incompatible mechanical discontinuity between the parts to be connected. However this process of double welding while superior to bolted fishplated joints, can, if not carried out correctly lead to failures in track or can lead to a 'soft-spot' around the adaptor casting being created. (*Deliverable D13.1* ***section 1.1.3)***

The proposed answer to the defects identified in *Deliverable D13.1 "Operational Failure modes of S&C"* (described above) is to limit the initiation of such defects through the use of a special steel that provides a higher surface hardness.

The new material and its implememtation developed by Vossloh Cogifer is different than existing steel grades (e.g. CrBainit [DB], B320, B360) and will offer significant benefits over traditional cast manganese crossings in terms of improved internal quality and the resulting extension to component life at the same time as reduced maintenance cost.

The target of the demonstrator is to confirm the effects that can indeed be avoided through the use of the proposed new material, and to quantify the resulting decrease in whole life costs.

In principle the Demonstrator would take the form of a crossing manufactured in the new steel that would replace an existing 60E1 crossing (Turnout TG 1/12 R500mm) manufactured from cast manganese.

The crossing would have the same geometry as the existing crossing and would match the existing crossing footprint with only 8 special replacement baseplates requiring to be provided.

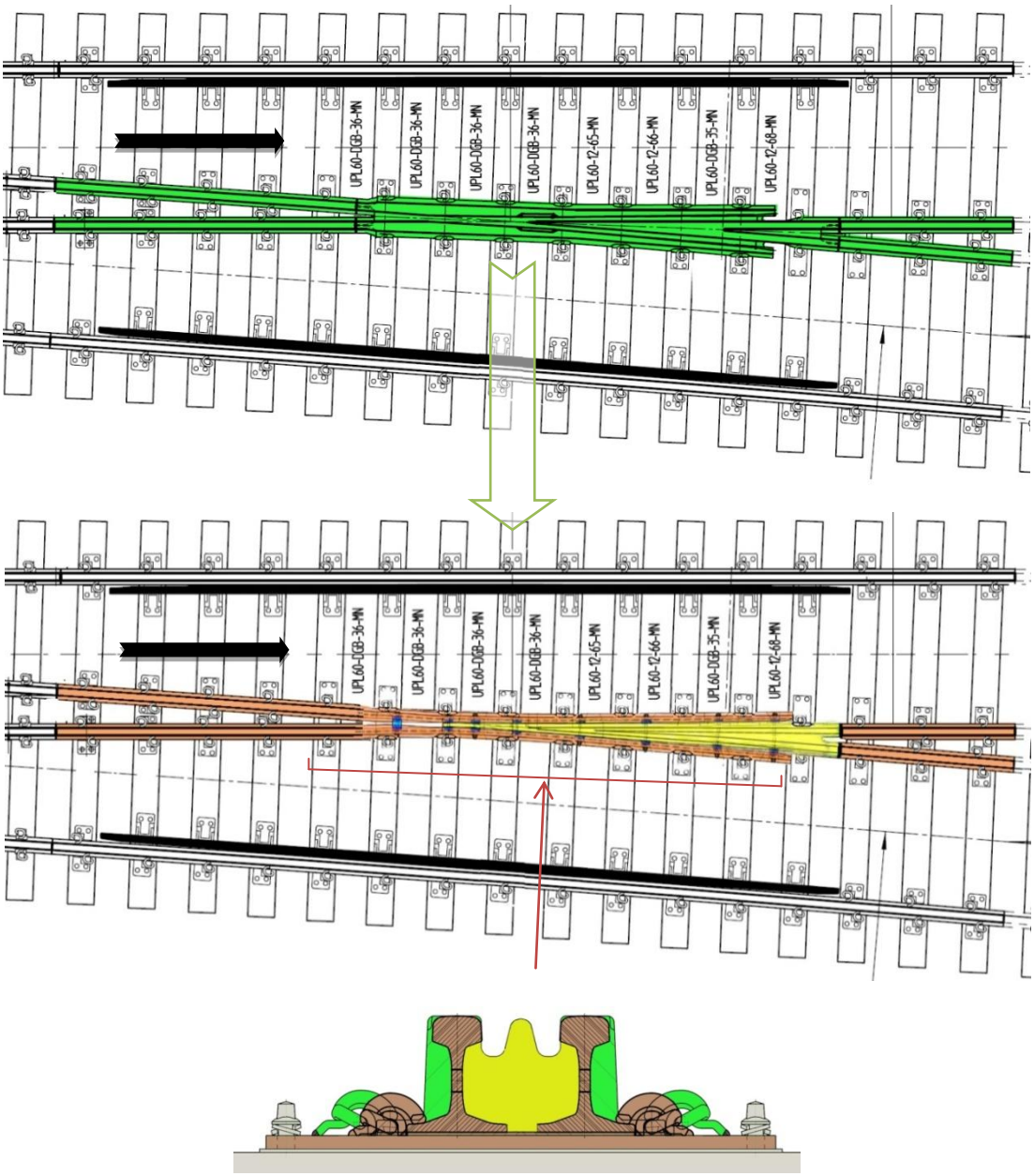

Figure 3.2.57. Demonstrator crossing. Same geometry and compatible baseplates (8 special provided with the test crossing). Tested material is implemented on the crossing point and represented in yellow on the drawing. The green section represents the monobloc Mn crossing shape replaced by the rails and point. The fasteners (Pandrol clip) are moved in order to be close to the rail. The baseplate has same holes as for Mn crossing, but adapted shoulders

3.2.7.2 Crossing geometry and wear monitoring in track

Understanding the complex degradation mechanisms of wear, plastic deformation and fatigue damage in crossing and switches requires robust damage models supported by reliable material data as well as a mean of precisely measuring and quantifying the change in shape of the rails under traffic conditions.

Current industry practice relies on manual devices such as MiniProf and Calipri to do this. However surveying a full turnout at regular intervals implies costly operation with long track possession, often at night where quality of data can be compromised by a number of factors, most importantly the human factor.

Various semi-automated advanced solutions are available using a range of 3D or 3D laser scanner or 3D camera. The C4R consortium is interested in investigating those solutions able to improve the speed and reliability of track measurement to support the validation of models prediction as well as validate any demonstrator activities.

UoH in a H2020 project on weld is developing a laser based system to measure weld. It is currently working automatically on a frame fixed to the running rail, while a length of about 1 m around the weld is scanned automatically in several seconds (series of 2D cross sections measured every .1 mm), see Figure 3.2.58. UoH plans to adapt this low cost system to a lightweight S&C frame to trial on crossings. Similar system has been found such as GRAW scorpion which are however not so easily transportable, see Figure 3.2.59.

Figure 3.2.58. UoH Laser measurement on welded leg end

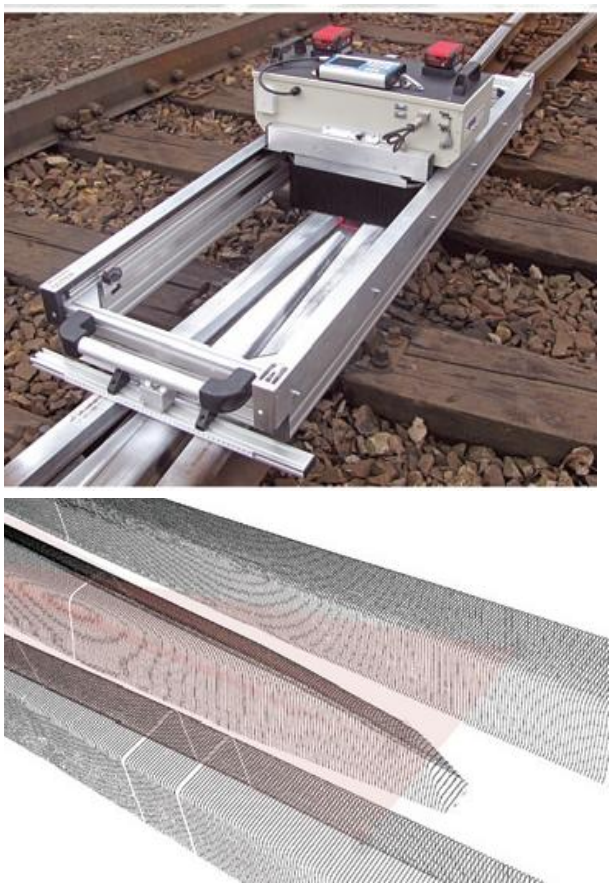

Figure 3.2.59. Graw Scorpion S&C measurement system (source http://graw.com)

Vossloh Cogifer plans to do the demonstrator follow up in track in order to measure the new material behaviour.

The aim is to measure the running surface before traffic, after 1 month, 6 months, 12 month,s 24 months. Those measurements compared to the reference shape will show the wear at relevant sections and wear along the crossing point.

The measurement will be done with a portable laser tool “creaform HANDY SCAN3D –700”. Resolution is 0.05 mm and accuracy 0.03 mm.

VCSA has tested this tool and plan to buy this tool, see the CAD snapshot in Figure 3.2.61.

Figure 3.2.60. Portable 3D scanner by HandyScan 3D (source: http://www.creaform3d.com)

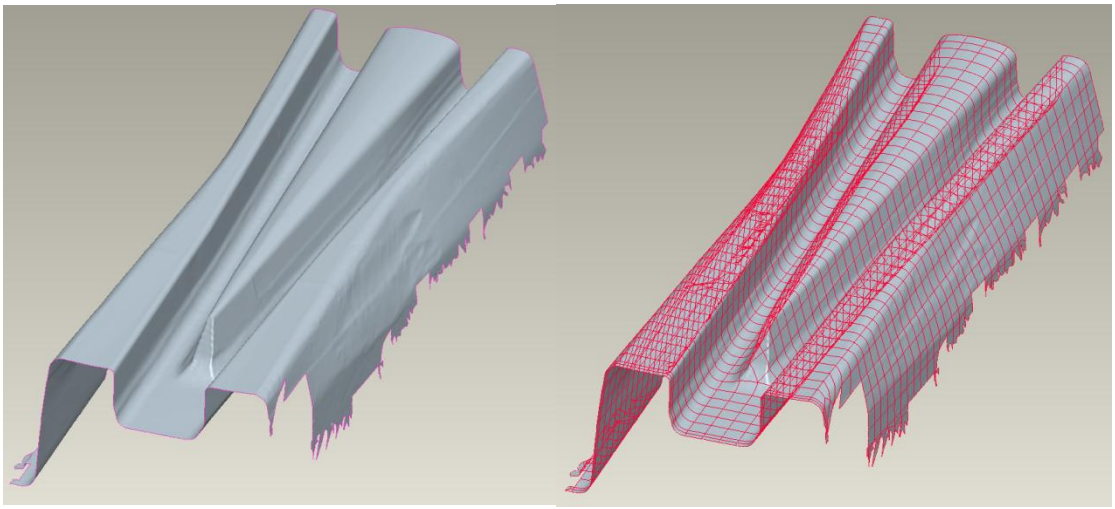

Figure 3.2.61. Meshed STEP model

3.2.8 REFERENCES

[3.2.1] C4R Deliverable 1.3.1

[3.2.2] SUSTRAIL Deliverable 4.4

[3.2.3] Jenkins, H., Stephenson, J., Clayton, G., Morland, G., & Lyon, D., The effect of track and vehicle parameters on wheel/rail vertical dynamic forces, *Railway Engineering Journal*, 1974, **3**(1), pp 2-16

[3.2.4] Innotrack Deliverable 3.1.4

[3.2.5] Pålsson, B. A., & Nielsen, J. C., Track gauge optimisation of railway switches using a genetic algorithm, *Vehicle System Dynamics*, 2012, **50**(Sup1), pp 365-387

[3.2.6] Wan, C., Markine, V., & Shevtsov, I., Improvement of vehicle–turnout interaction by optimising the shape of crossing nose, *Vehicle System Dynamics*, 2014, **52**(11), pp 1517-

1540

[3.2.7] Andersson, C. and T. Dahlberg, Wheel/rail impacts at a railway turnout crossing, *Proceedings IMechE, Part F, Journal of Rail and Rapid Transit*, 1998, 212(2), pp 123-134

[3.2.8] Zhu, J.Y., On the effect of varying stiffness under the switch rail on the wheel—rail dynamic characteristics of a high-speed turnout, *Proceedings IMechE, Part F, Journal of Rail and Rapid Transit*, 2006, **220**(1), pp 69-75

[3.2.9] Kassa, E., C. Andersson, and J.C. Nielsen, Simulation of dynamic interaction between train and railway turnout, *Vehicle System Dynamics*, 2006, **44**(3), pp 247-258

[3.2.10] Alfi, S. and S. Bruni, Mathematical modelling of train–turnout interaction, Vehicle System Dynamics, 2009, **47**(5), pp 551-574

[3.2.11] Bruni, S., et al., Effects of train impacts on urban turnouts: modelling and validation through measurements, *Journal of Sound and Vibration*, 2009, **324**(3), pp 666-689

[3.2.12] Ren, Z., S. Sun, and G. Xie, A method to determine the two-point contact zone and transfer of wheel–rail forces in a turnout, *Vehicle System Dynamics*, 2010, **48**(10), pp 1115-1133

[3.2.13] Burgelman, N., Z. Li, and R. Dollevoet, A new rolling contact method applied to conformal contact and the train–turnout interaction, *Wear*, 2014, **321**, pp 94-105

[3.2.14] Sebes, M., et al., Application of a semi-Hertzian method to the simulation of vehicles in high-speed switches, *Vehicle System Dynamics*, 2006, **44**(sup1), pp 341-348

[3.2.15] Wiest, M., et al., Assessment of methods for calculating contact pressure in wheel-rail/switch contact, *Wear*, 2008, **265**(9), pp 1439-1445

[3.2.16] Pletz, M., W. Daves, and H. Ossberger, A wheel passing a crossing nose: Dynamic analysis under high axle loads using finite element modelling, *Proceedings IMechE, Part F, Journal of Rail and Rapid Transit*, 2012, **226**(6), pp 603-609

[3.2.17] Wiest, M., et al., Deformation and damage of a crossing nose due to wheel passages, *Wear*, 2008, **265**(9), pp 1431-1438

[3.2.18] Kassa, E. and G. Johansson, Simulation of train–turnout interaction and plastic deformation of rail profiles, *Vehicle System Dynamics*, 2006, **44**(Sup1), pp 349-359

[3.2.19] Pletz, M., W. Daves, and H. Ossberger, A wheel set/crossing model regarding impact, sliding and deformation—Explicit finite element approach, *Wear*, 2012, **294**, pp 446-456

[3.2.20] Sun, Y.Q., C. Cole, and P. Boyd, A numerical method using VAMPIRE modelling for prediction of turnout curve wheel–rail wear, *Wear*, 2011, **271**(1), pp 482-491

[3.2.21] Johansson, A., et al., Simulation of wheel–rail contact and damage in switches & crossings, *Wear*, 2011, **271**(1), pp 472-481

[3.2.22] Xiao, J., F. Zhang, and L. Qian, Contact stress and residual stress in the nose rail of a high manganese steel crossing due to wheel contact loading, *Fatigue Fract Engng Mater Struct*, 2014, **37**(2), pp 219-226

[3.2.23] Ekberg, A., E. Kabo, and H. Andersson, An engineering model for prediction of rolling contact fatigue of railway wheels, *Fatigue Fract Engng Mater Struct*, 2002, **25**(10), pp 899-909

[3.2.24] Vu, M., S. Kaewunruen, and M. Attard, Nonlinear 3D finite element modeling for structural failure analysis of concrete sleepers/bearers at an urban turnout diamond, 2016

[3.2.25] Eck, S., et al., Comparison of the fatigue and impact fracture behaviour of five different steel grades used in the frog of a turnout, *Proceedings IMechE, Part F, Journal of Rail and Rapid Transit*, 2014, **228**(6), pp 603-610

[3.2.26] Larsson-Kraik, P.-O., et al., Geometrical degradation of railway turnouts-a case study from Swedish heavy haul railroad, *Proceedings IMechE, Part F, Journal of Rail and Rapid Transit*, 2014, **228**(6), pp 611-619

[3.2.27] Li, X., J.C. Nielsen, and B.A. Pålsson, Simulation of track settlement in railway turnouts. *Vehicle System Dynamics*, 2014, **52**(Sup1), pp 421-439

[3.2.28] Kennedy, J., et al., Reducing railway track settlement using three-dimensional polyurethane polymer reinforcement of the ballast, *Construction and Building Materials*, 2013, **44**, pp 615-625

[3.2.29] SOLIDWORKS. Release 2015. Dassault Systèmes

[3.2.30] ANSYS Mechanical APDL. Release 15.0. ANSYS Inc.

[3.2.31] ANSYS Mechanical APDL. Release 15.0, Help system, ANSYS parametric design language guide. ANSYS Inc.

[3.2.32] Nicklisch, D., Kassa, E., Nielsen, J., Ekh, M., & Iwnicki, S., Geometry and stiffness optimization for switches and crossings, and simulation of material degradation. *Proceedings IMechE, Part F, Journal of Rail and Rapid Transit,*2010, **224**(4), pp 279-292.

[3.2.33] Lichtberger, B., Track compendium. Eurailpress Tetzlaff-Hestra GmbH & Co. KG, Hamburg, 2005

[3.2.34] Grossoni, I., Bezin, Y., & Neves, S. G. M., Optimization of support stiffness at a railway crossing panel. Paper presented at the Railways 2016, The Third International Conference on Railway Technology: Research, Development and Maintenance, Cagliari Italy

[3.2.35] Kaewunruen, S., & Remennikov, A. M., Sensitivity analysis of free vibration characteristics of an in situ railway concrete sleeper to variations of rail pad parameters, *Journal of Sound and Vibration*, 2006, **298**(1), pp 453-461

[3.2.36] Johansson, A., Nielsen, J. C.O., Bolmsvik, R., Karlström, A., & Lundén, R., Under sleeper pads—Influence on dynamic train–track interaction, *Wear*, 2008, **265**(9), pp 1479-1487

[3.2.37] du Grand Placitre, A., & Zuckerman, A., Benefits of Under Sleeper Pads (USPs) for ballasted track. Paper presented at the RAILWAY ENGINEERING 2015: 13th International Conference & Exhibition, Edinburgh, 2015

[3.2.38] Riessberger, A., Ballast track for high speeds. Proceedings "Tracks for High-Speed Railways", pp 23-44, Porto, Portugal, October 2006

[3.2.39] Grossoni, I., Bezin, Y., & Alonso, A., Modelling Uneven Support at Railway Crossings using a Vehicle-track Coupling System. in J. Pombo (Editor), Railways 2014, Ajaccio, Corsica, 2014

[3.2.40] Hunt, G.A., EUROBALT: vertical dynamic model for track damage studies. British Rail Research: Derby, 1998

[3.2.41] Bezin, Y., Farrington, D., Penny, C., Temple, B., & Iwnicki, S., The dynamic response of slab track constructions and their benefit with respect to conventional ballasted track, *Vehicle System Dynamics*, 2010, **48**(Sup1), pp 175-193

3.3 LONG-TERM DESIGN SOLUTIONS

The overall design of the S&C has been fundamentally unchanged for the last 30 years. To tackle the significant increases in line speed, axle load and volume of traffic the S&C system has been incrementally further developed, but from a sub-system or component level. The future ambition of the S&C next generation is therefore to consider a whole-system approach to enhancing common S&C designs and to incorporate modern mechatronics for improved system kinematics and control.

Sections 3.3.1 – 3.3.4 have been written by VAE, while Section 3.3.5 has been written by VCSA.

3.3.1 S&C NEXT GENERATION – ENHANCED DESIGN, MATERIALS & COMPONENTS

Due to higher traffic loads, higher speeds and severe weather conditions and dirt, S&C components are affected by slip, wear and rolling contact fatigue. S&C rely on standard profiles that are machined to the specific shapes as required by the S&C configuration. Traditionally, the design application engineering is different across European and particularly worldwide railways. To progress beyond the current state of the art technology transfer opportunities from other industries as well as developing materials science solutions shall be examined. The innovative approach is to adopt the growing trend of merging mechanical, electro-mechanics, electronic design and digital control system elements into one integrated S&C. The next generation of radical S&C designs will be based on new methodologies of switching trains between tracks in a manner that improves capacity, performance and reduce costs whilst maintaining safety as the most important consideration. The wheel-rail interface will be optimised to enable the development of radically new mechanisms for switching a train from one line to another.

3.3.2 S&C NEXT GENERATION – ENHANCED KINEMATIC & ELECTRIFICATION SYSTEMS

Existing S&C systems still use historical design feature originally intended for hand operation. Modern actuators and motors deliver increased switch actuation forces, which can reduce the asset operational life. The next generation of S&C design will incorporate a completely new switching function using novel kinematic elements and will be designed from a whole system perspective. The new design will also affect the failure modes of track circuits and provides an opportunity to integrate train detection with significantly reduced electrical failure modes.

3.3.3 S&C Next Generation – Enhanced Control, Monitoring & Sensor Systems

Existing S&C systems do not utilise sophisticated sensor systems with feedback control loops. Through new technology development and transfer from other industries, the next generation S&C design will incorporate intelligent self-diagnostic systems with the capability to self-adjust, self-correct and self-heal within predefined system operating tolerances. The next generation of S&C will significantly reduce manual maintenance operations through self-management.

3.3.4 S&C Next Generation – Maintenance and Degradation Free S&C

It is vital that the S&C system has a stable position in vertical and lateral direction during its operational life time. To counter the dynamic forces over the total life time correct support conditions have to be guaranteed. It is common that the S&C is treated as an extension of the normal plain track system utilising the same design and construction techniques. The next generation of S&C will allow for a different approach to the S&C support elements and will be designed together as a whole system.

3.3.5 MCS Modular Continuous Support on turnout design

Modular Continuous Support (MCS) track developed by Vossloh Cogifer is a ballast-less beam track offering an efficient lower cost rail technology for all track configurations (including for turnouts) based on two main principles:

- Pre-fabricated modules for tracks and turnouts (a small gap appears between the modules, but with limited influence on the performance).
- Rail is continuously supported.

MCS track is a way to improve track design and S&C design in the following fields, see also Table 3.3.1:

- Reduced structure height and weight, facilitating the logistics.
- Maintenance costs amount to 20-30% of the maintenance costs for ballasted track.
- Increased service life, improved rail behaviour in track and turnouts
- Higher track stability
- Abatement of noise and, in particular, vibration nuisance
- Track accessibility to road vehicles

Table 3.3.1. MCS track vs ballasted track

DESCRIPTION	Ballast track	MCS track
Maintenance	Need to check and upkeep geometry, high cost.	Stable geometry. Low cost, comparable to slab track.
Construction cost and LCC	Construction cost relatively lower but with high LCC	Construction cost comparable to ballast track, but with LCC comparable slab track.
Construction	Need for heavy, specialized machinery	No specific equipment for a modular layout.
Lifetime	Relatively lower.	Relatively higher: comparable to slab track.
Rail and turnout design	Wear, vibration and contact surface driven by sleepers layout	Better setting of the rail which implies less wear, vibration and a better stability. Les constraints on the rail.
Stability	Instability of the track on ballast	Comparable to slab track

MCS track technology includes the following features (cf. Figure 3.3.1):

- Longitudinal pre-cast reinforced concrete beams, continuously supporting the rail by a continuous pad. Beams can be designed for any capacity.
- Standard proprietary fastenings are used to fix rails on the beams with a spacing potentially longer than for ballasted track.
- The modular design system is delivered in convenient 5 to 8 m track modules consisting in the assembly of the two concrete beams connected together to ease and ensure alignment. Modules can be easily shipped by truck or rail.
- The absence of ballast implies a direct contact between the longitudinal beam and the platform through a certain thickness of grout.

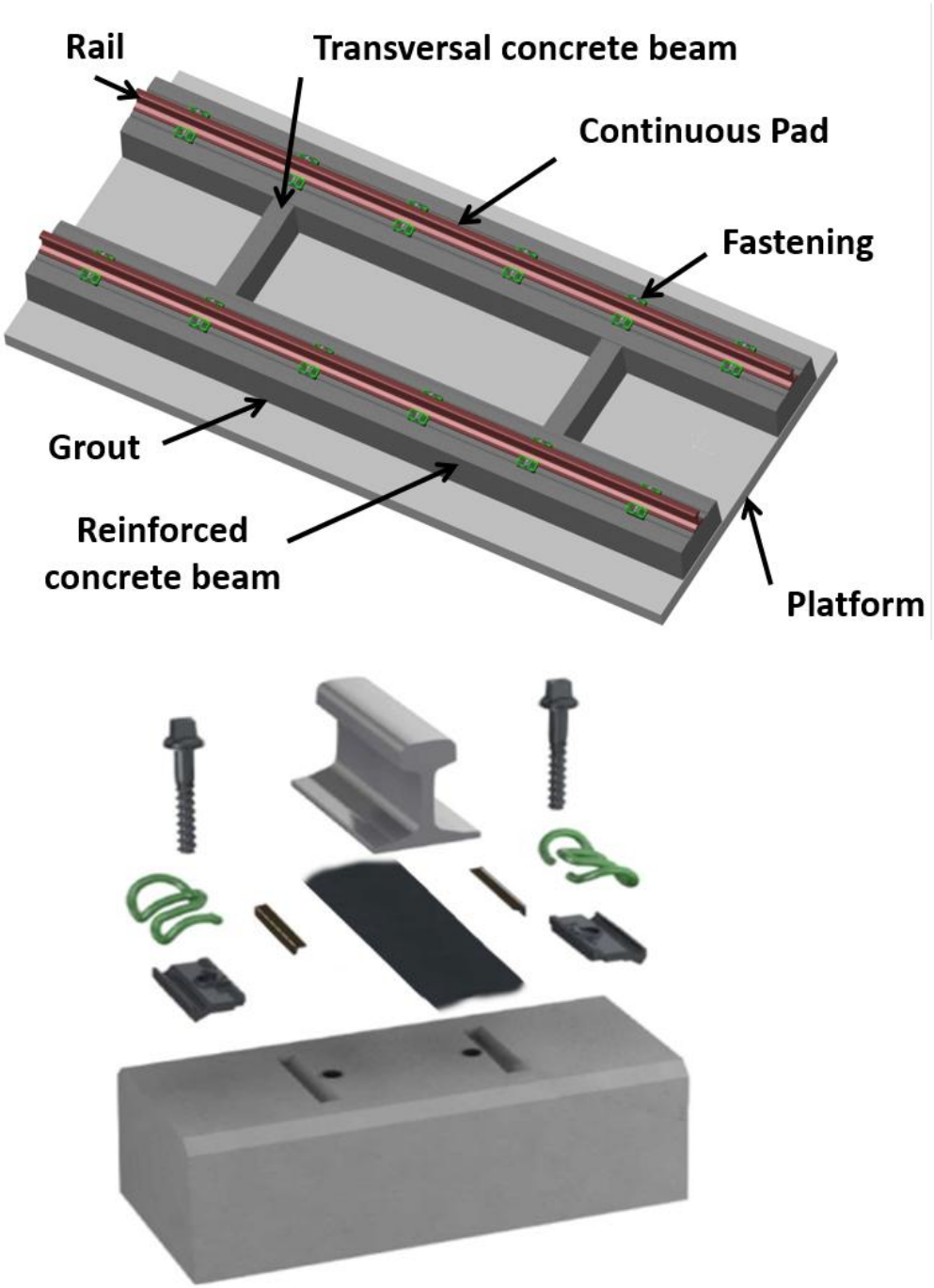

Figure 3.3.1. Modular Continuous Support description

Figure 3.3.1 shows a track module by Vossloh Cogifer with MCS principles developed at WP1.1 slab track workshops:

- A continuous elastic pad is supporting the rail.
- Six fastening systems are located on each beam.
- The distance between fasteners is around 1000 mm (R>3000 m), and 600-700 mm (R<3000 m).
- Vossloh W21T fastening system is used.
- Lateral adjustment is done by an adapted angle guide or insulator (+/-4mm).
- Curve is included in the concrete bloc (location of dowels and grove).
- Rail inclination is included in the concrete bloc section or rail head.
- TOP DOWN levelling is used: a mortar is applied between the module and the bituminous layer or sub layer.

Mechanically, it can be pointed out that MCS track is supposed to exhibit a better LWR resistance compared to conventional track (reduced rail warp risk when confronted to extreme temperatures).

3.3.6 MCS APPLICATION IN S&C

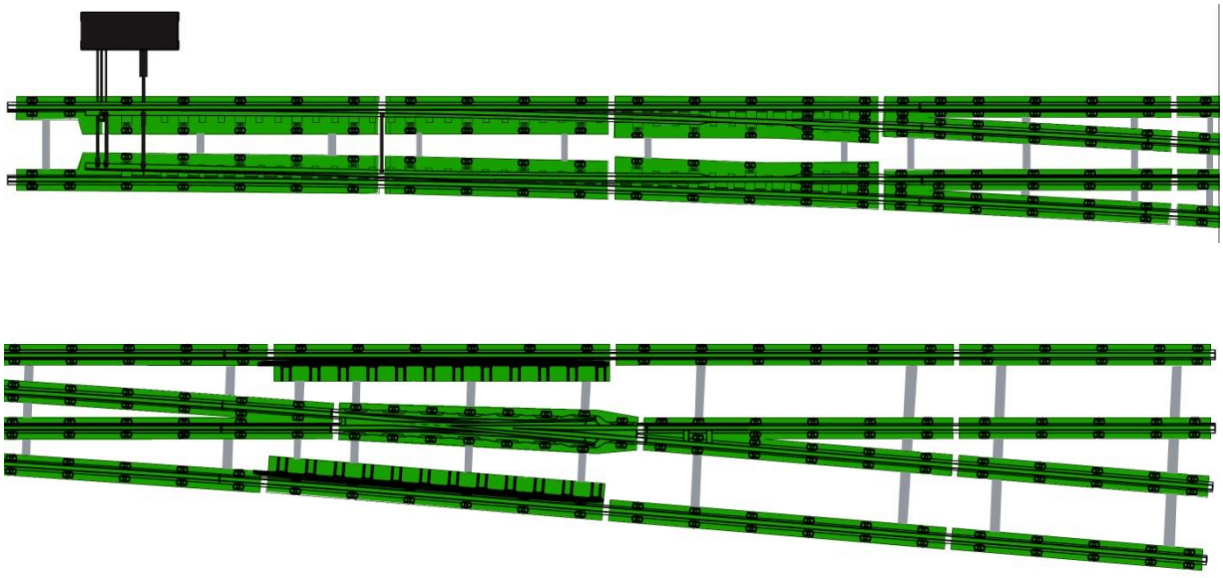

Figure 3.3.2. Modules (MCS)

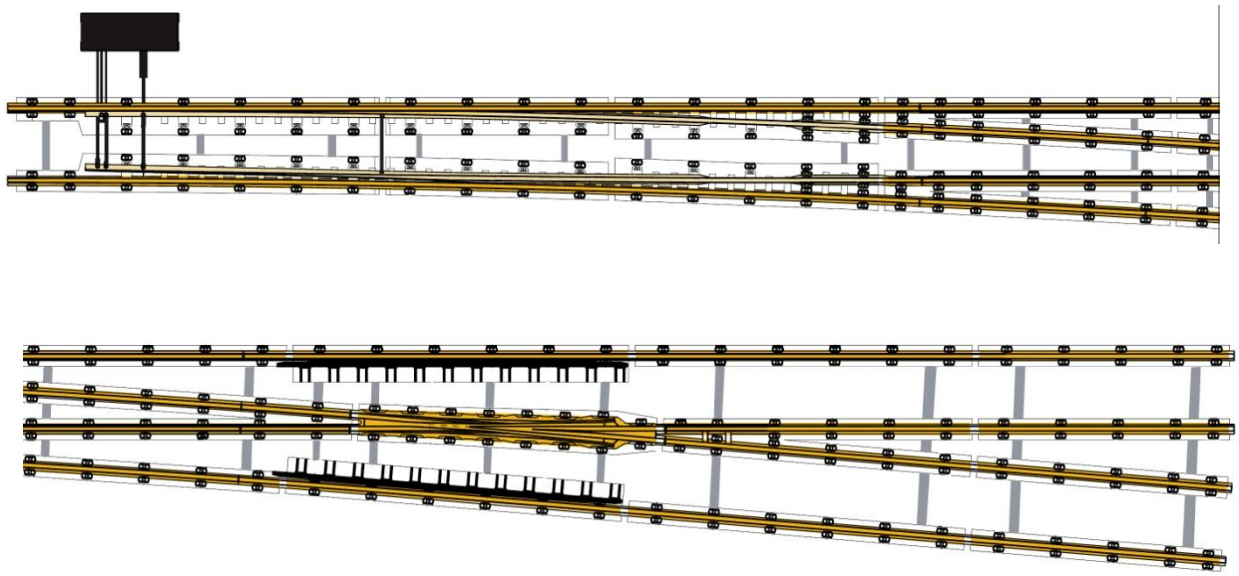

Figure 3.3.3. Continuous rail support (MCS)

4 S&C resilience to extreme weather conditions (C4R task 1.3.3)

4.1 COLD CLIMATE

4.1.1 BACKGROUND

Snow and low temperature are meteorological phenomena that affect the reliability of the railway. As precipitation seems to increase in certain places in the scenario of warmer climate it might also become more frequent with extreme snowfalls in the future[2]. Track problems related to cold climate and potential solutions are discussed in Section 4.1, which has been written by Trafikverket.

4.1.2 TEMPERATURE AND SNOW IN EUROPE

Temperatures below zero are possible in all of Europe but are more common in the north and at high altitudes, such as in the Alps. The lowest temperatures are normally recorded in January and February, and large amounts of snow are obtained if the cold weather is combined with open water. In Figure 4.1.1, it is shown that this can affect nearly all of Europe. In many European countries, only a few days in a year lead to problems for the railways and therefore the preparedness for snow and ice is less than it is for countries having temperature below zero up to 120 days per year (northern Europe). The amount of snow varies from a few centimetres up to 200 centimetres per year. According to SMHI (the Swedish Meteorological and Hydrological Institute), snowfall can result in up to 100 centimetres in just one day. It is the combination of strong winds and snow fall that gives the largest problems.

[2] IPCC https://www.ipcc.ch/pdf/reports-nonUN-translations/swedish/ar5-wg2-spm.pdf

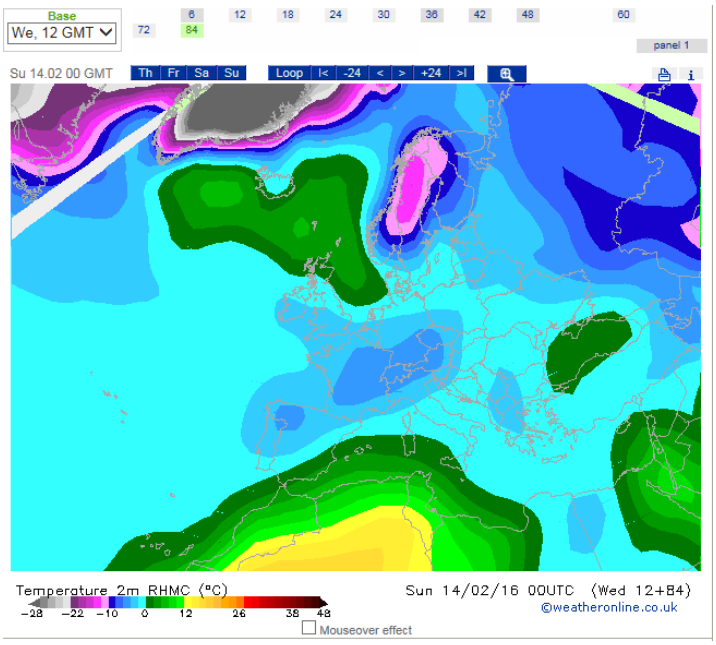

Figure 4.1.1. Night temperature 14th February 2016 (source www.weatheronline.co.uk)

4.1.3 TRACK RELATED PROBLEMS

There is a higher number of failures during the winter as shown in Figure 4.1.2. These failures are typically for rail, S&Cs and overhead wire (or 3rd rail). Those that affect traffic are for instance

- Rails will have more rail breakage due low temperature.
- On tracks where the wind can build snow piles due to drifting snow trains may get stuck.
- In switches, there can be a problem to move the switch blade due to snow.
- Overhead wires will have ice formation that can cause sparks and sometimes the contact wire is torn down

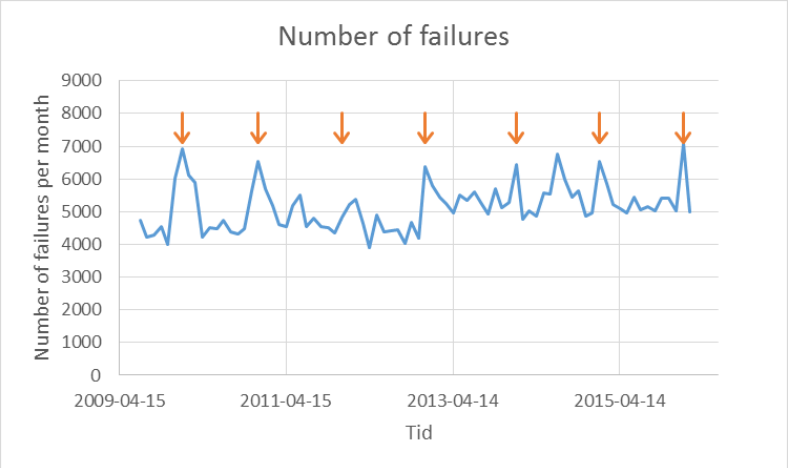

Figure 4.1.2. Number of failures for railway infrastructure in Sweden, red arrows mark December/January each year

4.1.4 IMPLEMENTED SOLUTIONS

Heating by electrical or gas systems is generally the implemented solution. The energy flow is higher with gas solutions and therefore such systems can faster remove large amounts of snow. Heating with an electrical heater is more reliable and does not require as much maintenance. A heater element have a power of 200 – 400 W/m, which is enough to heat the rail to a temperature of at least 20 degrees higher than the ambient temperature. The heating elements are placed on the inside foot of the stock rail and on the foot or in the web of the switch rail. Most of the heat from a heating element is radiated out in the air. If the fastening of the heating element is not maintained there might be a distance between the heating element and the rail leading to reduced efficiency. Trafikverket's heating elements reaches 700 W/m at the tip of the switch rail and between 300 – 600 W/m in the rest of the heated area. The solution can guarantee at least removal of 20 cm snow per hour. The life of a heating element is about 10 years.

4.1.5 POSSIBLE SOLUTIONS UNDER TEST

Trafikverket is investigating several new solutions that can make the heating system more efficient, more reliable and able to cope with more snow than previously. One solution is based on heating cables which are restricted in power output (to about 150 W/m per cable) but are more efficient as the energy to heat up the rail is not radiated to the air and most of the power is used to heat up the rail, see Figure 4.1.3.

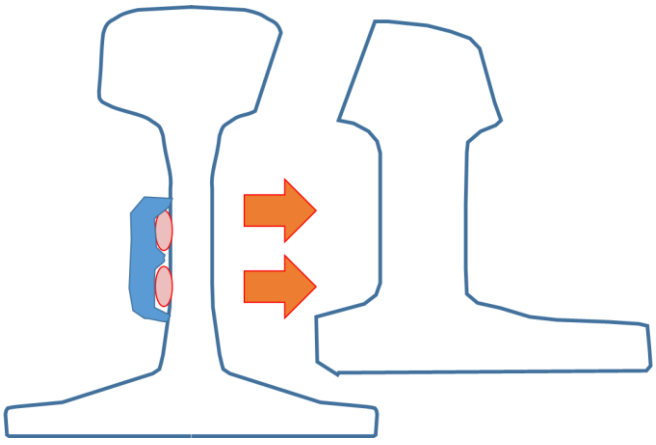

Figure 4.1.3. System with heating cables. The cables are protected by an insulating cover which reduces the heat loss to the air

Other tests are based on heating plates that can heat up the air between switch rail and stock rail by using from 100 W up to 900 W per sleeper gap. The maximum power is enough to heat more than 80 cm snow/hour which is the demand Trafikverket has asked for in the tender. The most challenging with these systems is how to control them. As the power output is so high it is even more important to limit the use to situations when there is heavy snow fall or drifting snow and hard winds than for the standard system.

4.1.6 NEED FOR FURTHER DEVELOPMENT

Systems using cold or warm air as well as a system using warm water are in use in Japan. Some tests of this system have been performed in Europe. In Canada, anti-freeze liquid is used by manually spraying it on S&Cs and a Swedish company has offered a more automated system which is still under development.

4.2 WARM CLIMATE

4.2.1 BACKGROUND

Railway operators operate within a variety of meteorological conditions, some of which are particularly problematic for rail transportation. Warm weather conditions influence railways in general. These conditions may affect operating efficiency, physical infrastructure, and the safe passage of freight and people. Precipitation and fog lead to decreased visibility of signals, flash floods can wash out tracks, and excessive heat can warp tracks. Crosswinds can reduce stability or lead to blow-over of railcars. Snow and ice may cause regional delays or shutdowns. Serious problems can also result from pre-existing accumulations of rain, ice and snow not associated with current weather conditions.

Despite the growing availability and sophistication of weather information and introduction of new technologies, adverse weather conditions continue to cause problems for operators. Weather phenomena present many real-time and forecast problems that challenge the abilities of railway operators and crews to confront, recover from, avoid and communicate specific weather hazards.

Sections 4.2.1 – 4.2.3 have been written by TCDD, while Sections 4.2.4 – 4.2.5 have been written by VCSA.

4.2.2 WARM WEATHER- RELATED PROBLEMS AT TCDD

As a result of examination of the records from TCDD accident and incident reports and speed restriction records for the period 2012-2014 it is found that 163 weather-related railway accidents and incidents have occurred, 46.6% of those were most closely associated with extreme heat causing track buckling and deterioration of track geometry.

Another problem is that due to adverse effect extreme heat on railway switches point machine protect itself and the signal turns into red. In addition, track buckling is also seen on steel railway bridges at TCDD lines.

So temperature extremes and temperature variability are the most frequently seen weather-related cause of derailments. Fast moving trains traversing tracks that are kinked, misaligned or broken have the potential to derail many railcars. Collisions are less common than derailments. Fast moving trains traversing tracks that are kinked, misaligned or broken have the potential to derail many railcars. Accidents during the summer months of June, July, and August are predominantly caused by high temperatures at TCDD networks.

Figure 4.2.1. Failure of track geometry due to warm weather

Precautions for summer at TCDD

Before summer, small fastening materials are loosened and those damaged are maintained and the screws are tightened to suitable torque values

- Making up deficiency of ballast, especially in curvy areas ballast shoulders are reinforced.
- Speed restriction to prevent any hazard during very high temperatures
- Track maintenance is performed by tamping machine except in August and July.

4.2.3 TEMPERATURE - EXTREMES AND VARIATIONS

The temperature at which railway track is laid or when repairs are made is referred to as the “rail neutral temperature.” Any significant deviation above or below this temperature may result in expansion or contraction in the steel rail. The TCDD network is divided into 7 regional directorates, see Table 4.2.1.

Table 4.2.1. Temperatures in different directorates of the TCDD network

REGIONS	Max Air Temperature Measured (in 50 Years)	Minimum Air Temperature Measured (in 50 Years)	Maximum Average Rail Temperature (In 50 Years)	Corresponding Neutral Temperature (In 50 Years)
REGION-1	44,10°C	-19,50°C	28,68°C	33,68°C
REGION-2	44,40°C	-31,40°C	25,63°C	30,63°C
REGION-3	44,60°C	-21,80°C	29,65°C	34,65°C
REGION-4	45,00°C	-37,00°C	24,68°C	29,68°C
REGION-5	46,00°C	-34,40°C	26,78°C	31,78°C
REGION-6	47,00°C	-28,00°C	30,15°C	35,15°C
REGION-7	43,80°C	-27,40°C	23,25°C	28,25°C

Thermal misalignments caused by sun induced kinks have often been identified as a cause of train derailments with the potential for injuries, fatalities and property damage. A kink that occurs at a rail joint can cause the joint to give way under the weight of the train. Thermal misalignment of railway tracks may be further compounded by poor ballast condition or a soft roadbed. A lead locomotive or railcars may derail when high heat causes a switch to open up, forcing the train up and over the switch. Extreme heat may also produce misalignment and slack, as well as damage to catenaries and pantographs. High stresses increases the risk of sun buckling close to the S&C, but also give longitudinal and lateral displacements within the switch panel. These displacements are causing failures due to “S&C not in control”.

4.2.4 TEMPERATURE RELATED PROBLEMS– EXPERIENCE FROM NETWORK RAIL

Switches and Crossings (S&C) work and the plain line immediately adjacent to S&C is at the highest risk of buckling and preparation work in these locations is the most critical. S&C with timber bearers are at greatest risk.

One method of monitoring or controlling temperatures around S&C, in the event of high temperatures is to deploy a permanent track watchman to remain on site, recording and watching the track every time a train passes over the location. Typically the watchman will have a temperature gauge and take regular readings of the rail temperature.

4.2.4.1 Point work expansion

Points and switches have moveable parts that have intricate mechanical interlocking systems. During periods of high temperature these are vulnerable to expansion and can foul other equipment and cause failures. If expansion occurs, switches may not be able to operate for the passage of a train or are able to detect the train and this will inevitably cause disruption to the network.

One of the first signs of a problem is when the signaller operates the points but does not get the required indication on the signalling panel. The points may have moved to the required position but will not lock into the position. Switch diamonds are more vulnerable than an ordinary switch.

Normal mitigations include, but are not limited to:

- Ensuring all equipment has been correctly adjusted
- Lubricating moveable parts where possible
- Painting the points with a reflective paint
- Arranging patrols to inspect vulnerable locations during periods of high temperatures
- Track Section Manager to monitor points lubrication and arrange enhanced lubrication to reduce risk.

Expansion and subsequent deformation can also occur on switches which incorporate stress transfer blocks, as pictured below.

Figure 4.2.2. Misalignment at switch heel due to thermal forces

Maintaining a stable and high rail neutral temperature is critical for prevention of this type of buckling. Neutral or force-free temperature of CWR is usually different from initial installation or anchoring temperature. Rail longitudinal movement (creep) can be due to train braking and traction forces, or due to differential thermal forces (sun and shade). Compressive and tensile forces can cause radial breathing of curves especially in weak ballast conditions. Vertical differential settlement of rails can occur on new or recently surfaced track, or in areas of weak subgrade conditions. Neutral temperature changes can be influenced by maintenance operations including: lifting, lining, and tamping, replacing broken rail, destressing, and installing CWR in cold weather.

4.2.4.2 Painting of critical switches and switch diamond crossings

The Track Managers in the UK will arrange the painting of operationally critical switches and switch diamond crossings with heat-reflecting white paint. They would typically ask for this to be completed by 31st March each year. Painting rails at-risk white so they absorb less heat, reducing rail temperatures. Typically measurements have shown that a painted rail will be five to ten degrees cooler than an unpainted rail.

Figure 4.2.3. Switch diamond with heat-reflecting paint

4.2.5 CWR INCORPORATION PROCEDURE FOR S&C

The integration of the turnout section into a continuous rail is now a common practice. It can nevertheless be observed that the procedures to perform such integration are not yet normalized. The consequence is that those procedures are different from one network to another. Not known or not properly applied by the installation entity, the turnout section becomes a fixed point in the track where all forces are joining creating a particular stress condition and potentially unstable.

Integration procedures can be standardised and at least minimum requirements can be put into an EN standard.

The main topics to be addressed in this chapter are:

- Crossing section: fixed or moveable frogs are often considered as fixed points in the track, concentrating track forces.

- Toe of the switch: holding the safety equipment often allows creeping of the rail, thus disturbing the equipment.
- Force levels in the turnout can become extremely significant introducing additional stresses, geometrical instability and stress risk.

Standard requirements and methodologies are thus needed to ensure proper integration of the turnout.

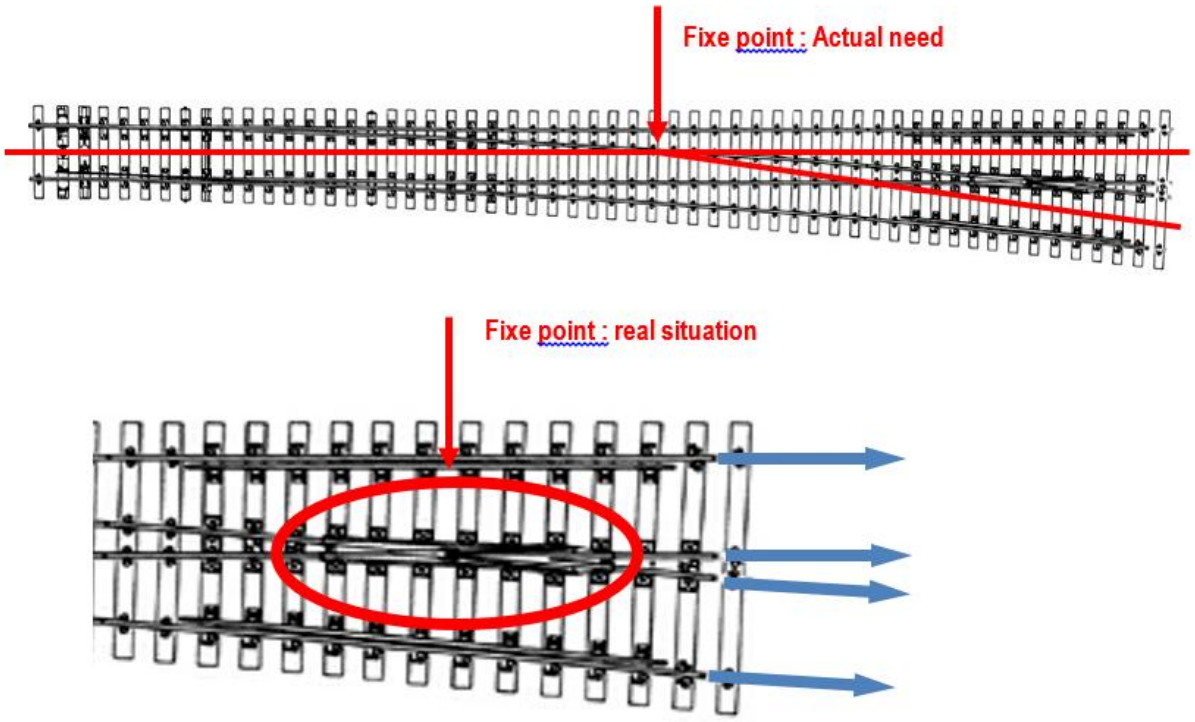

Figure 4.2.4. The crossing is forming a fix point due to the two rails linked at the heel. This results in high forces on the welds

4.3 RAINY CONDITIONS

4.3.1 BACKGROUND

High waters from flash floods, river floods, persistent heavy rains, and hurricanes are one of the most known weather-related concerns facing the railway operators.

Washouts caused by runoffs from earlier heavy rains or rising waters have the potential to weaken bridge trestles, undermine ballast, and cause collapsed culverts. Derailments and spills can then occur when the roadbed or bridge gives out. Snowmelt causes similar saturation problems by removing ballast, making soft roadbeds. Deteriorated ties further increase these risks.

Slides can threaten the safety and efficiency of railway operations. Slide mitigation planning and implementation requires the development of warnings that allow trains to safely stop in advance of a hazard. Ground movements as a result of heavy rains, freeze-thaw cycles, tremors and other factors can disturb large boulders or large fields of rocks. These may derail a train in motion, or block tracks by debris from rock slides, mudslides, avalanches, fallen trees etc. and cause significant delays or damages.

Sections 4.3.1 – 4.3.2 have been written by TCDD, while Section 4.3.3 has been written by VCSA.

4.3.2 RAINY WEATHER –RELATED PROBLEMS AT TCDD NETWORK

As a result of examination of the records from TCDD accident and incident reports and speed restriction records for the period 2012-2014, it is found that 163 weather-related railway accidents and incidents, excluding winter conditions have occurred, 46.6% of those were most closely associated with extreme heat causing track buckling and deterioration of track geometry. The remaining 53.4% is closely associated with rainy conditions causing slides of mud and rocks, flood and saturated soil, precipitation etc. 10% of rainy condition cause preciptation, 59% is subsidience and track geometry deterioration, about 6% is rock sliding, about 19% is landslides, about 6% is flash flooding, river flooding.

We can schedule the failures due to precipitation at TCDD network as below:

- Unavailability of railway due to landslide
- Subsidence of track
- In case of choked culverts and arched bridges during heavy rain and flood, suspension of railway track is seen due to washed away ballast
- Geotextiles are used on the platform for the known subsidence locations to drain the water

Following heavy rain, flooding and earthquakes, civil structures like tunnels, bridges, culverts etc. and cuttings, embankments, ditches are checked at once.

If frost comes after rain, upon the melting of frost, railway track becomes more instable than usual. In such situations, the above-mentioned checks start at early hours of the day. If there is very hot weather prevailing, checks are carried out around noon and afternoon depending on the situation.

Figure 4.3.1. Landslide due to extreme rain

Figure 4.3.2. Drainage failure due to excessive rain

Figure 4.3.3. Fallen rocks due to rain

Figure 4.3.4. Landslide due to excessive rain (left) and unavailable track due to fallen rocks caused by excessive rain (right)

TCDD makes the following precautions to reduce failures due to winter, rain and flooding to a minimum:

- Cleaning of arched bridges and culverts
- Supporting of piers of steel bridges
- Due to signs of deviation in river bed and to protect the platform from water, spur diking is applied as a measure in advance
- Cleaning of cuttings
- In rocky areas, the rocks that have a risk to fall down are removed
- To prevent the flooding coming from a mountain side from moving to the railway line, head ditches are built as a mitigation measure and water is directed to culverts

The well-known problematic places are always under control by TCDD maintenance staff. In case of any sign for heavy rain or snow, a maintenance team is directed to those places for checking purposes. This team has close communication with a dispatcher to govern the traffic.

Most common failures observed in summer and winter at TCDD network

In the TCDD network, climatic factors are considered as the external factors that have very large influence on railway infrastructure and catenary systems. Climatic factors affect large areas. To provide aggregated climatic data at country level is more realistic, see Table 4.3.1.

Table 4.3.1. Climatic data in TCDD network

<table>
<tr><th>CLIMATIC DATA</th><th>AT COUNTRY LEVEL- TURKEY</th></tr>
<tr><td>Average Ambient Temperature</td><td>From 2009 to 2014;
Avg. of the min extremes: -33.6° C
Avg. of the max extremes: 46.1° C</td></tr>
<tr><td>Average Humidity</td><td>63.8%</td></tr>
<tr><td>Wind Speed</td><td>1.9 m/sec</td></tr>
<tr><td>Ice Loads</td><td>
<table>
<tr><th rowspan="2">*Region No</th><th rowspan="2">Ice load coefficient</th><th rowspan="2">Ice load kg/m</th><th rowspan="2">Ice load N/m</th><th colspan="2">Ambient Temperature</th></tr>
<tr><th>Highest</th><th>Lowest</th></tr>
<tr><td>1</td><td>0</td><td>0</td><td></td><td>50</td><td>-10</td></tr>
<tr><td>2</td><td>0.2</td><td>0,2√d [1)]</td><td>1.96√d [1)]</td><td>45</td><td>-15</td></tr>
<tr><td>3</td><td>0.3</td><td>0,3√d</td><td>2.94√d</td><td>40</td><td>-25</td></tr>
<tr><td>4</td><td>0.5</td><td>0,52√d</td><td>5.096√d</td><td>40</td><td>-30</td></tr>
<tr><td>5</td><td>1.2</td><td>1,2√d</td><td>11.76√d</td><td>40</td><td>-30</td></tr>
</table>
1) d=Radius of conductor; * Region numbers are indicated on the map
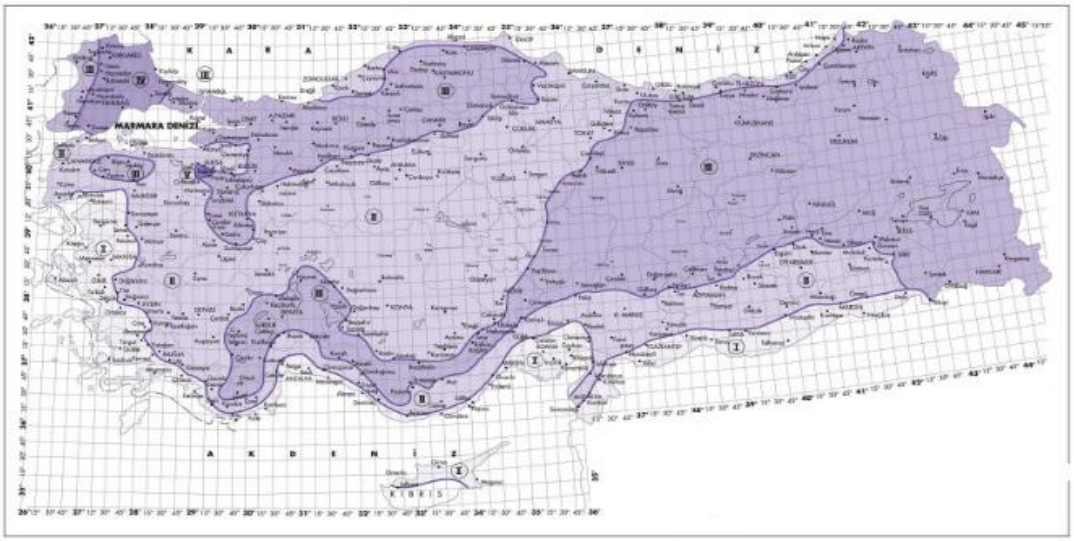

Ice Load map of Turkey
</td></tr>
</table>

Air Quality	

The most common climatic factors causing failures seen in the TCDD network are:

- Heavy rain
- Fallen tree on catenary system due to wind
- Precipitation
- Track geometry failure due to external factors
- Fire
- Stroke of lightning onto substation
- Flood
- Falling rocks on the track
- Track alignment problems

The TCDD network is divided into seven regions. For regions 2, 4, 5 and 6, statistics for the most commonly observed climatic factors leading to failures in 2014 to 2015 are presented in Tables 4.3.2 to 4.3.4.

Table 4.3.2. Number of failures in 2014 to 2015 for Region 2

REGION 2	2015											
EXTERNAL FACTORS	JAN.	FEB.	MAR.	APR.	MAY.	JUNE	JULY	1. Region	SEP.	OCT.	NOV.	DEC.
heavy rain	0	0	0	0	0	0	0	0	0			
fallen tree on OHL	1	0	0	0	0	1	0	0	0			
precipitation	0	0	0	0	0	1	0	0	0			
Track geometry failure due to external factors	0	0	0	0	0	0	0	0	0			
fire	0	0	0	1	0	0	1	1	0			
stroke of lightning onto substation	0	0	0	0	0	0	0	0	0			
flood	0	0	0	0	0	0	0	0	0			
falling rocks on the track	0	0	0	0	0	0	0	0	0			
storm	0	0	0	0	0	0	0	0	0			
track allighment problems	0	0	0	0	0	0	0	0	0			
REGION 2	2014											
EXTERNAL FACTORS	JAN.	FEB.	MAR.	APR.	MAY.	JUNE	JULY	AUG.	SEP.	OCT.	NOV.	DEC.
heavy rain	0	0	0	0	0	0	0	0	0	0	0	0
fallen tree on OHL	0	0	0	0	0	0	0	0	0	0	0	0
precipitation	0	0	0	0	0	0	0	0	0	0	0	0
Track geometry failure due to external factors	0	0	0	0	0	0	0	0	0	0	0	0
fire	0	0	0	0	0	0	1	0	0	0	0	0
stroke of lightning onto substation	0	0	0	0	0	1	0	0	0	0	0	0
flood	0	0	0	0	0	0	0	1	0	0	0	1
falling rocks on the track	0	0	0	0	0	0	0	0	0	0	0	0
storm	0	0	0	0	0	0	0	0	0	0	0	0
track allighment problems	0	0	0	0	0	0	0	0	0	0	0	0

Table 4.3.3. Number of failures in 2014 to 2015 for Regions 4 and 5

REGION4-REGION5	2015											
EXTERNAL FACTORS	JAN.	FEB.	MAR.	APR.	MAY.	JUNE	JULY	AUG.	SEP.	OCT.	NOV.	DEC.
heavy rain	0	0	0	0	0	0	0	0	0			
fallen tree on OHL	0	0	0	0	0	0	0	0	0			
precipitation	0	0	0	0	0	1	0	0	0			
Track geometry failure due to external factors	0	0	0	0	0	0	0	0	0			
fire	0	0	0	0	0	0	0	0	0			
stroke of lightning onto substation	0	0	0	0	0	0	0	0	0			
flood	0	0	0	0	0	0	0	0	0			
falling rocks on the track	0	0	0	0	0	0	0	0	0			
storm	1	0	0	0	0	0	0	0	0			
track allighment problems	0	0	0	0	0	0	0	0	0			
REGION4-REGION5	2014											
EXTERNAL FACTORS	JAN.	FEB.	MAR.	APR.	MAY.	JUNE	JULY	AUG.	SEP.	OCT.	NOV.	DEC.
heavy rain	0	0	0	0	0	0	0	0	0	0	0	0
fallen tree on OHL	0	0	0	0	0	0	0	0	0	0	0	0
precipitation	0	0	0	1	0	0	0	0	0	0	0	0
Track geometry failure due to external factors	0	0	0	0	0	0	0	0	0	0	0	0
fire	0	0	0	0	0	0	0	0	0	0	0	0
stroke of lightning onto substation	0	0	0	0	0	0	0	0	0	0	0	0
flood	0	0	0	0	0	0	0	0	0	0	0	0
falling rocks on the track	0	0	0	0	1		0	0	0	0	0	0
storm	0	0	0	0	0	0	0	0	0	0	0	0
track allighment problems	0	0	0	0	0	0	0	0	0	0	0	0

Table 4.3.4. Number of failures in 2014 to 2015 for Regions 5 and 6

REGION5-REGION6	2015											
EXTERNAL FACTORS	JAN.	FEB.	MAR.	APR.	MAY.	JUNE	JULY	AUG.	SEP.	OCT.	NOV.	DEC.
heavy rain	0	0	0	0	0	0	0	0				
fallen tree on OHL	0	0	0	0	0	0	0	0				
precipitation	0	0	0	0	0	0	0	0				
Track geometry failure due to external factors	0	0	0	0	0	0	0	0				
fire	0	0	0	0	0	0	0	0				
stroke of lightning onto substation	0	0	0	0	0	0	0	0				
flood	0	0	0	0	0	0	0	0				
falling rocks on the track	0	0	0	0	0	0	0	0				
storm	1	0	0	0	0	0	0	0				
track allighment problems	0	0	1	0	0	0	0	0				
REGION5-REGION6	2014											
EXTERNAL FACTORS	JAN.	FEB.	MAR.	APR.	MAY.	JUNE	JULY	AUG.	SEP.	OCT.	NOV.	DEC.
heavy rain	0	0	1	0	0	0	0	0	0	0	0	0
fallen tree on OHL	0	0	0	0	0	0	0	0	0	0	0	0
precipitation	0	0	0	0	0	0	0	1	0	0	0	0
Track geometry failure due to external factors	0	0	0	0	0	0	0	0	0	0	0	0
fire	0	0	0	0	0	0	0	0	0	0	0	0
stroke of lightning onto substation	0	0	0	0	0	0	0	0	0	0	0	0
flood	0	0	0	0	0	0	0	0	0	0	0	0
falling rocks on the track	0	0	0	0	0	0	0	0	0	0	0	0
storm	0	0	0	0	0	0	0	0	0	0	0	0
track allighment problems	0	0	0	0	0	0	0	0	0	0	0	0

4.3.3 FLOODING – PROBLEMS RELATED TO NETWORK RAIL

During periods of heavy rain, routes may experience localised or in some cases extensive flooding. Floodwater has the ability to wash away large sections of track bed and cause signalling failures if equipment becomes waterlogged or track circuits become fully submerged.

Heavy rain bursts can cause two types of flooding in the summer months: ground water flooding and run-off flooding.

Ground water flooding is generally a result of heavy rain falling proceeded by a long wet spell. Low lying ground becomes saturated and can physically hold no more water, so the site becomes flooded.

Run-off flooding on the other hand, is caused by an intense burst of rain (normally associated with summer thunderstorms). The rain is so heavy that it cannot drain away quickly enough, or the drains cannot cope with the amount of rainfall so flooding occurs. Urban areas are more susceptible to run-off flooding due to the semi-impervious nature of the roads, pavements and drains. The flooding, however, is generally localised.

During the summer, if there has been a particular dry spell, the ground may be baked and hard, increasing demands on drainage.

Basic preparations include but are not limited to:

- Ensuring that track drainage is kept clear from obstructions (normally ballast, vegetation and litter)
- Ensuring that off track drainage is clear from obstructions (this type of drainage is important in controlling or diverting run off from adjacent land)
- Ensuring local authorities have adequate flood defences and that they are in a good state of repair
- The Rail Network's flood defences are in a good state of repair
- Reporting of any blocked drains or defective pumping locations to Route Control
- Deploy flood defence systems including modular ridged barriers with a membrane that seals to prevent water getting through, and inflatable barriers which are filled with flood water.
- Build pumping stations in locations which are prone to flooding so we can quickly pump flood water away

Many sections of railways were built in cuttings and tunnels which are lower than the surrounding area, and many other lines are on flat, low-lying land with limited drainage, making them prone to flooding.

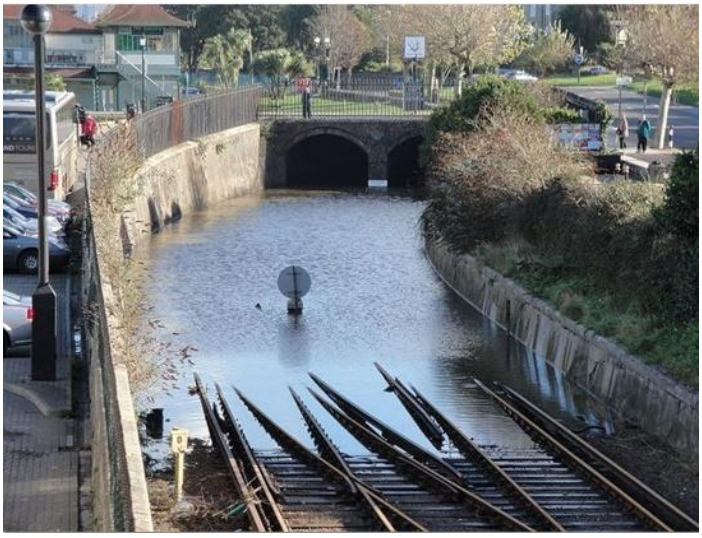

Figure 4.3.5. Flooding in switches and crossings

Flood water can wash away ballast - the bed of stones which supports sleepers - making the line unsafe until it is re-laid.

The development of land near the railway can increase the risk of flooding. If the drainage system is inadequate, rain which previously soaked into the ground may run off tarmac and concrete and straight onto the tracks.

When the water level rises above the rails, trains have to reduce their speed to prevent damage to the train. If the track has a live conductor rail, flooding can cause a short circuit.

Points and signalling equipment can fail when water enters their housings and may need replacing before services can resume.

When lines that are at risk of flooding effort are renewed, care is taken to raise the tracks and signalling equipment to try to mitigate this.

5 Optimized S&C sensor strategies to minimize traffic disruptions (C4R task 1.3.4)

Today, the most common way to inspect S&Cs is by manual personnel. Recorded measurements from such visits can be used for monitoring purpose, but most of the inspections are not quantified and are therefore not useful for predictions. Section 5 has been written by Trafikverket.

5.1 KEY OPERATIONAL PARAMETERS

S&Cs can be monitored in track by stand-off equipment, by the point machine, by the interlocking system or by vehicles.

5.1.1 MONITORING IN TRACK (EMBEDDED SENSORS)

Monitoring in track will be investigated in the In2Rail project and therefore it is just briefly covered here. Sensors measuring acceleration, displacement or strain can be used on the rails. Sleeper strain and ballast pressure or displacement can be measured. Most of these measurements are used by CEDEX in their track box.

Temperature is measured to control the heating elements.

Force is more difficult to measure than strain. In straight track, a wheel impact load detector can be used to indirectly measure the vertical wheel-rail contact force by measuring the force at the rail seat. These detectors are 7 metres long to cover twice the circumference of a wheel so it is not realistic to use them in an S&C. When using strain gauges applied on the rail web, the vertical force can only be determined if the contact points are known in advance, and in S&Cs double point contact occurs both in the switch panel and in the crossing. Thus, to measure wheel-rail contact forces (vertical, lateral and longitudinal) in S&Cs, it is necessary to use an instrumented wheel set.

5.1.2 MONITORING BY USING STAND-OFF EQUIPMENT

Monitoring by using stand-off equipment will be investigated in the In2Rail project and is therefore just briefly covered here.

Stand-off technology uses laser and/or camera technology to measure or observe. It normally also involves some kind of video analysis and pattern recognition. It is possible to measure distances and profiles, and also changes, over time. For instance if objects are stuck between switch rail and

support rail this can be observed by a camera. Standoff technology is also used to observe settlement over time.

A special possibility that is a mix between in track measurements and stand-off technology is the use of sensors placed in track that communicate wirelessly with equipment outside the track. In WP1 and WP4 strain sensors are going to be embedded in concrete and activated by RFID technologies. For more simple applications, the energy of the sensor might be sent to the sensor with RFID technology. For more advanced applications, a battery is needed for the sensors.

5.1.3 MONITORING BY POINT MACHINE AND INTERLOCKING SYSTEM

The point machine always controls in which position the S&C is. During the movement of the switch rail, time for movement, force, motor current, hydraulic pressure and/or the distance can be measured. Voestalpine offers the system Roadmaster [5.1.1] that is a system that includes both point machine measurements and track measurements in the S&C.

VCSA offers the systems SURVAIG [5.1.2] and SURTRACK, which are designed for predictive maintenance of track equipment and track circuits.

In digitalised interlocking systems, current, voltage and energy can be measured and time variant control signals can be registered. Even in relay based interlocking systems, it is possible to record the occurrence of and when in time different states occur.

5.1.4 MONITORING BY VEHICLES

Measurement by vehicles is standard for track including the straight section (through route) of an S&C, and it is performed as often as it is for standard track. For diverging track, the measurements are performed more seldom. All infrastructure owners measure track geometry and, by ultrasonic equipment, internal rail defects. For surface initiated rail defects, eddy current, video inspection and even accelerometers (squats) can be used.

5.1.5 REFERENCES

[5.1.1] https://www.voestalpine.com/bwg/static/sites/c015/downloads/en/products/Roadmaster_en.pdf

[5.1.2] http://www.vossloh-cogifer.com/en/products_and_systems/track_monitoring_2/track_monitoring_3.html

5.2 SENSOR STRATEGIES

The overall goal for all monitoring is to be able to take decisions of maintenance in time before failures are affecting the operation of traffic.

The condition data must therefore include a prediction of deterioration over time. When the signal passes the threshold value there must (in most cases) be a long enough failure development time to allow for safe traffic operation until adequate maintenance is performed.

5.3 RELATIONSHIP BETWEEN SENSOR DATA AND DETERIORATION LEVELS

Sensor data are first collected locally and can be either stored as raw data or summarized in mean values, standard deviation, minimum and maximum values. Measurements at different times can be used to follow trends and based on these trends it is possible to predict when in time to do maintenance.

Here the focus will be on data from track geometry cars and in particular the development of the level signal. Level is the vertically position of the rail and is normally the signal from the track geometry car that changes fastest over time.

An example for a crossing at Trafikverket is given in Figure 5.3.1. The S&C Åby 133 b was placed in track in 2013. The crossing had shortly after installation a dip of 6 mm, which is unusually much. Because of the bad initial situation and no performed maintenance, the dip has during the following two years developed to about 11 mm, which is close to the maintenance limit for normal track.

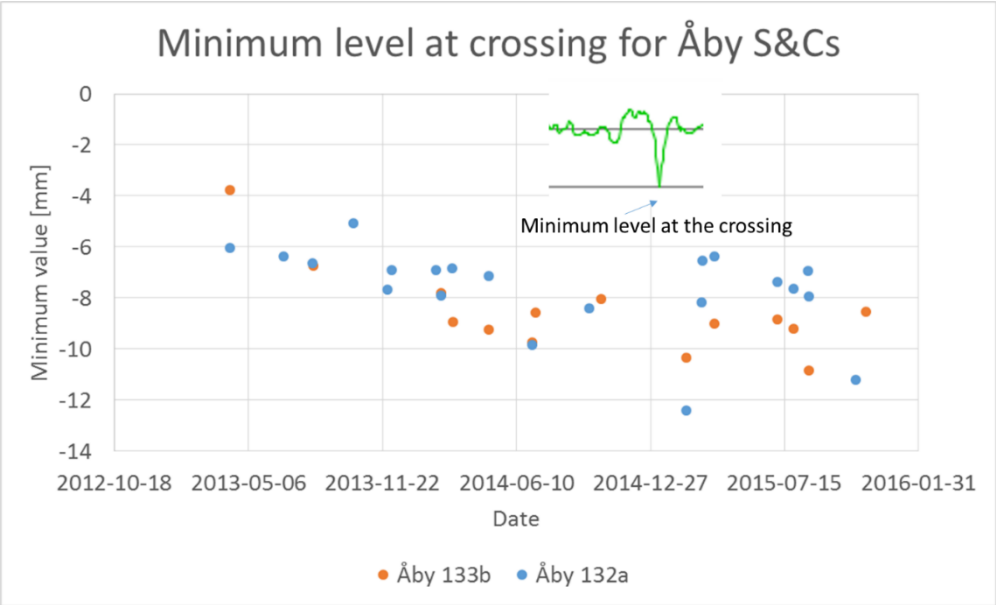

Figure 5.3.1. Time history of measured minimum level for the crossing at Åby 133b. Maintenance can be planned before the minimum level reaches a certain value

Measurement of track geometry in S&Cs is still an area where development is needed as each recording needs to be compared for nearly the same location (within 5 m) to be sure that the analysis is done in a correct way. For normal track, a larger deviation is acceptable. Today's system for presenting track geometry gives possibilities to monitor track degradation over time, which has been proven by for instance the Technical University of Graz. To be able to perform a similar analysis for S&Cs it is necessary to identify the different panels of the S&C and use different parameters for each panel. The geometry at the crossing and the point machine are normally not within the tolerances of new laid track (+/- 2 mm) and should therefore be identified and monitored separately, while the rest of the S&C can be treated as normal track. For the diverging route, a special analysis of gauge, side wear and alignment also can be made. In the analysis, prediction models for each parameter is needed and these models need input of traffic volume in straight and diverging routes.

6 Conclusions

The present deliverable is an intermediate report describing the work carried out in tasks 2, 3 and 4 of Capacity4Rail WP1.3.

The main focus has been to investigate and propose innovative designs aiming towards improved railway turnouts (S&C) that reduces material deterioration (wear, plastic deformation, rolling contact fatigue) and failures (C4R task 1.3.2). Based on numerical simulations of dynamic vehicle-track interaction using validated models and software, it has been demonstrated how rail and track degradation can be reduced by optimisation of geometry and stiffness properties of the turnout, leading to reduced Life Cycle Cost (LCC).

The investigated *short-term solutions* for reducing loads and rail profile degradation in the switch panel have included selection of (1) rail profile and rail inclination, (2) rail grade, and application of (3) friction management. The calculations have shown that a design with inclined rails (1:30) is superior to the case with vertical rails. The selection of rail grade R350HT instead of R260 leads to an expected reduction in wear, but in order to more accurately quantify the improvement there is a need for validation of the implemented wear map model by further measurements of the influence of contact pressure and sliding velocity on wear coefficients for different rail grades. The predicted influences of rail grade and friction management on RCF are uncertain due to the wide range of factors influencing RCF initiation, such as the important interaction between crack growth and wear in situations with medium-high levels of energy dissipation ($T\gamma$) in the wheel-rail contact. Such situations have been shown to be common in the switch panel and in particular at rail sections where there are transitions between ‘one-point’ and ‘two-point’ wheel-rail contact. Thus, it is important that the implemented RCF damage model is validated by future field observations and measurements. It has been shown that both wear and RCF are reduced significantly by maintaining a low friction coefficient in the wheel-rail contact. In particular, situations with dry wheel-rail contact (high friction) should be avoided as these lead to very high RCF damage impact. Remaining work on short-term solutions will focus on prescribed track gauge variation in the switch panel and accounting for traffic in facing and trailing moves in both through and diverging routes.

The investigated *medium-term solutions* have focussed on improving the performance of the crossing panel. These solutions have included (1) geometry optimisation of the crossing to minimise impact loads and reduce the steering force damage in the contact areas, (2) dynamic load mitigation (ballast protection) through rail pad stiffness optimisation and the use of under sleeper pads (USP) or connecting elements between sleepers, and (3) novel materials in crossing nose and wing rails to resist fatigue, wear and plastic deformation.

The investigation in crossing geometry has highlighted key differences in current design practice and machining tools used for half and full cant (UK terminology) geometries, leading to quantifiably different damage behaviour. The interaction between wheel shape and the crossing wing geometry

is a determining factor in the level for vertical impact force, lateral dynamics and resulting rail damage. The crossing with a higher inclined wing rail showed better performance across all wheels simulated. The peculiar behaviour of hollow wheels has been quantified and shown to be more reactive to one of the crossing types. High conicity wheels are also potentially leading to higher dynamic impact. All this needs to be considered in the design process. On that basis, the proposed methodology can enable a fast and effective optimisation process of the crossing wing rail geometry minimising vertical impact loads, wear and RCF on both wing rail and crossing vee. The topic of further work will focus on modifying the shape of the wing rail (inclined, length of inclined and slope of topping) to achieve an optimum solution in between the two investigated so far. Like for the short-term optimisation in switches, there is a crucial need for more material data to quantify their resistance to wear and RCF in high energy ($T\gamma$) and high load regimes, with the particularity of cast manganese behaviour, having a very non-linear and unpredictable hardening process through the earlier cycles of utilisation. Such data is currently not available to make a full utilisation of the methodology developed here. Alongside, it is important to be able to measure precisely the evolution in shape of crossing both at the early stages and throughout their life by using advanced 3D scanning equipment.

A methodology has also been proposed for the optimisation of rail pad stiffness in crossing panel, showing that low stiffness rail pads (ca 80 kN/mm) provide a suitable mitigation for ballast pressure, sleeper acceleration and minimising contact forces, while maintaining acceptable bending stresses of rail components. This study can be extended to more crossing types, length and speed, as well as include baseplate systems. An investigation into the role of under sleeper pads (USP) in mitigating vertical dynamics loads has been presented, highlighting the importance of careful selection of USP properties, so that the system response is fully understood while designing or upgrading an S&C. Finally, an investigation in linking sleepers together in the areas of load transfer of a crossing panel has shown some benefits in protecting the ballast layer while making the panel behave more like a slab. It is proposed this is followed up by further investigation in lateral and combined vertical/lateral loading to highlight benefit and cross over between ballasted and non-ballasted tracks, possibly within the lighthouse project In2Rail under hybrid track scope.

Next generation S&C (*long-term solutions*) will be based on a whole-system approach including enhanced design, materials and components and incorporation of modern mechatronics for improved system kinematics and control. One example of a long-term solution that has been discussed in the report is the Modular Continuous Support (MCS) track, which is a ballast-less track design offering an efficient lower cost rail technology based on pre-fabricated modules and continuously supported rails. Next generation S&C will be an important topic for further work in Shift2Rail.

Operation of S&Cs in extreme weather conditions is a challenge to railway administrations (task 1.3.3). The report includes a survey of common problems occurring due to situations with strong winds at low temperatures and heavy snow fall, as well as at high temperatures and due to heavy rain fall and flooding. Innovative solutions and operational practices to ensure resilience to these extreme conditions are discussed and will be further investigated in remaining work of Capacity4Rail.

The last section of the report includes a brief survey of optimised maintenance and sensor strategies (task 1.3.4). The implementation of monitoring strategies and sensor technology is covered in more detail in Capacity4Rail SP4.

In task 1.3.5 (not reported here), innovative S&C concepts will be demonstrated. The distribution of budget for the demonstrators was not yet decided at the time of writing of this report. However, several proposals closely related to the demonstration and validation of results in the present report have been suggested. Examples of proposed demonstrators are testing of a new bainitic material in the crossing panel, measurement of the influence of rail pad and under sleeper pad stiffness on (differential) settlement in the crossing in a controlled environment at the CEDEX track box, and further measurements of wear coefficients for different rail grades at various combinations of contact pressure and sliding velocity.

The present work and the writing of this deliverable were performed by Chalmers (lead contractor), University of Huddersfield, VAE, VCSA, INECO, TCDD and Trafikverket.